

2014-01-01

# Light Scattering From Aerosol Particles In The El Paso Del Norte Region / The Effect Of Humidity

Richard Medina Calderon

*University of Texas at El Paso*, [rmedina9@miners.utep.edu](mailto:rmedina9@miners.utep.edu)

Follow this and additional works at: [https://digitalcommons.utep.edu/open\\_etd](https://digitalcommons.utep.edu/open_etd)



Part of the [Atmospheric Sciences Commons](#), and the [Optics Commons](#)

---

## Recommended Citation

Medina Calderon, Richard, "Light Scattering From Aerosol Particles In The El Paso Del Norte Region / The Effect Of Humidity" (2014). *Open Access Theses & Dissertations*. 1296.  
[https://digitalcommons.utep.edu/open\\_etd/1296](https://digitalcommons.utep.edu/open_etd/1296)

This is brought to you for free and open access by DigitalCommons@UTEP. It has been accepted for inclusion in Open Access Theses & Dissertations by an authorized administrator of DigitalCommons@UTEP. For more information, please contact [lweber@utep.edu](mailto:lweber@utep.edu).

LIGHT SCATTERING FROM AEROSOL PARTICLES IN THE EL PASO  
DEL NORTE REGION / THE EFFECT OF HUMIDITY

RICHARD MEDINA CALDERON

Computational Sciences Program

APPROVED:

---

Rosa Fitzgerald, PhD., Chair

---

Marian Manciú, PhD.

---

Rodrigo Romero, PhD.

---

Charles Ambler, PhD.  
Dean of the Graduate School

Copyright ©

by

Richard Medina Calderon

2014

## DEDICATION

To my beloved parents Dolores and Bartolo . . .

LIGHT SCATTERING FROM AEROSOL PARTICLES IN THE EL PASO  
DEL NORTE REGION / THE EFFECT OF HUMIDITY

by

RICHARD MEDINA CALDERON

DISSERTATION

Presented to the Faculty of the Graduate School of

The University of Texas at El Paso

in Partial Fulfillment

of the Requirements

for the Degree of

DOCTOR OF PHILOSOPHY

Computational Sciences Program

THE UNIVERSITY OF TEXAS AT EL PASO

December 2014

## ACKNOWLEDGMENTS

First and foremost to my advisor Rosa Fitzgerald, for all the dedication she put in this work, and for her patience, wise guidance and endless encouragement throughout all this months.

A special thanks to my committee members, who were always available to discuss ideas, to Dr. Marian Manciu and to Dr. Rodrigo Romero for reviewing this work. Also special thanks to Dr. Efrain Ferrer for our conversations in Physics which were always very productive and for being always accesible even when he was tired or busy.

Thanks to Dr David Dubois from the New Mexico Climate Center for his financial support at the beginning of this project, and also to the people of the department of Physics who always support me with TA's postion even when the resources were scarce.

Finally, I would like to extend special thanks to the NOAA/EPP, for the financial support in this last months that made the completion of this work possible and to all the people of the Computaional Sciences Program of the University of Texas at El Paso.

## ABSTRACT

Atmospheric aerosols play an important role in climate forcing, through scattering and absorption of the incoming solar radiation. The extinction of light by the presence of atmospheric aerosols was studied using two first-principle models, and corresponding computer codes. In the first model the extinction of light from irregularly shaped aerosol particles was analyzed. In the second model it was assumed that the irregularly shaped aerosol particles were covered by a film of water, and the hygroscopicity and the extinction of light by the aerosols was analyzed. These models were then applied to the Paso del Norte region and their light extinction results compared with a local extinctionmeter. The inter-comparison of the models extinction results and the extinctionmeter values were well correlated. It was observed that for high humidity days the model that used an aerosol particle covered with a water film correlated better with the experimental extinctionmeter measurements. While these two models were validated in the Paso del Norte region, they are also applicable to any other region, under humid or dry atmospheric conditions.

## TABLE OF CONTENTS

<b>DEDICATION</b> . . . . .	ii
<b>ACKNOWLEDGMENTS</b> . . . . .	iv
<b>ABSTRACT</b> . . . . .	v
<b>TABLE OF CONTENTS</b> . . . . .	vi
<b>LIST OF TABLES</b> . . . . .	ix
<b>LIST OF FIGURES</b> . . . . .	x
<b>CHAPTER</b>	
<b>1 Introduction</b> . . . . .	1
1.1 Atmospheric Aerosols . . . . .	2
1.1.1 Atmospheric properties of atmospheric aerosols . . . . .	6
1.1.2 Optical parameters of atmospheric aerosols . . . . .	8
1.1.3 The Lognormal Distribution . . . . .	10
1.1.4 The volume-weighted method . . . . .	12
1.2 Extinction by an arbitrary particle . . . . .	13
1.2.1 Scattering, and absorption by an arbitrary finite particle	13
1.2.2 General formulation of the scattering problem (Mie Theory)	17
1.2.3 Expansion of a plane wave in vector spherical harmonics	23
1.2.4 The internal and scattering fields . . . . .	25
1.2.5 Particles small compared with the wavelength . . . . .	28
1.2.6 The scattering matrix . . . . .	31

	<b>Page</b>
1.3 The T-matrix approximation . . . . .	37
1.3.1 The T-matrix approximation for coated non-spherical particles . . . . .	40
<b>2 Methodology . . . . .</b>	<b>43</b>
2.1 Instrumentation . . . . .	43
2.1.1 Optical particle laser counter . . . . .	43
2.1.2 Photoacoustic Extinctionmeter (PAX) . . . . .	44
2.1.3 The Visible Multifilter Rotating Shadowband Radiometer	46
2.2 Mathematical models . . . . .	47
2.2.1 The Tropospheric Radiative Transfer Model (TUV) . . .	47
2.2.2 The T-matrix model . . . . .	48
2.2.3 The LISA model . . . . .	51
2.3 The Scattering Matrix . . . . .	52
2.3.1 The matrix element $F_{11}$ . . . . .	52
2.3.2 The matrix element $F_{22}/F_{11}$ . . . . .	53
2.3.3 The matrix element $F_{33}/F_{11}$ and $F_{44}/F_{11}$ . . . . .	53
2.3.4 The matrix element $F_{12}/F_{11}$ . . . . .	53
2.3.5 The matrix element $F_{34}/F_{11}$ . . . . .	54
2.4 Experimental setup . . . . .	54
2.4.1 Selection of days . . . . .	54
2.4.2 Input Process . . . . .	59
<b>3 Results and Discussion . . . . .</b>	<b>65</b>
3.1 April 13, 2013 . . . . .	67

	<b>Page</b>
3.2 July 18, 2014 . . . . .	84
<b>4 Conclusions and future work . . . . .</b>	<b>99</b>
4.1 Conclusions . . . . .	99
4.2 Future Work . . . . .	100
List of References . . . . .	104
<b>Vita . . . . .</b>	<b>107</b>

## LIST OF TABLES

Table		Page
1	The refractive index $n = m - ik$ of oceanic, water-insoluble (mainly, dust), water-soluble (sulfates, nitrates, etc.), and soot aerosol, respectively (courtesy of Kokhanovsky, A. [6]) . . . . .	5
2	T-matrix input parameter values . . . . .	50
3	T-matrix output information . . . . .	50
4	LISA input parameter values . . . . .	51
5	LISA output information . . . . .	51
6	Number concentration for April 13, 2013, in $\text{cm}^{-3}$ , diameters for the four bins are in $\mu\text{m}$ at the header . . . . .	57
7	Number concentration for July 18, 2014, in $\text{cm}^{-3}$ , diameters for the four bins are in $\mu\text{m}$ at the header. . . . .	58
8	Days selected and values of relative humidity and particle concentration for April 13 and July 18, 2014, in the PdN Airshed. .	59
9	Physical constant of species used in refractive index and density calculations (courtesy, Hand, J. L., et al. [36]) . . . . .	62
10	Time (hh:mm), $B_{\text{sca}}$ ( $\mu\text{m}^{-3}$ ) of instrument, LISA model, T-matrix model, Relative Humidity (%), and Index of Refraction for composite material for April 13, 2013 . . . . .	68
11	Time (hh:mm), $B_{\text{sca}}$ ( $\mu\text{m}^{-3}$ ) of instrument, LISA model, T-matrix model, Relative Humidity (%), and Index of Refraction for composite material for July 18, 2014 . . . . .	86

## LIST OF FIGURES

Figure		Page
1	Aerosol vertical distribution at 500 nm, for El Paso, TX. Notice the concentration of aerosols are mainly in the first two km of the troposphere approximately, a region called boundary layer .	6
2	Layers of the Earth's lower atmosphere, and the structure of the temperature and pressure with the altitude. Courtesy of Jacobson M. Z. [8] . . . . .	7
3	Extinction by a single particle. Courtesy of Bohren, C. F. [11]. .	14
4	The incident field ( $\mathbf{E}_{\text{inc}}, \mathbf{B}_{\text{inc}}$ ) gives rise to a field ( $\mathbf{E}_1, \mathbf{B}_1$ ) inside the particle and a scattered field ( $\mathbf{E}_{\text{sca}}, \mathbf{B}_{\text{sca}}$ ) in the surrounding medium of the particle labeled as 2. Courtesy of Bohren, F. C.[11]. . . . .	19
5	Scattering by an arbitrary particle. Courtesy of Bohren, C. F. and Huffman, D. R.[11]. . . . .	34
6	The geometry of a plane wave incident upon a sphere with a concentric spherical shell, as it was shown by Aden and Kerker [21]. . . . .	41
7	Climet CI-150t - Laser Particle Counter. . . . .	44
8	Photoacoustic extinctionmeter circuit diagram. . . . .	45
9	Photoacoustic extinctionmeter model PAX 870 nm. . . . .	45
10	Side (a) and close up view (b) of the Visible Multifilter Rotating Shadowband Radiometer installed at the roof of the Undergraduate Learning center (UGLC), at the University of Texas at El Paso. . . . .	47
11	Flowchart of procedure for light scattering calculations. . . . .	55
12	Averaged particle concentration, $\text{cm}^{-3}$ on April 13, 2013. . . . .	62
13	Averaged particle concentration, $\text{cm}^{-3}$ on July 18, 2014. . . . .	63
14	Mass concentration ( $\mu\text{g}/\text{m}^3$ ) on April 13, 2013. . . . .	63

Figure		Page
15	Mass concentration ( $\mu\text{g}/\text{m}^3$ ) on July 18, 2014. . . . .	64
16	$B_{\text{sca}}$ Coefficients for April 13th, 2013. Look at the high peak at 7:49AM. . . . .	70
17	$\text{Log}(F_{11})$ Müeller matrix element for an ensemble of oblate spheroids as a function of scattering angle $\theta$ and relative core size $q$ for April 13, 2013 at 7:49 AM. . . . .	71
18	$\text{Log}(F_{11})$ Müeller matrix element for an ensemble of oblate spheroids as a function of scattering angle $\theta$ and relative core size $q$ for April 13, 2013 at 8:04 AM. . . . .	72
19	$F_{22}/F_{11}$ Müeller matrix element for an ensemble of oblate spheroids as a function of scattering angle $\theta$ and relative core size $q$ for April 13, 2013 at 7:49AM. . . . .	73
20	$F_{22}/F_{11}$ Müeller matrix element for an ensemble of oblate spheroids as a function of scattering angle $\theta$ and relative core size $q$ for April 13, 2013 at 8:04AM. . . . .	74
21	$F_{33}/F_{11}$ Müeller matrix element for an ensemble of oblate spheroids as a function of scattering angle $\theta$ and relative core size $q$ for April 13, 2013 at 7:49AM. . . . .	75
22	$F_{33}/F_{11}$ Müeller matrix element for an ensemble of oblate spheroids as a function of scattering angle $\theta$ and relative core size $q$ for April 13, 2013 at 8:04AM. . . . .	76
23	$F_{44}/F_{11}$ Müeller matrix element for an ensemble of oblate spheroids as a function of scattering angle $\theta$ and relative core size $q$ for April 13, 2013 at 7:49AM. . . . .	77
24	$F_{44}/F_{11}$ Müeller matrix element for an ensemble of oblate spheroids as a function of scattering angle $\theta$ and relative core size $q$ for April 13, 2013 at 8:04AM. . . . .	78
25	$F_{12}/F_{11}$ Müeller matrix element for an ensemble of oblate spheroids as a function of scattering angle $\theta$ and relative core size $q$ for April 13, 2013 at 7:49AM. . . . .	79
26	$F_{12}/F_{11}$ Müeller matrix element for an ensemble of oblate spheroids as a function of scattering angle $\theta$ and relative core size $q$ for April 13, 2013 at 8:04AM. . . . .	80

Figure		Page
27	$F_{34}/F_{11}$ Müller matrix element for an ensemble of oblate spheroids as a function of scattering angle $\theta$ and relative core size $q$ for April 13, 2013 at 7:49AM. . . . .	81
28	$F_{34}/F_{11}$ Müller matrix element for an ensemble of oblate spheroids as a function of scattering angle $\theta$ and relative core size $q$ for April 13, 2013 at 8:04AM. . . . .	82
29	Single scattering albedo retrievals for April 13th, 2013. . . . .	83
30	$B_{\text{sca}}$ Coefficients for July 18th, 2014. . . . .	87
31	$\text{Log}(F_{11})$ Müller matrix element for an ensemble of oblate spheroids as a function of scattering angle $\theta$ and relative core size $q$ for July 18, 2014 at 14:53 hrs. . . . .	88
32	$\text{Log}(F_{11})$ Müller matrix element for an ensemble of oblate spheroids as a function of scattering angle $\theta$ and relative core size $q$ for July 18, 2014 at 15:08 hrs. . . . .	89
33	$F_{22}/F_{11}$ Müller matrix element for an ensemble of oblate spheroids as a function of scattering angle $\theta$ and relative core size $q$ for July 18, 2014 at 14:53 hrs. . . . .	90
34	$F_{22}/F_{11}$ Müller matrix element for an ensemble of oblate spheroids as a function of scattering angle $\theta$ and relative core size $q$ for July 18, 2014 at 15:08 hrs. . . . .	91
35	$F_{33}/F_{11}$ Müller matrix element for an ensemble of oblate spheroids as a function of scattering angle $\theta$ and relative core size $q$ for July 18, 2014 at 14:53 hrs. . . . .	92
36	$F_{33}/F_{11}$ Müller matrix element for an ensemble of oblate spheroids as a function of scattering angle $\theta$ and relative core size $q$ for July 18, 2014 at 15:08 hrs. . . . .	93
37	$F_{12}/F_{11}$ Müller matrix element for an ensemble of oblate spheroids as a function of scattering angle $\theta$ and relative core size $q$ for July 18, 2014 at 14:53 hrs. . . . .	94
38	$F_{12}/F_{11}$ Müller matrix element for an ensemble of oblate spheroids as a function of scattering angle $\theta$ and relative core size $q$ for July 18, 2014 at 15:08 hrs. . . . .	95

Figure		Page
39	$F_{34}/F_{11}$ Müller matrix element for an ensemble of oblate spheroids as a function of scattering angle $\theta$ and relative core size $q$ for July 18, 2014 at 14:53 hrs. . . . .	96
40	$F_{34}/F_{11}$ Müller matrix element for an ensemble of oblate spheroids as a function of scattering angle $\theta$ and relative core size $q$ for July 18, 2014 at 15:08 hrs. . . . .	97
41	Single scattering albedo retrievals for July 18th, 2014. . . . .	98
42	Aerosol particle at $200\mu\text{m}$ scale resolution. The threads in the figure are the composition of special filters used in the filtering process. . . . .	102
43	Aerosol particle at $500\mu\text{m}$ scale resolution. The threads in the figure are the composition of special filters used in the filtering process. . . . .	103

## CHAPTER 1

### Introduction

The word aerosol [1] denotes an aerial colloid, a suspensoid with air as the medium with radius between  $0.5 \times 10^{-3} \mu\text{m}$  to  $20 \mu\text{m}$  approximately. They arise from emissions of particles and from the conversion of certain gases to particles in the atmosphere [2]. Aerosols affect climate forcing through scattering and absorption, and both attenuate or extinct the incoming solar radiation and the outgoing terrestrial IR radiation helping in this way the earth's radiation balance.

Chemical and physical properties are used to classify aerosols such as composition, particle concentration, geometric shape, and size distribution. These properties are often hard to describe completely in situ due to the continuum mixing state of them due to the constant change of the medium. Field measurements of these properties are carried out sometimes by using ground based instruments like radiometers or nephelometers and compared with retrieval algorithms [3]. These computer algorithms are very important when studying aerosols, not only to determine their physical properties but also to describe their behavior and their impact on the environment in both short and long term.

On the other side, the study of light scattering by small aerosol particles allow to understand the interaction process under a deeper analysis which involves electromagnetic theory, statistical analysis and numerical algorithms. This study considers particle properties like geometric shape, orientation and composition in the analysis of the particles, as well as a complete mathematical approach of the scattering problem through complicated series expansions where both associate Legendre and spherical Bessel functions are of crucial importance. In the computational field, discretization of the mathematical formulations, stabilization of

the mathematical methods and accuracy of them are always taken into account. Fortunately all these computational issues were already coded into the T-matrix approximation developed by Waggoner [4], and modeled by Mishchenko [5]. Also, based in these formulation, it was possible to study different aerosol geometries which can be randomly oriented or composed of different materials. Additionally, in other conditions where the particle or system of particles are under effects of relative humidity (RH), or when the aerosol masses are composed of particles with different refractive indexes, these mathematical approaches are still valid under certain assumptions.

In the following chapters, the concept of aerosols is given and its properties in the troposphere, its optical properties and stochastic behavior when they are grouped in clusters. Here also is presented the mathematical analysis of its interaction with light, the physics formulation of the process and its solution. Additionally, two mathematical codes are studied and tailored to two specific days of low and high relative humidity in the El Paso del Norte Airshed.

## 1.1 Atmospheric Aerosols

When studying atmospheric aerosols, their optical properties are used for classification. These properties are particle concentration, size, shape, and internal structure. The sizes of aerosol particles ranges in different equivalent diameters. Particle detectors can measure different order of magnitudes in aerosol diameters, which can range from 0.001 to more than 20  $\mu\text{m}$ . For this reason, it is convenient to divide the range of aerosol diameters in bins of size ranges (modes) of similar physical properties. Three important modes are the nucleation mode, the accumulation mode, and the coarsening mode. The nucleation mode consists of particles with diameters that range on about  $10^{-3}$  -  $0.1\mu\text{m}$ . This particles have short residence times in the air and they coagulate quickly with other particles to form

new ones. The accumulation mode consists of particles with diameter in the range of  $0.1\text{-}2\mu\text{m}$ . These particles are important because they can be suspended on the air for long periods of time and can be transported by wind long distances. The coarse mode consists of particles with diameters larger than  $2\mu\text{m}$ . These particles are more affected by gravity forces and therefore they also have short residence time in the air.

One important dimensionless parameter for aerosol particles is the one related to its size, the characteristic size parameter,  $x_{\text{eff}}$ , which is defined as:

$$x_{\text{eff}} = \frac{2\pi n r_{\text{eff}}}{\lambda} \quad (1)$$

where  $\lambda$  is the wavelength of incident radiation,  $n$  is the refractive index of the external medium and  $r$  is the characteristic size of the particle (e.g., the radius of a droplet, or the side of a cubic crystal). Also, the number concentration  $N$  which represent the number of particles per cubic centimeter is a parameter that help to describe the distribution of particles when they are grouped in sizes. As an example, the number concentration of sea-salt particles in the open ocean is usually around  $250\text{ cm}^{-3}$  (250 particles per cubic centimeter) and the value of  $N$  is dominated by small particles with typical sizes around  $0.3\text{ }\mu\text{m}$ . The particle size distribution (PSD) describes how the aerosols are distributed in sizes and is expressed as a function of radius  $f(r)$  and more often modeled using the log-normal law:

$$f(r) = \frac{1}{\sqrt{2\pi}\sigma r} \exp\left\{-\frac{\ln^2(r/r_0)}{2\sigma^2}\right\} \quad (2)$$

where  $r$  is the radius of a spherical homogeneous particle,  $r_0 = 0.3\mu\text{m}$  is the effective radius (which is related to the projected surface area of the particle that scatters radiation), and  $\sigma$  is the standard deviation corresponding to this

distribution. The log-normal distribution often provides a good fit for atmospheric aerosol distributions and is regularly used in many atmospheric applications [2]. The area-weighted mean or effective radius  $r_{\text{eff}}$  is an important quantity in aerosol optics and it is expressed as follows

$$r_{\text{eff}} = \frac{\int_0^{\infty} r^3 f(r) \, dr}{\int_0^{\infty} r^2 f(r) \, dr} \quad (3)$$

and it is related to the average particle size of the distribution. For the log-normal particle size distribution from eq. (2) the following relation applies

$$r_{\text{eff}} = r_0 \exp(2.5\sigma^2) \quad (4)$$

In media where aerosol particles form part of it like air for example, scattering of light always occur. When an electromagnetic wave interacts with aerosol particles, this interaction depends on the relative complex refractive index of the particle  $n = m - ik$ , where  $k$  represents the ability of the particle to absorb electromagnetic energy. The refractive index of water, for example is approximately 1.33 in the visible and its complex refractive index is  $1.0000 \times 10^{-9}$  indicating that the water is very low absorptive of light radiation and it can be neglected in the visible, infrared, and also in the ultraviolet regime where  $k = 1.1000 \times 10^{-7}$ .

Table 1 shows us the refractive values of some aerosols for some wavelengths from ultraviolet to infrared. As it was mentioned, values of  $m$  give us both the scattering index of the particle and  $k$  the absorption index of refraction of the particle.

When describing the mass concentration of aerosol particles in the atmosphere, it is observed that most of the concentration of aerosol particles are in the first

Table 1: The refractive index  $n = m - ik$  of oceanic, water-insoluble (mainly, dust), water-soluble (sulfates, nitrates, etc.), and soot aerosol, respectively (courtesy of Kokhanovsky, A. [6])

$\lambda$ , nm	$n$		$k$		$n$		$k$		$n$		$k$	
300	1.40	$5.8 \cdot 10^{-7}$	1.53	$8.0 \cdot 10^{-3}$	1.53	$8.0 \cdot 10^{-3}$	1.74	0.47				
400	1.39	$9.9 \cdot 10^{-9}$	1.53	$8.0 \cdot 10^{-3}$	1.53	$5.0 \cdot 10^{-3}$	1.75	0.46				
550	1.38	$4.3 \cdot 10^{-9}$	1.53	$8.0 \cdot 10^{-3}$	1.53	$6.0 \cdot 10^{-3}$	1.75	0.44				
694	1.38	$5.0 \cdot 10^{-8}$	1.53	$8.0 \cdot 10^{-3}$	1.53	$7.0 \cdot 10^{-3}$	1.75	0.43				
860	1.37	$1.1 \cdot 10^{-6}$	1.52	$8.0 \cdot 10^{-3}$	1.52	$1.2 \cdot 10^{-2}$	1.75	0.43				
1060	1.37	$6.0 \cdot 10^{-5}$	1.52	$8.0 \cdot 10^{-3}$	1.52	$1.7 \cdot 10^{-2}$	1.75	0.44				
1300	1.37	$1.4 \cdot 10^{-4}$	1.46	$8.0 \cdot 10^{-3}$	1.51	$2.0 \cdot 10^{-2}$	1.76	0.45				
1800	1.35	$3.1 \cdot 10^{-4}$	1.33	$8.0 \cdot 10^{-3}$	1.46	$1.7 \cdot 10^{-2}$	1.79	0.48				
2000	1.35	$1.1 \cdot 10^{-3}$	1.26	$8.0 \cdot 10^{-3}$	1.42	$8.0 \cdot 10^{-3}$	1.80	0.49				
2500	1.31	$2.4 \cdot 10^{-3}$	1.18	$9.0 \cdot 10^{-3}$	1.42	$1.2 \cdot 10^{-2}$	1.83	0.51				

2000 m (or 2 km) of the troposphere, inside a region that is known as the *Boundary Layer*. The boundary layer is the region from the surface to about 0.5-3 km altitude and its height changes during the day.

Figure 1 shows the concentration of aerosol particles expressed by its optical depth for the first 10 km in the city of El Paso for a light wavelength of 500 nm ( $1 \text{ nm} = 10^{-9} \text{ m}$ ). This figure is a re-creation of the values of optical thickness vertical profile of Elterman L., at 500 nm [7], and weighted with local values for the surface of El Paso obtained from a visible multifilter radiometer like the one in fig. 10. This figure clearly shows that most of the concentrations of aerosols are in the first 2 km of the troposphere (orange region), inside the boundary layer and the remaining region can be neglectable of aerosols.

In the El Paso del Norte topography, most of the aerosols correspond to mineral dust and sand which originate from the land surface, and with some contributions of anthropogenic sources. Mineral dust and sand are the primary elements that reduce visibility and also affect the health of the residents in the region, especially in high-wind events where the concentration of particles can reduce the visibility to 5%.

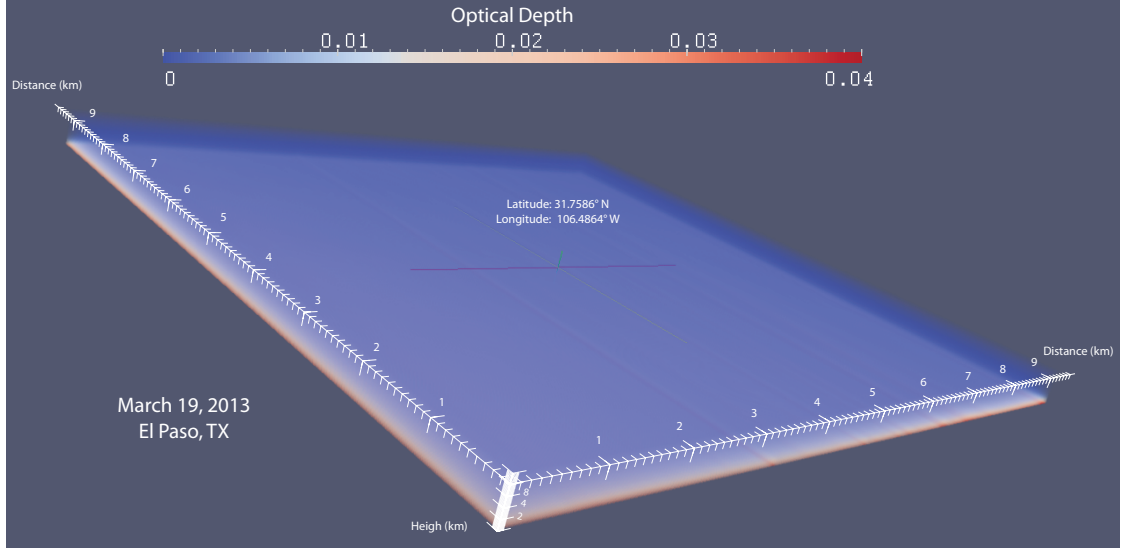


Figure 1: Aerosol vertical distribution at 500 nm, for El Paso, TX. Notice the concentration of aerosols are mainly in the first two km of the troposphere approximately, a region called boundary layer

### 1.1.1 Atmospheric properties of atmospheric aerosols

Light is scattered by aerosol particles suspended in the air. Processes of light scattering mostly dominate over processes of absorption in the visible region. The reduction in the intensity of a direct beam during its propagation through an aerosol medium is determined simultaneously by absorption and scattering processes. Emission, which is negligible at optical wavelengths, is not considered in light scattering processes.

All solar radiation with wavelength below  $0.28 \mu\text{m}$  is absorbed by the Earth's atmosphere, above the troposphere. The troposphere is a region that starts at the surface and extends to between 9 km at the poles and 17 km at the equator, although this extension can vary with the weather.

Above the troposphere there are several layers where different phenomena occurs. Figure 2 depicts what is called the lower atmosphere and its layers along with the distribution of the temperatures and pressures with the altitude.

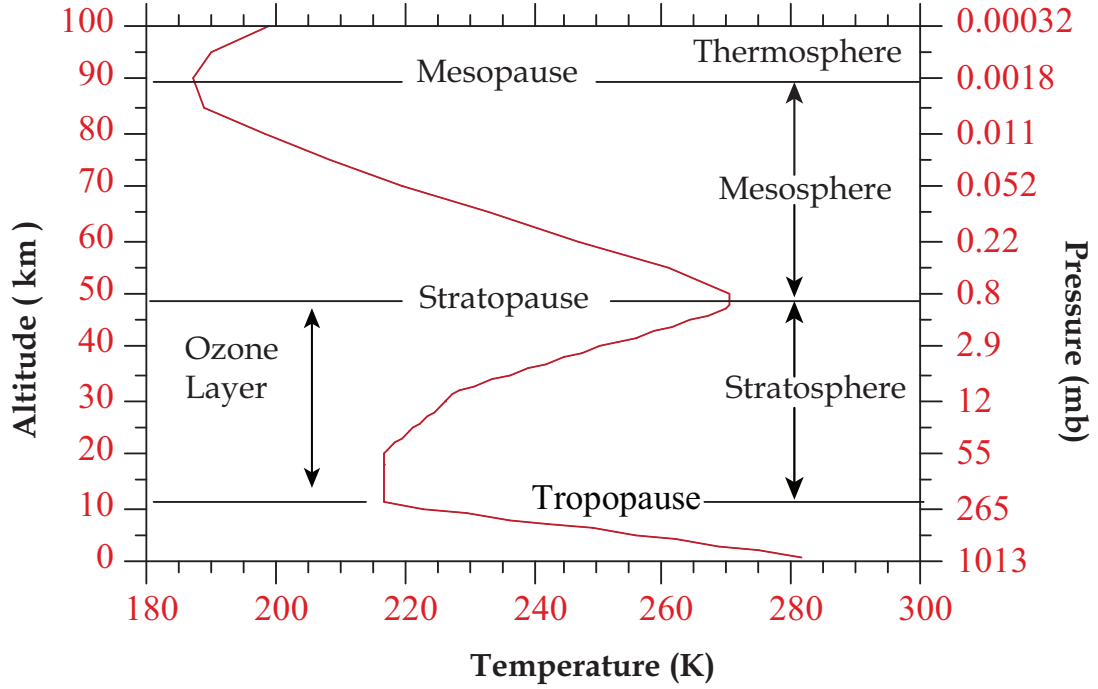


Figure 2: Layers of the Earth's lower atmosphere, and the structure of the temperature and pressure with the altitude. Courtesy of Jacobson M. Z. [8]

Gas absorption is important only in the thermosphere (320-380 km), mesosphere (50-85 km approximately) and stratosphere (12-51 km, approximately), where  $N_2$  and  $O_2$  together prevent those wavelengths less than  $0.245 \mu m$  reaching the troposphere [8].

In the troposphere only  $NO_2$  affects more solar radiation, especially for wavelengths less than  $0.50 \mu m$  and moderately for wavelengths of  $0.5-0.6 \mu m$ . At wavelengths less than  $0.32 \mu m$  however,  $O_3$  has a larger effect than  $NO_2$  on light attenuation or light extinction. On the other side, the only process of gas scattering by gas in the atmosphere is Rayleigh Scattering which is produced by  $N_2$  and  $O_2$  mainly [4].

In summary, gases scatter short wavelength much more effectively than they do long wavelength and also their mixing ratios are too low in comparison with the effect of scattering and absorption by particles. It is for this reason that the study

of visibility is concentrated only on aerosol particles in the troposphere.

In the case of absorption, the imaginary part  $k$ , of the refractive index is an important parameter because the greater the absorption of a particle, the lesser the scattering, since absorption hinders scattering. Small particles with radii  $r_i \ll \lambda$  are relatively inefficient absorbers of radiation. The strongest absorptive particle in the visible and ultraviolet spectrum region is black carbon, which is the main component of soot. Others are  $\text{Fe}_2\text{O}_3$ ,  $\text{Al}_2\text{O}_3$ , and certain organic compounds [8].

The description of range and regimen of particles and wavelengths is important when we study the effects of extinction of solar radiation due to the interaction with aerosol particles. When a particle diameter  $d_i$  is much smaller than the wavelength of light ( $d_i < 0.03 \lambda$ ), it is said that the particles are in the Rayleigh regime. For diameter particles in  $0.03 \lambda < d_i < 32 \lambda$ , the particles are in the Mie region, and the absorption and scattering are approximated with Mie's solution to Maxwell equations (or with the T-matrix approximation, which has a wider application for different shapes of particles than Mie's approximation which only deals with spherical shapes). Finally, for diameters of  $d_i > 32 \lambda$ , the particles are in the Geometric regime.

### 1.1.2 Optical parameters of atmospheric aerosols

An important property of aerosols is the *optical depth*, which is a measure of the transparency (dimensionless), or the quantity of light radiation removed from a beam by scattering or absorption.

$$\tau(z, \nu) = - \int_{z_1}^{z_2} B_{\text{ext}}(z', \nu) dz' \quad (5)$$

The negative sign is used because we shall adopt the convention that  $z$  and  $\tau$  run in opposite directions.  $\tau_\nu(z)$  gives the integrated extinction of radiation along the

z-direction in the segment  $(z_2 - z_1)$ . The term  $B_{\text{ext}}$  is the extinction coefficient which is defined as the attenuation of radiation after passing through a medium,  $\nu$  is the wavelength frequency and  $z$  is the vertical coordinate.

The single scattering albedo of a particle is a measure of particle scattering cross section relative to its total extinction cross section (absorption plus scattering cross sections) and is mathematically defined by the equation (6) as follows

$$\omega = \frac{C_{\text{sca}}}{C_{\text{ext}}} = \frac{C_{\text{sca}}}{C_{\text{abs}} + C_{\text{sca}}} \quad (6)$$

Another important parameter which describes angular distribution of the scattered radiation is the phase function  $P(\theta)$  or the scattering phase function and it is defined as the scattered intensity at a certain angle  $\theta$ :

$$P(\theta) = \frac{I(\theta)}{\int_0^\pi I(\theta) \sin \theta d\theta} \quad (7)$$

where  $\theta$  is the scattering angle and  $I(\theta)$  is the intensity [2]. The Asymmetry parameter  $g$  is defined similarly as the intensity weighted average of the cosine of the scattering angle:

$$\begin{aligned} g &= \frac{1}{2} \frac{\int_0^\pi \cos \theta I(\theta) \sin \theta d\theta}{\int_0^\pi I(\theta) \sin \theta d\theta} \\ &= \frac{1}{2} \int_0^\pi \cos \theta P(\theta) \sin \theta d\theta \end{aligned} \quad (8)$$

where the factor  $1/2$  ensures values of  $g=1$  for light forward scattered completely at  $\Theta = 0^\circ$ , and of  $g = -1$  for light backward scattered completely at  $\Theta = 180^\circ$ . On the other hand, a value of  $g = 0$  indicates that the radiation is scattered isotropically.

### 1.1.3 The Lognormal Distribution

The size distribution function is the number of particles per unit volume with diameters between  $D_p$  and  $D_p + dD_p$ . This number of particles or number concentration is normalized by the range of particle diameters [9]:

$$n(D_p) = \frac{dN}{dD_p} \quad (9)$$

and when the order of magnitude is big in the range of aerosol diameters, the logarithm scale is used:

$$n(\log(D_p)) = \frac{dN}{d\log(D_p)} \quad (10)$$

which is the form more used in atmospheric aerosol calculations.

Other distributions are also applied to aerosol particles like exponential, power law, Khrgian-Mazin, Nukiyama-Tanasawa, and Rosin-Rammler, but these distributions correspond to special situations and they were selected empirically to fit the wide range and skewed shape of most aerosol size distributions [9].

The normal distribution is widely applied elsewhere but is not suitable for most aerosol particle size distributions because most aerosols exhibit a skewed (long tail at large sizes) distribution function and this distribution is symmetrical. The lognormal makes the skewed behavior of the particles symmetrical and also correct the singularity of the normal distribution which consider negative values on diameters, which does not have physical meaning. Also, the lognormal distribution is most useful in situations where the ratio of the largest to the smallest value is greater than about 10.

The number frequency function in normal distribution is given by

$$df(D_p) = \frac{1}{\sigma\sqrt{2\pi}} \exp\left(-\frac{(D_p - \bar{D}_p)^2}{2\sigma^2}\right) dD_p \quad (11)$$

where the  $\bar{D}_p$  is the arithmetic mean diameter and  $\sigma$  is the standard deviation, defined as

$$\sigma = \left(\frac{\sum n_i (D_i - \bar{D}_p)^2}{N - 1}\right)^{\frac{1}{2}} \quad (12)$$

Now we use the geometrical mean  $D_g = (D_1 D_2 D_3 \dots D_N)^{\frac{1}{2}}$  with the conversion

$$\ln D_g = \frac{\sum n_i \ln D_i}{N} \quad (13)$$

and the standard deviation is

$$\ln \sigma_g = \left[\frac{\sum n_i (\ln D_i - \ln D_g)^2}{N - 1}\right]^{\frac{1}{2}} \quad (14)$$

which is a dimensionless quantity with a value equal or greater than 1. With this change the new frequency deviation can be expressed as

$$df = \frac{1}{\sqrt{2\pi} D_p \ln \sigma} \exp\left(-\frac{(\ln D_p - \ln D_g)^2}{2(\ln \sigma_g)^2}\right) d \ln D_p \quad (15)$$

which gives the fraction of the particles having diameters whose logarithms lie between  $\ln D_p$  and  $\ln D_p + d \ln D_p$ .

The normal and lognormal distributions have the following properties which can be used to fit particle data.

- In the normal distribution, 95% of the particles lie in the range  $\bar{D} + 2\sigma$ , as for the log-normal distribution this percentage lies in  $\exp(\ln D_g + 2 \ln D_g)$
- One standard deviation in the normal distribution follows  $\sigma = D_{84\%} - D_{50\%}$ , as for the log-normal distribution, the geometric standard deviation:

$$\sigma_g = \frac{d_{84\%}}{d_{50\%}} = \frac{d_{50\%}}{d_{16\%}} = \left( \frac{d_{84\%}}{d_{16\%}} \right)^{\frac{1}{2}} \quad (16)$$

#### 1.1.4 The volume-weighted method

The volume-weighted method [10] is a technique which calculates the refractive indexes by knowing the mass fraction and density of the species of a composite medium. The method is shown in equations (17) and (18). The mean refractive index ( $\bar{n} = \bar{m} + i\bar{k}$ ) is computed with the real refractive index for species  $j(m_j)$ , the mass fraction of species  $j(X_j)$ , and the species density ( $\rho_j$ , g/cm<sup>3</sup>). The mean imaginary part of the complex refractive index is computed using the value corresponding to each species ( $k_j$ ):

$$\bar{n} = \bar{\rho} \sum_j \frac{X_j m_j}{\rho_j} + \bar{\rho} \sum_j \frac{X_j k_j}{\rho_j} i \quad (17)$$

the mean density  $\bar{\rho}$  is computed with

$$\bar{\rho}^{-1} = \sum_j \frac{X_j}{\rho_j} \quad (18)$$

## 1.2 Extinction by an arbitrary particle

When a beam of light interacts with a particle, the amount and angular distribution of the light scattered and the amount absorbed by the particle, depends on its shape, size, and the internal composition. The different possibilities of face the problem can be simplified if we take into account some features common to the phenomena of scattering and absorption by small particles. In this chapter the mathematical and physical framework will be described in some detail to underly the specific problem of the scattering of light by small arbitrary finite particles, and the effects of relative humidity in the process.

### 1.2.1 Scattering, and absorption by an arbitrary finite particle

When an incident electromagnetic beam of electric field  $\mathbf{E}$  and magnetic field  $\mathbf{H}$  impinges on a small particle, several effects can be caused. When the energy is absorbed into the particle, the process is called *absorption* and the energy is converted into heat. If the energy is scattered into any direction, this process is called *scattering*. As a result, the energy is reduced by an amount equal to the sum of the absorbed and scattered energy and it is called *extinction*. Extinction (or attenuation), is the effect that produces a diminishing in intensity of radiation through a medium due to either absorption or scattering, or both together.

The extinction, scattering and absorption cross sections, are characteristics of the scattering object and of the beam, and has dimensions of area. The product of the scattering cross section  $C_{\text{sca}}$  and the incident monochromatic energy flux gives the total monochromatic power removed from the incident wave as a result of scattering of the incident radiation in all directions. Analogously, the product of the absorption cross section  $C_{\text{abs}}$  and the incident monochromatic energy flux gives the total monochromatic power removed from the incident wave as a result of absorption of light by the object [5]. In consequence, the extinction cross section

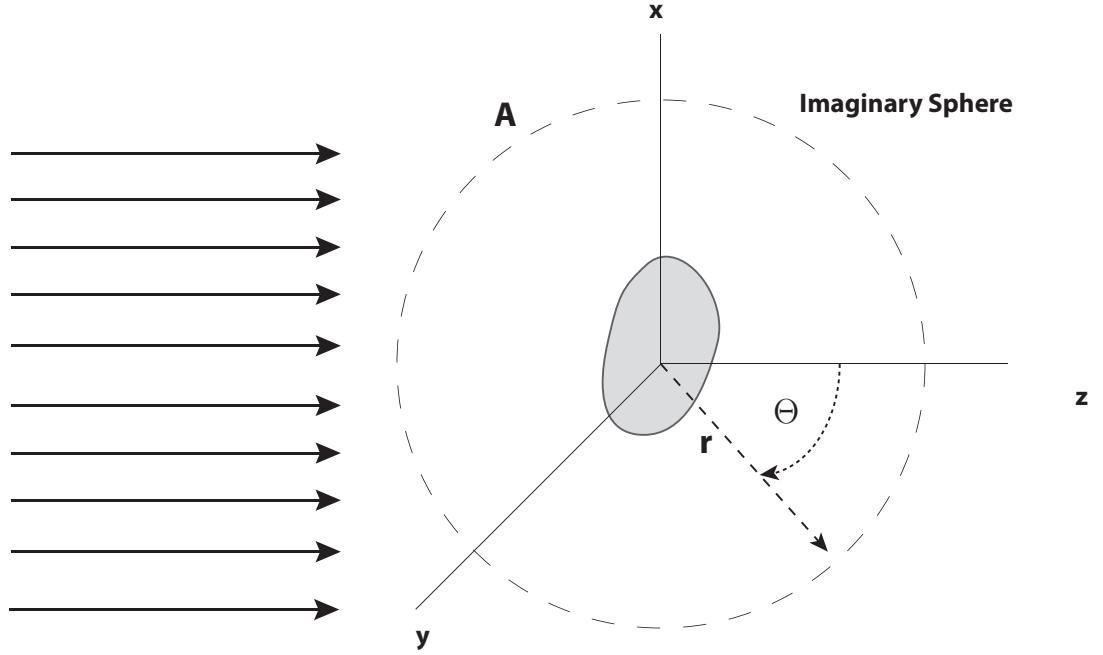


Figure 3: Extinction by a single particle. Courtesy of Bohren, C. F. [11].

$C_{\text{ext}}$  is the sum of the scattering and absorption cross sections and, when multiplied by the incident monochromatic energy flux it is equal to the total monochromatic power removed from the incident light by the combined effect of scattering and absorption is obtained.

To determine the total optical cross sections, an imaginary non-absorbing medium as a sphere of radius  $r$  and area  $A$  is constructed around the particle as is shown in figure 3. The net rate at which electromagnetic energy crosses the surface  $A$  of this sphere is always non-negative and is equal to the power absorbed by the particle:

$$W_{\text{abs}} = - \int_A \mathbf{S} \cdot \hat{\mathbf{e}}_r dA \quad (19)$$

here  $\mathbf{S}$  is the Poynting vector which specifies the magnitude and direction of the

rate of transfer of electromagnetic energy at all points of space, namely

$$\mathbf{S} = \mathbf{E} \times \mathbf{H} \quad (20)$$

or for the time averaged Poynting vector for time harmonic fields

$$\langle \mathbf{S} \rangle = \frac{1}{2} \Re \{ \mathbf{E}_c \times \mathbf{H}_c^* \} \quad (21)$$

where  $\Re$  denotes real part of the complex term, the subindex  $c$  denotes complex vector, and  $\mathbf{H}_c^*$  denotes the complex conjugate of the magnetic field.

Now,  $W_{\text{abs}}$  can be written as a combination of three terms:

$$W_{\text{abs}} = W_{\text{inc}} - W_{\text{sca}} + W_{\text{ext}} \quad (22)$$

where

$$W_{\text{inc}} = - \int_A \mathbf{S}_{\text{inc}} \cdot \hat{\mathbf{e}}_r dA \quad (23a)$$

$$W_{\text{sca}} = \int_A \mathbf{S}_{\text{sca}} \cdot \hat{\mathbf{e}}_r dA \quad (23b)$$

$$W_{\text{ext}} = - \int_A \mathbf{S}_{\text{ext}} \cdot \hat{\mathbf{e}}_r dA \quad (23c)$$

$W_{\text{inc}}$  vanishes because the surrounding medium is nonabsorbing and  $\mathbf{S}_{\text{inc}}$  is a constant vector, whereas  $W_{\text{sca}}$  is the rate at which the scattered energy crosses the surface  $A$  in the outward direction. Therefore,  $W_{\text{ext}}$  is equal to the sum of the energy scattering rate and the energy absorption rate:

$$W_{\text{abs}} = W_{\text{sca}} + W_{\text{ext}} \quad (24)$$

And now, the  $W_{\text{ext}}$ ,  $W_{\text{abs}}$ , and  $W_{\text{sca}}$ , can be related with  $I_{\text{inc}}$  which is the incident

radiance and the respective cross section values

$$C_{\text{ext}} = \frac{W_{\text{ext}}}{I_{\text{inc}}} \quad (25\text{a})$$

$$C_{\text{abs}} = \frac{W_{\text{abs}}}{I_{\text{inc}}} \quad (25\text{b})$$

$$C_{\text{sca}} = \frac{W_{\text{sca}}}{I_{\text{inc}}} \quad (25\text{c})$$

The mathematical derivation of the cross sections in the eqs. (25a)-(25c), is based on the solution of the wave equation by vector spherical harmonics. The next section will cover this mathematical formulation and the solution of the problem for an spherical particle. The spectral aerosol extinction coefficient  $B_{\text{ext}}(\mu\text{m}^{-1})$  is important to determine levels of extinction by particles or by a system of particles. For a specific number concentration  $N$  of particles, we have

$$B_{\text{ext}} = NC_{\text{ext}} \quad (26)$$

also, the equivalent spectral aerosol scattering coefficient is defined by

$$B_{\text{sca}} = NC_{\text{sca}} \quad (27)$$

and the equivalent spectral aerosol absorption coefficient by

$$B_{\text{abs}} = NC_{\text{abs}} \quad (28)$$

those are important physical quantities that will allow us to calculate levels of extinction, scattering and absorption of light. We also recall that

$$C_{\text{ext}} = C_{\text{abs}} + C_{\text{sca}} \quad (29)$$

where  $C_{\text{ext}}$ ,  $C_{\text{abs}}$ , and  $C_{\text{sca}}$  are the extinction, absorption, and scattering cross-section respectively.

### 1.2.2 General formulation of the scattering problem (Mie Theory)

The calculation of the electromagnetic fields inside and scattered by a particle due to its interaction with light is an interesting problem treated in many books (see for example [11], [12], and [13]), where the main idea is solving the vector wave equations for the fields  $\mathbf{E}$  and  $\mathbf{H}$ . The field inside the particle is denoted by  $(\mathbf{E}_1, \mathbf{H}_1)$ ; the field  $(\mathbf{E}_2, \mathbf{H}_2)$  in the medium surrounding the particle is the superposition of the incident field  $(\mathbf{E}_i, \mathbf{H}_i)$  and the scattered field  $(\mathbf{E}_s, \mathbf{H}_s)$  as it is shown in fig. 4. Then

$$\mathbf{E}_2 = \mathbf{E}_i + \mathbf{E}_s$$

$$\mathbf{H}_2 = \mathbf{H}_i + \mathbf{H}_s$$

where

$$\mathbf{E}_i = \mathbf{E}_0 \exp(i\mathbf{k} \cdot \mathbf{x} - i\omega t)$$

$$\mathbf{H}_i = \mathbf{H}_0 \exp(i\mathbf{k} \cdot \mathbf{x} - i\omega t)$$

and  $\mathbf{k}$  is the wave vector appropriate to the surrounding medium,  $\omega$  is the frequency of the field and  $t$  is the propagation time. The fields  $\mathbf{E}$  and  $\mathbf{H}$  are divergence-free, not independent and must satisfy the Maxwell's equations

$$\nabla \cdot \mathbf{E} = 0 \tag{32a}$$

$$\nabla \cdot \mathbf{H} = 0 \tag{32b}$$

$$\nabla \times \mathbf{E} = i\omega\mu\mathbf{H} \tag{32c}$$

$$\nabla \times \mathbf{H} = -i\omega\varepsilon\mathbf{E} \tag{32d}$$

at the points where the permittivity of free space  $\varepsilon$  and the magnetic permeability  $\mu$  are continuous. The curl of (32c) and (32d) is

$$\nabla \times (\nabla \times \mathbf{E}) = i\omega\mu\nabla \times \mathbf{H} = \omega^2\varepsilon\mu\mathbf{E}$$

$$\nabla \times (\nabla \times \mathbf{H}) = -i\omega\varepsilon\nabla \times \mathbf{E} = \omega^2\varepsilon\mu\mathbf{H}$$

and by using the vector identity

$$\nabla \times (\nabla \times \mathbf{A}) = \nabla(\nabla \cdot \mathbf{A}) - \nabla \cdot (\nabla \mathbf{A}) \quad (34)$$

we obtain

$$\nabla^2 \mathbf{E} + k^2 \mathbf{E} = 0 \quad (35a)$$

$$\nabla^2 \mathbf{H} + k^2 \mathbf{H} = 0 \quad (35b)$$

where  $k^2 = \omega^2 \varepsilon \mu$ , and again  $\mu$  as the magnetic permeability, which measure the ability of magnetization of a material in response to a magnetic field, and  $\varepsilon$  is the complex permittivity. The complex permittivity can be expressed as

$$\varepsilon = \varepsilon_0(1 + \chi) + i \frac{\sigma}{\omega} \quad (36)$$

where  $\chi$  is the electric susceptibility (a measure of how fast a dielectric polarizes in response to an electric field),  $\sigma$  is the electric conductivity of the medium,  $\varepsilon_0$  is the permittivity of free space ( $\varepsilon_0 = 8.854187 \times 10^{-12}$  F/m), which is the material's ability to transmit an electric field, and again  $\omega$  is the angular frequency of the field.

The solution of equations (35a) and (35b) are based in the construction of two vector functions  $\mathbf{M}$  and  $\mathbf{N}$  consisted on the scalar function  $\psi$  and an arbitrary constant vector  $\mathbf{c}$  in the following way

$$\mathbf{M} = \nabla \times (\mathbf{c}\psi) \quad (37a)$$

$$\mathbf{N} = \frac{\nabla \times (\mathbf{M}}{k} \quad (37b)$$

proving that  $\mathbf{M}$  and  $\mathbf{N}$  satisfy the vector wave equation, they are divergent free, and satisfy the following properties

$$\nabla \cdot \mathbf{M} = 0 \quad (38a)$$

$$\nabla \times \mathbf{N} = k\mathbf{M} \quad (38b)$$

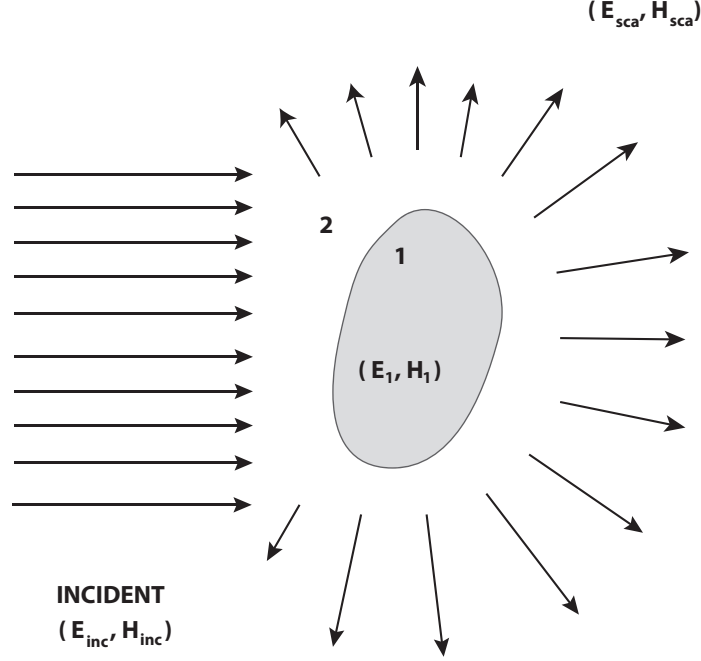


Figure 4: The incident field  $(\mathbf{E}_{\text{inc}}, \mathbf{B}_{\text{inc}})$  gives rise to a field  $(\mathbf{E}_1, \mathbf{B}_1)$  inside the particle and a scattered field  $(\mathbf{E}_{\text{sca}}, \mathbf{B}_{\text{sca}})$  in the surrounding medium of the particle labeled as 2. Courtesy of Bohren, F. C.[11].

then, we can write from eqs. (35a) and (35b) in similar way

$$\nabla^2 \mathbf{M} + k^2 \mathbf{M} = \nabla \times [\mathbf{c} (\nabla^2 \psi + k^2 \psi)] \quad (39)$$

and therefore  $\mathbf{M}$  will satisfy the vector wave equation if  $\psi$  is a solution of the scalar wave equation

$$\nabla^2 \psi + k^2 \psi = 0 \quad (40)$$

which can be written in spherical coordinates as

$$\frac{1}{r^2} \frac{\partial}{\partial r} \left( r^2 \frac{\partial \psi}{\partial r} \right) + \frac{1}{r^2 \sin \theta} \frac{\partial}{\partial \theta} \left( \sin \theta \frac{\partial \psi}{\partial \theta} \right) + \frac{1}{r^2 \sin^2 \theta} \frac{\partial^2 \psi}{\partial \phi^2} + k^2 \psi = 0 \quad (41)$$

and after using variable separation  $\psi(r, \theta, \phi) = R(r) \Theta(\theta) \Phi(\phi)$  yields us to the

three separated equations

$$\frac{d^2\Phi}{d\phi^2} + m^2\Phi = 0 \quad (42)$$

$$\frac{1}{\sin\theta} \frac{d}{d\theta} \left( \sin\theta \frac{d\Theta}{d\theta} \right) + \left[ n(n+1) - \frac{m^2}{\sin^2\theta} \right] \Theta = 0 \quad (43)$$

$$\frac{d}{dr} \left( r^2 \frac{dR}{dr} \right) + [k^2 r^2 - n(n+1)] R = 0 \quad (44)$$

where the separation constants  $m$  and  $n$  are determined by subsidiary conditions that  $\psi$  must satisfy.

The linearly independent solutions for  $\Phi(\phi)$  are

$$\begin{aligned} \Phi_e &= \cos m\phi \\ \Phi_o &= \sin m\phi \end{aligned} \quad (45)$$

where the subscripts  $e$  and  $o$  denote *even* and *odd* and  $\psi$  is a *single-valued* function of the azimuthal angle  $\phi$ :

$$\lim_{\nu \rightarrow 2\pi} \psi(\phi + \nu) = \psi(\phi) \quad (46)$$

and this is valid for all  $\phi$  except at points on the boundary between regions with different properties. The condition (46) requires that  $m$  to be an integer or zero; positive values of  $m$  are sufficient to generate all the linearly independent solutions to (42).

The solutions to (43) that are finite at  $\theta = 0$  and  $\theta = \pi$  are the *associated Legendre functions* of the first kind  $P_n^m(\cos\theta)$  of degree  $n$  and order  $m$ , where

$n = m, m + 1, \dots$ . When  $m = 0$ , the associated Legendre functions are the *Legendre polynomials*, which are denoted by  $P_n$ .

For the equation (44) it is used to make a change of variable  $\rho = kr$  and define the function  $Z = R\sqrt{\rho}$ , and it becomes

$$\rho \frac{d}{d\rho} \left( \rho \frac{dZ}{d\rho} \right) + \left[ \rho^2 - \left( n + \frac{1}{2} \right)^2 \right] Z = 0 \quad (47)$$

The linearly independent solutions to (47) are the *Bessel functions* of first and second kind  $J_\nu$  and  $Y_\nu$ , where the order  $\nu = n + \frac{1}{2}$  is half integral and the Bessel functions are written as

$$j_n(\rho) = \sqrt{\frac{\pi}{2\rho}} J_{n+\frac{1}{2}}(\rho) \quad (48)$$

$$y_n(\rho) = \sqrt{\frac{\pi}{2\rho}} Y_{n+\frac{1}{2}}(\rho)$$

where the constant factor  $\sqrt{\pi/2}$  is introduced for convenience. Any linear combination of  $j_n$  and  $y_n$  is also a solution to (44). Two such combinations that deserve attention are the *spherical Bessel functions of the third kind* (sometimes called spherical Hankel functions):

$$h_n^{(1)}(\rho) = j_n(\rho) + iy_n(\rho) \quad (49)$$

$$h_n^{(2)}(\rho) = j_n(\rho) - iy_n(\rho) \quad (50)$$

The generating functions that satisfy the scalar wave equation in spherical coordi-

nates are:

$$\psi_{emn} = \cos(m\phi) P_n^m(\cos \theta) z_n(kr) \quad (51)$$

$$\psi_{omn} = \sin(m\phi) P_n^m(\cos \theta) z_n(kr) \quad (52)$$

where  $z_n$  is any of the four spherical Bessel functions  $j_n$ ,  $y_n$ ,  $h_n^{(1)}$ , or  $h_n^{(2)}$ . Moreover, because of the *completeness* of the functions  $\cos m\phi$ ,  $\sin m\phi$ ,  $P_n^m(\cos \theta)$ ,  $z_n(kr)$ , any function that satisfies the scalar wave equation in spherical polar coordinates may be expanded as an infinite series in the functions (51) and (52).

The vector spherical harmonics generated by  $\psi_{emn}$  and  $\psi_{omn}$  are

$$\mathbf{M}_{emn} = \nabla \times (\mathbf{r}\psi_{emn}) \quad \mathbf{M}_{omn} = \nabla \times (\mathbf{r}\psi_{omn})$$

$$\mathbf{N}_{emn} = \frac{\nabla \times (\mathbf{M}_{emn})}{k} \quad \mathbf{N}_{omn} = \frac{\nabla \times (\mathbf{M}_{omn})}{k}$$

which, in component form, may be written

$$\begin{aligned}
\mathbf{M}_{emn} &= \frac{-m}{\sin \theta} \sin m\phi P_n^m(\cos \theta) z_n(\rho) \hat{\mathbf{e}}_\theta \\
&\quad - \cos m\phi \frac{dP_n^m(\cos \theta)}{d\theta} z_n(\rho) \hat{\mathbf{e}}_\phi
\end{aligned} \tag{53}$$

$$\begin{aligned}
\mathbf{M}_{omn} &= \frac{m}{\sin \theta} \cos m\phi P_n^m(\cos \theta) z_n(\rho) \hat{\mathbf{e}}_\theta \\
&\quad - \sin m\phi \frac{dP_n^m(\cos \theta)}{d\theta} z_n(\rho) \hat{\mathbf{e}}_\phi
\end{aligned} \tag{54}$$

$$\begin{aligned}
\mathbf{N}_{emn} &= \frac{z_n(\rho)}{\rho} \cos m\phi n(n+1) P_n^m(\cos \theta) \hat{\mathbf{e}}_r \\
&\quad + \cos m\phi \frac{dP_n^m(\cos \theta)}{d\theta} \frac{1}{\rho} \frac{d}{d\rho} [\rho z_n(\rho)] \hat{\mathbf{e}}_\theta \\
&\quad - m \sin m\phi \frac{dP_n^m(\cos \theta)}{\sin \theta} \frac{1}{\rho} \frac{d}{d\rho} [\rho z_n(\rho)] \hat{\mathbf{e}}_\phi
\end{aligned} \tag{55}$$

$$\begin{aligned}
\mathbf{N}_{omn} &= \frac{z_n(\rho)}{\rho} \sin m\phi n(n+1) P_n^m(\cos \theta) \hat{\mathbf{e}}_r \\
&\quad + \sin m\phi \frac{dP_n^m(\cos \theta)}{d\theta} \frac{1}{\rho} \frac{d}{d\rho} [\rho z_n(\rho)] \hat{\mathbf{e}}_\theta \\
&\quad + m \cos m\phi \frac{dP_n^m(\cos \theta)}{\sin \theta} \frac{1}{\rho} \frac{d}{d\rho} [\rho z_n(\rho)] \hat{\mathbf{e}}_\phi
\end{aligned} \tag{56}$$

where the  $r$ -component of  $N_{mn}$  is simplified by using the fact that  $P_n^m$  satisfies (43). Any solution to the field equations (35a) and (35a) can be now be expanded in an infinite series of the functions (53)-(56) .

### 1.2.3 Expansion of a plane wave in vector spherical harmonics

The scattering of a plane x-polarized wave, written in spherical polar coordinates as

$$\mathbf{E}_i = E_0 e^{ikr \cos \theta} \hat{\mathbf{e}}_x \tag{57}$$

where

$$\hat{\mathbf{e}}_x = \sin \theta \cos \phi \hat{\mathbf{e}}_r + \cos \theta \cos \phi \hat{\mathbf{e}}_\theta - \sin \phi \hat{\mathbf{e}}_\phi \quad (58)$$

by an arbitrary sphere. The first step toward the solution to this problem is expanding (57) in vector spherical harmonics:

$$\mathbf{E}_i = \sum_{m=0}^{\infty} \sum_{n=m}^{\infty} (B_{emn} \mathbf{M}_{emn} + B_{omn} \mathbf{M}_{omn} + A_{emn} \mathbf{N}_{emn} + A_{omn} \mathbf{N}_{omn}) \quad (59)$$

Because  $\sin m\phi$  is orthogonal to  $\cos m'\phi$  for all  $m$  and  $m'$  it follows that  $\mathbf{M}_{emn}$  and  $\mathbf{M}_{omn}$  are orthogonal and similarly,  $(\mathbf{N}_{omn}, \mathbf{N}_{emn})$ ,  $(\mathbf{M}_{omn}, \mathbf{N}_{omn})$ , and  $(\mathbf{N}_{emn}, \mathbf{M}_{emn})$ . The orthogonality properties of  $\cos m\phi$ , and  $\sin m\phi$  imply that all vector harmonics of different order  $m$  are mutually orthogonal. This orthogonality property implies that the coefficients in the expansion (59) are of the form

$$B_{emn} = \frac{\int_0^{2\pi} \int_0^\pi \mathbf{E}_i \cdot \mathbf{M}_{emn} \sin \theta d\theta d\phi}{\int_0^{2\pi} \int_0^\pi |\mathbf{M}_{emn}|^2 \sin \theta d\theta d\phi} \quad (60)$$

with similar expressions for  $B_{omn}$ ,  $A_{emn}$ , and  $A_{omn}$ . It follows from (53), (56), and (59), along with the orthogonality of the sine and cosine, that  $B_{emn} = A_{omn} = 0$  for all  $m$ , and  $n$  [11]. Moreover, the remaining coefficients vanish unless  $m = 1$  for the same reason. It comes also that because the incident field is finite at the origin [11],  $j_n(kr)$  will be the appropriate spherical Bessel function in the generating functions  $\psi_{o1n}$  and  $\psi_{e1n}$ , and reject  $y_n$  because of its misbehavior at the origin. In this case the radial dependence of the generating functions is specified by  $j_n$  and the subscript (1) is appended to vector spherical harmonics. Thus, the expansion

for  $\mathbf{E}_i$  has the form

$$\mathbf{E}_i = \sum_{n=1}^{\infty} \left( B_{o1n} \mathbf{M}_{o1n}^{(1)} + A_{e1n} \mathbf{N}_{e1n}^{(1)} \right) \quad (61)$$

After using orthogonalities properties and some algebraic manipulation the expansion coefficients  $\mathbf{M}_{o1n}^{(1)}$  and  $_{e1n} \mathbf{N}_{e1n}^{(1)}$ , become

$$B_{o1n} = i^n E_0 \frac{2n+1}{n(n+1)} \quad (62a)$$

$$A_{e1n} = -i E_0 i^n \frac{2n+1}{n(n+1)} \quad (62b)$$

and finally, we can express the expansion of the incident plane wave in spherical harmonics

$$\mathbf{E}_i = E_0 \sum_{n=1}^{\infty} i^n \frac{2n+1}{n(n+1)} \left( \mathbf{M}_{o1n}^{(1)} - i \mathbf{N}_{e1n}^{(1)} \right) \quad (63)$$

#### 1.2.4 The internal and scattering fields

When a plane  $x$ -polarized wave is incident on an homogeneous isotropic sphere of radius  $a$  the incident electric field can be expanded in an infinite series of vector spherical harmonics, and the corresponding incident magnetic field is obtained from the curl of (63):

$$\mathbf{H}_i = \frac{-k}{\omega\mu} E_0 \sum_{n=1}^{\infty} i^n \frac{2n+1}{n(n+1)} \left( \mathbf{M}_{o1n}^{(1)} - i \mathbf{N}_{e1n}^{(1)} \right) \quad (64)$$

We may also expand the scattered electromagnetic field  $(\mathbf{E}_s, \mathbf{H}_s)$  and the field  $(\mathbf{E}_1, \mathbf{H}_1)$  inside the sphere in vector harmonics with the same property that these expansions vanish for all  $m \neq 1$ . Also, finiteness at the origin requires that we take  $j_n(k_1 r)$ , where  $k_1$  is the wave number in the sphere, as the appropriate spherical Bessel functions for the generating functions for the vector harmonics inside the sphere. Thus, the expansion of the field  $(\mathbf{E}_1, \mathbf{H}_1)$

$$\begin{aligned}\mathbf{E}_1 &= \sum_{n=1}^{\infty} E_n \left( c_n \mathbf{M}_{o1n}^{(1)} - i d_n \mathbf{N}_{e1n}^{(1)} \right) \\ \mathbf{H}_1 &= \frac{-k_1}{\omega \mu_1} \sum_{n=1}^{\infty} E_n \left( d_n \mathbf{M}_{o1n}^{(1)} + i c_n \mathbf{N}_{e1n}^{(1)} \right)\end{aligned}\tag{65}$$

where  $E_n = i^n E_0 (2n+1)/n(n+1)$  and  $\mu_1$  is the permeability of the sphere.

In the region outside the sphere  $j_n$  and  $y_n$  are well behaved; therefore, the expansion of scattered field involves both of these functions. In this case we can use Hankel functions  $h_n^{(1)}$  and  $h_n^{(2)}$ . It is proved that only one of these functions is required by considering the asymptotic expansions of the Hankel functions of order  $\nu$  for large values of  $|\rho|$  (see for example [14]). In this case the expansion of the scattered field is therefore

$$\begin{aligned}\mathbf{E}_s &= \sum_{n=1}^{\infty} E_n \left( i a_n \mathbf{N}_{o1n}^{(3)} - b_n \mathbf{M}_{e1n}^{(3)} \right) \\ \mathbf{H}_s &= \frac{k}{\omega \mu} \sum_{n=1}^{\infty} E_n \left( i b_n \mathbf{N}_{o1n}^{(3)} + a_n \mathbf{M}_{e1n}^{(3)} \right)\end{aligned}\tag{66}$$

where the subscript (3) at the vector spherical harmonics mean that the radial dependence of the generating functions is specified by  $h_n^{(1)}$ . After using the prop-

erties of the orthogonality of  $\sin \phi$  and  $\cos \phi$ , the coefficients inside the particle  $c_n$  and  $d_n$  are obtained

$$c_n = \frac{\mu_1 j_n(x) [x h_n^{(1)}(x)]' - \mu_1 h_n^{(1)}(x) [x j_n(x)]'}{\mu_1 j_n(mx) [x h_n^{(1)}(x)]' - \mu h_n^{(1)}(x) [mx j_n(mx)]'} \quad (67)$$

$$d_n = \frac{\mu_1 m j_n(x) [x h_n^{(1)}(x)]' - \mu_1 m h_n^{(1)}(x) [x j_n(x)]'}{\mu m^2 j_n(mx) [x h_n^{(1)}(x)]' - \mu h_n^{(1)}(x) [mx j_n(mx)]'}$$

and the scattering coefficients

$$a_n = \frac{\mu m^2 j_n(mx) [x j_n(x)]' - \mu_1 j_n(x) [mx j_n(mx)]'}{\mu m^2 j_n(mx) [x h_n^{(1)}(x)]' - \mu_1 h_n^{(1)}(x) [mx j_n(mx)]'} \quad (68)$$

$$b_n = \frac{\mu_1 j_n(mx) [x j_n(x)]' - \mu j_n(x) [mx j_n(mx)]'}{\mu_1 j_n(mx) [x h_n^{(1)}(x)]' - \mu h_n^{(1)}(x) [mx j_n(mx)]'}$$

where the prime indicates differentiation with respect to the argument in parentheses and the size parameter  $x$  and the relative refractive index  $m$  are

$$x = ka = \frac{2\pi Na}{\lambda}$$

$$m = \frac{k_1}{k} = \frac{N_1}{N}$$

where  $N_1$  and  $N$  are the refractive indices of particle and medium, respectively.

The scattering coefficients can be simplified when introducing the Ricatti-Bessel

functions

$$\psi_n(\rho) = \rho j_n(\rho)$$

$$\xi(\rho) = \rho h_n^{(1)}(\rho)$$

If we take both the permeability of the surrounding medium and of the particle to be the same, then

$$\begin{aligned} a_n &= \frac{m \psi_n(mx) \psi'_n(x) - \psi_n(x) \psi'_n(mx)}{m \psi(mx) \xi'_n(x) - \xi_n(x) \psi'_n(mx)} \\ b_n &= \frac{\psi_n(mx) \psi'_n(x) - m \psi_n(x) \psi'_n(mx)}{\psi_n(mx) \xi'_n(x) - m \xi_n(x) \psi'_n(mx)} \end{aligned} \quad (69)$$

Note that  $a_n$  and  $b_n$  vanish as  $m$  approaches unity, this is as it should be, when the particle dissapears, so does the scattered field. Finally, once obtained the scattering coefficients the scattering cross sections can be obtained as

$$\begin{aligned} C_{\text{sca}} &= \frac{W_{\text{sca}}}{I_{\text{inc}}} = \frac{2\pi}{k^2} \sum_{n=1}^{\infty} (2n+1) (|a_n|^2 + |b_n|^2) \\ C_{\text{ext}} &= \frac{W_{\text{ext}}}{I_{\text{inc}}} = \frac{2\pi}{k^2} \sum_{n=1}^{\infty} (2n+1) \Re(|a_n| + |b_n|) \end{aligned} \quad (70)$$

### 1.2.5 Particles small compared with the wavelength

From power series expansion of the spherical Bessel functions (48), and equations (68) and (69) we have

$$\begin{aligned}
\psi_1(\rho) &\approx \frac{\rho^2}{3} - \frac{\rho^4}{30}, & \psi'_1(\rho) &\approx \frac{2\rho}{3} - \frac{2\rho^3}{15}, \\
\xi_1(\rho) &\approx -\frac{i}{\rho} - \frac{i\rho}{2} + \frac{\rho^2}{3}, & \xi'_1(\rho) &\approx \frac{i}{\rho^2} - \frac{i}{2} + \frac{2\rho}{3} \\
\psi_2(\rho) &\approx \frac{\rho^2}{15}, & \psi'_2(\rho) &\approx \frac{\rho^2}{5} \\
\xi_2(\rho) &\approx -\frac{i^3}{\rho^2}, & \xi'_2(\rho) &\approx \frac{i^6}{\rho^3}
\end{aligned}$$

with the coefficients

$$\begin{aligned}
a_1(\rho) &= -\frac{i2x^3}{3} - \frac{m^2 - 1}{m^2 + 2} - \frac{i2x^5}{5} \frac{(m^2 - 2)(m^2 - 1)}{(m^2 + 2)^2} \\
&\quad + \frac{4x^6}{9} \left(\frac{m^2 - 1}{m^2 + 2}\right)^2 + O(x^7), \\
b_1 &= -\frac{ix^5}{45} (m^2 - 1) + O(x^7), \\
a_2 &= -\frac{ix^5}{15} \frac{m^2 - 1}{2m^2 + 3} + O(x^7), \\
b_2 &= O(x^7)
\end{aligned}$$

Here one condition arises, if  $|m|x \ll 1$ , then  $|b_1| \ll |a_1|$ ; with this assumption the amplitude scattering matrix elements to terms of order  $x^3$  are

$$\begin{aligned}
S_1 &= \frac{3}{2}a_1, \\
S_2 &= \frac{3}{2}a_1 \cos \theta, \\
a_1 &= -\frac{i2x^3}{3} \frac{m^2 - 1}{m^2 + 2}
\end{aligned} \tag{71}$$

where, if the incident light is unpolarized with radiance  $I_i$ , the scattered irradiance  $I_s$ , is

$$I_s = -\frac{8\pi^4 N a^6}{\lambda^4 r^2} \left| \frac{m^2 - 1}{m^2 + 2} \right|^2 (1 + \cos^2 \theta) I_i \tag{72}$$

where  $\theta$  is the angle between the incident and scattering beam. If the quantity  $|(m^2 - 1)/(m^2 + 2)|^2$  is weakly dependent on wavelength (this is not always true), the irradiance scattered by a sphere is small compared with the wavelength or, indeed, any sufficient small particle regardless of its shape, is proportional to  $1/\lambda^4$  [11]. Such scattering is called Rayleigh scattering which applies to incident unpolarized light.

Inside the scattering plane (see fig. 5) we can observe the relation between incident and scattered light, where the unitary vectors shows the direction of the scattered and incident components. One important light scattering parameter is the phase function  $F(\theta)$  which is proportional to the sum of the perpendicular and parallel polarized scattered light intensities  $F(\theta) \propto i_\perp + i_\parallel$ . The angular distribution of the scattered light depends on the polarization of the incident light.

$$i_{\parallel} = -\frac{9|a_1|^2}{4k^2r^2} \cos^2 \theta \quad \text{Incident light polarized parallel to the scattering plane.}$$

$$i_{\perp} = -\frac{9|a_1|^2}{4k^2r^2} \quad \text{Incident light polarized perpendicular to the scattering plane}$$

$$i = \frac{1}{2}(i_{\parallel} + i_{\perp}) \quad \text{Unpolarized incident light}$$

If the incident light is 100% polarized, the scattered light will be similarly polarized. However, because light of two different polarization states is scattered differently, the scattered light will be partially polarized if the incident light is unpolarized and

$$P = \frac{i_{\perp} - i_{\parallel}}{i_{\perp} + i_{\parallel}} = \frac{1 - \cos^2 \theta}{1 + \cos^2 \theta} \quad (73)$$

where the degree of polarization of the scattered light, given incident unpolarized light is  $|P|$ .  $P$  is always positive; therefore the scattered light is partially polarized *perpendicular* to the scattering plane. If a sufficiently small sphere is illuminated by unpolarized light, the scattered light is 100 % polarized at a scattering angle of 90%. We should note that the *absolute* scattered irradiance depends on size (the volume squared), but is difficult to measure absolute irradiances. Therefore, the radius of small spheres cannot readily be determined from scattering measurements; in this sense, all small spheres are equal [11].

### 1.2.6 The scattering matrix

Consider again an arbitrary particle that is illuminated by a plane harmonic wave (Fig. 5). The direction of propagation of the incident light defines the  $z$  axis which is called the *forward direction*. The scattering direction  $\hat{\mathbf{e}}_r$  and the forward direction  $\hat{\mathbf{e}}_z$  define a plane called the *scattering plane*. The incident electric field

$\mathbf{E}_i$ , which lies in the  $xy$  plane, can be expressed in components parallel ( $E_{\parallel}$ ) and perpendicular ( $E_{\perp}$ ) to the scattering plane

$$\mathbf{E}_i = (E_{0\parallel} \hat{\mathbf{e}}_{\parallel i} + E_{\perp} \hat{\mathbf{e}}_{\perp i}) e^{i(kz - \omega t)} = E_{\parallel i} \hat{\mathbf{e}}_{\parallel i} + E_{\perp i} \hat{\mathbf{e}}_{\perp i} \quad (74)$$

where the basis vectors hold the relations

$$\begin{aligned} \hat{\mathbf{e}}_{\perp i} &= \sin \phi \hat{\mathbf{e}}_x - \cos \phi \hat{\mathbf{e}}_y \\ \hat{\mathbf{e}}_{\parallel i} &= \cos \phi \hat{\mathbf{e}}_x + \sin \phi \hat{\mathbf{e}}_y \\ \hat{\mathbf{e}}_{\parallel i} &= \sin \theta \hat{\mathbf{e}}_r + \cos \theta \hat{\mathbf{e}}_{\theta} \\ \hat{\mathbf{e}}_{\perp i} \times \hat{\mathbf{e}}_{\parallel i} &= \hat{\mathbf{e}}_z \\ \hat{\mathbf{e}}_{\perp i} &= -\hat{\mathbf{e}}_{\phi} \end{aligned} \quad (75)$$

where  $k = 2\pi n/\lambda$  is the wave number in the medium surrounding the particle,  $n$  is the refractive index, and  $\lambda$  is the wavelength of the incident light in vacuo.

At sufficiently large distances from the origin ( $kr \gg 1$ ), in the *far-field region*, the scattered electric field  $\mathbf{E}_s$  is approximately transverse ( $\hat{\mathbf{e}}_r \cdot \mathbf{E}_s \approx 0$ ) and may be written

$$\mathbf{E}_s = E_{\parallel s} \hat{\mathbf{e}}_{\parallel s} + E_{\perp s} \hat{\mathbf{e}}_{\perp s} \quad (76)$$

similarly for the scattering field its basis vectors follow the relations

$$\begin{aligned} \hat{\mathbf{e}}_{\parallel s} &= \hat{\mathbf{e}}_{\theta} \\ \hat{\mathbf{e}}_{\perp s} &= -\hat{\mathbf{e}}_{\phi} \\ \hat{\mathbf{e}}_{\perp s} \times \hat{\mathbf{e}}_{\parallel s} &= \hat{\mathbf{e}}_r \end{aligned} \quad (77)$$

From fig.5, the basis vector  $\hat{\mathbf{e}}_{\parallel s}$  is parallel and  $\hat{\mathbf{e}}_{\perp s}$  is perpendicular to the

scattering plane, and the vectors  $\mathbf{E}_s$  and  $\mathbf{E}_i$  are specified relative to *different* sets of basis vectors. Because the linearity of the boundary conditions of the problem, the amplitude of the field scattered by an arbitrary particle is a linear function of the amplitude of the incident field. The relation between incident and scattered field is more conveniently written in matrix form

$$\begin{bmatrix} E_{\parallel s} \\ E_{\perp s} \end{bmatrix} = \frac{e^{i k (r-z)}}{-i k r} \begin{bmatrix} S_2 & S_3 \\ S_4 & S_1 \end{bmatrix} \begin{bmatrix} E_{\parallel i} \\ E_{\perp i} \end{bmatrix} \quad (78)$$

where the elements  $S_j (j = 1, 2, 3, 4)$  of the *amplitude scattering matrix* depend in general on  $\theta$ , the *scattering angle*, and the azimuthal angle  $\phi$ .

Once we have obtained the electromagnetic field inside and scattered by the particle, we can determine the Poynting vector and the electromagnetic fields at points outside the particle. The calculated electromagnetic fields allow the determination of the Poynting vector at points outside the particle (see figure 4). By using the equation (21), the Poynting vector  $\mathbf{S}$  at any point in the medium surrounding the particle can be written as the sum of three terms:

$$\begin{aligned} \mathbf{S} &= \frac{1}{2} \Re\{\mathbf{E}_2 \times \mathbf{H}_2^*\} = \mathbf{S}_{\text{inc}} + \mathbf{S}_{\text{sca}} + \mathbf{S}_{\text{ext}} \\ \mathbf{S}_{\text{inc}} &= \frac{1}{2} \Re\{\mathbf{E}_{\text{inc}} \times \mathbf{H}_{\text{inc}}^*\}, \quad \mathbf{S}_{\text{sca}} = \frac{1}{2} \Re\{\mathbf{E}_{\text{sca}} \times \mathbf{H}_{\text{sca}}^*\} \\ \mathbf{S}_{\text{ext}} &= \frac{1}{2} \Re\{\mathbf{E}_{\text{inc}} \times \mathbf{H}_{\text{sca}}^* + \mathbf{E}_{\text{sca}} \times \mathbf{H}_{\text{inc}}^*\} \end{aligned} \quad (79)$$

if the medium is nonabsorbent,  $\mathbf{S}_{\text{inc}}$  is independent of the position and we may interpret  $\mathbf{S}_{\text{ext}}$  as the term that arises because of the interaction between the incident and scattered waves. The problem of scattering is in this sense a problem

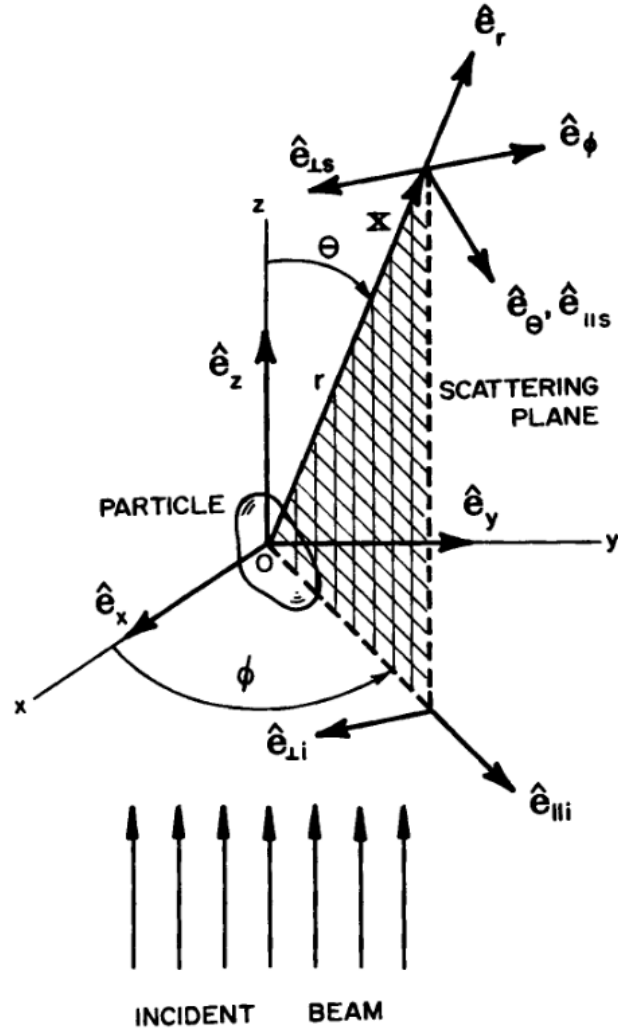


Figure 5: Scattering by an arbitrary particle. Courtesy of Bohren, C. F. and Huffman, D. R.[11].

that is more related to the polarization of light, which is nicely represented by a column vector called the *Stokes vector* [15], with its four elements which are called the Stokes parameter. The theory of light scattering and Stokes parameters was introduced into optics by Sir George Gabriel Stokes in 1852 when he was trying to describe mathematically the nature of polarized light, but his work was not followed immediately until almost one century after when it was "rediscovered" by S. Chandrasekar in the late 1940s when he wrote his monumental paper on radiative transfer [16]. If  $\mathbf{E} = \mathbf{E}_0 \exp(ikz - i\omega t)$  represent the incident wave with  $\mathbf{E}_0 = E_{||}\hat{\mathbf{e}}_{||} + E_{\perp}\hat{\mathbf{e}}_{\perp}$ , the Stokes polarization parameters of the incident light are written as

$$\begin{aligned}
I_{\text{inc}} &= E_{||\text{inc}}E_{||\text{inc}}^* + E_{\perp\text{inc}}E_{\perp\text{inc}}^* \\
Q_{\text{inc}} &= E_{||\text{inc}}E_{||\text{inc}}^* - E_{\perp\text{inc}}E_{\perp\text{inc}}^* \\
U_{\text{inc}} &= E_{||\text{inc}}E_{\perp\text{inc}}^* + E_{\perp\text{inc}}E_{||\text{inc}}^* \\
V_{\text{inc}} &= i(E_{||\text{inc}}E_{\perp\text{inc}}^* - E_{\perp\text{inc}}E_{||\text{inc}}^*)
\end{aligned} \tag{80}$$

The Stokes parameters of the light scattered by a particle are represented by

$$\begin{aligned}
I_{\text{sca}} &= \frac{k}{2\omega\mu} (E_{||\text{sca}}E_{||\text{sca}}^* + E_{\perp\text{sca}}E_{\perp\text{sca}}^*) \\
Q_{\text{sca}} &= \frac{k}{2\omega\mu} (E_{||\text{sca}}E_{||\text{sca}}^* - E_{\perp\text{sca}}E_{\perp\text{sca}}^*) \\
U_{\text{sca}} &= \frac{k}{2\omega\mu} (E_{||\text{sca}}E_{\perp\text{sca}}^* + E_{\perp\text{sca}}E_{||\text{sca}}^*) \\
V_{\text{sca}} &= i\frac{k}{2\omega\mu} (E_{||\text{sca}}E_{\perp\text{sca}}^* - E_{\perp\text{sca}}E_{||\text{sca}}^*)
\end{aligned} \tag{81}$$

The parameters in equations (80) and (81) represent the total intensity of the light ( $I_{\text{sca}}$ ), the amount of linear horizontal or vertical polarization ( $Q_{\text{sca}}$ ), the amount of  $45^\circ$  or  $-45^\circ$  degrees polarization ( $U_{\text{sca}}$ ), and the amount of right or left

circular polarization ( $V_{\text{sca}}$ ) for scattered light (incident or scattered). The relation between incident and scattered Stokes parameters are

$$\begin{aligned}
\begin{bmatrix} I_{\text{sca}} \\ Q_{\text{sca}} \\ U_{\text{sca}} \\ V_{\text{sca}} \end{bmatrix} &= \frac{1}{k^2 r^2} \begin{bmatrix} S_{11} & S_{12} & S_{13} & S_{14} \\ S_{21} & S_{22} & S_{23} & S_{24} \\ S_{31} & S_{32} & S_{33} & S_{34} \\ S_{41} & S_{42} & S_{43} & S_{44} \end{bmatrix} \begin{bmatrix} I_{\text{inc}} \\ Q_{\text{inc}} \\ U_{\text{inc}} \\ V_{\text{inc}} \end{bmatrix} \\
S_{11} &= \frac{1}{2} (|S_1|^2 + |S_2|^2 + |S_3|^2 + |S_4|^2) \\
S_{12} &= \frac{1}{2} (|S_2|^2 - |S_1|^2 + |S_4|^2 - |S_3|^2) \\
S_{13} &= \Re(S_2 S_3^* + S_1 S_4^*) \\
S_{14} &= \Im(S_2 S_3^* - S_1 S_4^*) \\
S_{21} &= \frac{1}{2} (|S_2|^2 - |S_1|^2 - |S_4|^2 + |S_3|^2) \\
S_{22} &= \frac{1}{2} (|S_2|^2 + |S_1|^2 - |S_4|^2 - |S_3|^2) \\
S_{23} &= \Re(S_2 S_3^* - S_1 S_4^*) \\
S_{24} &= \Im(S_2 S_3^* + S_1 S_4^*) \\
S_{31} &= \Re(S_2 S_4^* + S_1 S_3^*) \\
S_{32} &= \Re(S_2 S_4^* - S_1 S_3^*) \\
S_{33} &= \Re(S_1 S_2^* + S_3 S_4^*) \\
S_{34} &= \Im(S_2 S_1^* + S_4 S_3^*) \\
S_{41} &= \Im(S_2^* S_4 + S_3^* S_1) \\
S_{42} &= \Im(S_2^* S_4 - S_3^* S_1) \\
S_{43} &= \Im(S_1 S_2^* - S_3 S_4^*) \\
S_{44} &= \Re(S_1 S_2^* - S_3 S_4^*)
\end{aligned} \tag{82}$$

where this  $4 \times 4$  matrix is the *scattering matrix* or the *Müller matrix* and it de-

scribes the relation between "incident and "transmitted" Stokes vectors.

The Stokes parameters of the light scattered by a collection of particles are the sum of the Stokes parameters of the light scattered by individual particles. Therefore the scattering matrix for such a collection is merely the sum of individual particle scattering matrices, assuming that the linear dimensions of the volume occupied by the scatterers is small compared with the distance  $r$  at which the scattered light is observed [11].

### 1.3 The T-matrix approximation

The T-matrix method is a powerful technique for computing light scattering by nonspherical single and compounded particles in random orientation and it is based on numerically solving Maxwell's equations [5]. It was first introduced by Waterman (1965, 1971) as a technique for computing electromagnetic scattering by single, homogeneous, arbitrarily shaped particles based on the Huygens principle ([17], [18], [19], and [20]). due to the linearity of the Maxwell's equations, it is possible to expand both the incident and scattered waves into spherical harmonics and then relate the scattering coefficients of those expansions through use of a transformation matrix [5].

The single scattering of light by a small-volume element  $dV$  of  $n$  particles randomly oriented, and rotationally symmetric, is completely described by the ensembled-averaged extinction,  $C_{\text{ext}}$ , and scattering  $C_{\text{sca}}$ , cross sections per particle and the dimensionless Müller scattering matrix from equation (82). The process of the scattering is depicted by the following equation:

$$I_{\text{sca}} = \frac{n C_{\text{sca}} dV}{4\pi R^2} F(\theta) I_{\text{inc}} \quad (83)$$

where  $F(\theta)$  is the scattering matrix,  $\theta$  is angle between the incident and scattered

beam,  $R$  is the distance between the scattering system and the detector,  $C_{\text{sca}}$  is the scattering cross section of the particle, and  $F(\theta)$  is the Müller matrix.

The T-matrix model calculates, both scattering and extinction cross sections  $C_{\text{sca}}$  and  $C_{\text{ext}}$ , respectively, single scattering albedo, asymmetry parameter, and the Stokes and Müller matrix.

The formulation as it is presented by Mishchenko [5] consider an arbitrarily shaped particle located at the origin of a spherical coordinate system with a plane wave incident on the particle. The incident fields  $E_i$  and  $E_s$  are expanded as a series of spherical harmonics:

$$\mathbf{E}_i = \sum_n^\infty \sum_{m=-n}^n [a_{mn} Rg \mathbf{M}_{mn}(kr) + b_{mn} Rg \mathbf{N}_{mn}(kr)] \quad (84)$$

$$\mathbf{E}_s = \sum_n^\infty \sum_{m=-n}^n [p_{mn} \mathbf{M}_{mn}(kr) + q_{mn} \mathbf{N}_{mn}(kr)] \quad (85)$$

where  $M_{mn}$  and  $N_{mn}$  are proportional to the spherical Hankel functions, and  $Rg$  denotes the regular solution of the Helmholtz equation for the scattering problem (see Mishchenko, appendix C [5]).

For practical computer calculations, the infinite series are truncated to a finite size  $n_{\text{max}}$  that depends on the size parameter  $x = k_1 r$ , where  $r$  is the particle radius and  $k_1$  is the wave vector of the medium. This chosen value is adopted in the code as

$$n_{\text{max}}(x) = x + 4.05x^{\frac{1}{3}} + 8 \quad (86)$$

The relation of incident coefficients  $a_{mn}$  and  $b_{mn}$ , to the scattered field coefficients,

$p_{mn}$ , and  $q_{mn}$  are

$$p_{mn} = \sum_{n'=1}^{\infty} \sum_{m'=-n'}^{n'} [T_{mnm'n'}^{11} a_{m'n'} + T_{mnm'n'}^{12} b_{m'n'}] \quad (87)$$

$$q_{mn} = \sum_{n'=1}^{\infty} \sum_{m'=-n'}^{n'} [T_{mnm'n'}^{21} a_{m'n'} + T_{mnm'n'}^{22} b_{m'n'}] \quad (88)$$

or in matrix form

$$\begin{bmatrix} p \\ q \end{bmatrix} = \begin{bmatrix} T^{11} & T^{12} \\ T^{21} & T^{22} \end{bmatrix} \begin{bmatrix} a \\ b \end{bmatrix} \quad (89)$$

where  $T$  is the transformation matrix or *T-matrix* and it does not depend on the incident or scattered fields, but only on the physical properties of the scattering particle. Once the transformation matrix is solved for a given particle, it is possible to calculate the scattered light for any orientation of incident radiation. The determination of the *T-matrix* can be accomplished by use of the extended boundary condition method [17]. This is done by first expanding the internal field  $E_{\text{int}}$  of the particle in terms of vector spherical functions as it was explained on sections 1.2.3 and 1.2.4 for spherical particles. Following the same analysis, it is found that the internal field  $E_{\text{int}}$  is

$$E_{\text{int}} = \sum_n^{\infty} \sum_{m=-n}^n [c_{mn} Rg M_{mn}(mkr) + d_{mn} Rg N_{mn}(mkr)] \quad (90)$$

where the complex index of refraction is given by  $m$ . The expansion coefficients of the internal field to those of the incident and scattered fields through the

transformation matrix  $Q$  are

$$\begin{bmatrix} a \\ b \end{bmatrix} = \begin{bmatrix} Q^{11} & Q^{12} \\ Q^{21} & Q^{22} \end{bmatrix} \begin{bmatrix} c \\ d \end{bmatrix} \quad (91)$$

$$\begin{bmatrix} p \\ q \end{bmatrix} = - \begin{bmatrix} Rg Q^{11} & Rg Q^{12} \\ Rg Q^{21} & Rg Q^{22} \end{bmatrix} \begin{bmatrix} c \\ d \end{bmatrix} \quad (92)$$

The  $T$ -matrix can then be related to  $Q$  by the following

$$T = -Rg Q Q^{-1} \quad (93)$$

The elements of  $Q$  are integrals over the particle's surface and depend again on the physical properties of that particle. In eneral,  $T$  and  $Q$  contain an infinite number of elements. However, for practical purposes, the summations on equations (85) and (90), are truncated after certain convergence criteria are reached thus allowing  $T$  to be determined explicitly. In addition, the calculation of  $T$  can be greatly simplified by the assumption of an ensemble of randomly oriented particles with rotational symmetry.

The T-matrix calculations of light scattering was done using the double precision T-matrix code for polydisperse non-spherical and randomly oriented particles of Mishchenko et al., available at NASA web site <http://www.giss.nasa.gov/staff/mmishchenko/> and of free distribution.

### 1.3.1 The T-matrix approximation for coated non-spherical particles

The calculation of light scattering properties of randomly oriented symmetric coated particles, for concentric spheres was studied with the Aden-Kerker theory

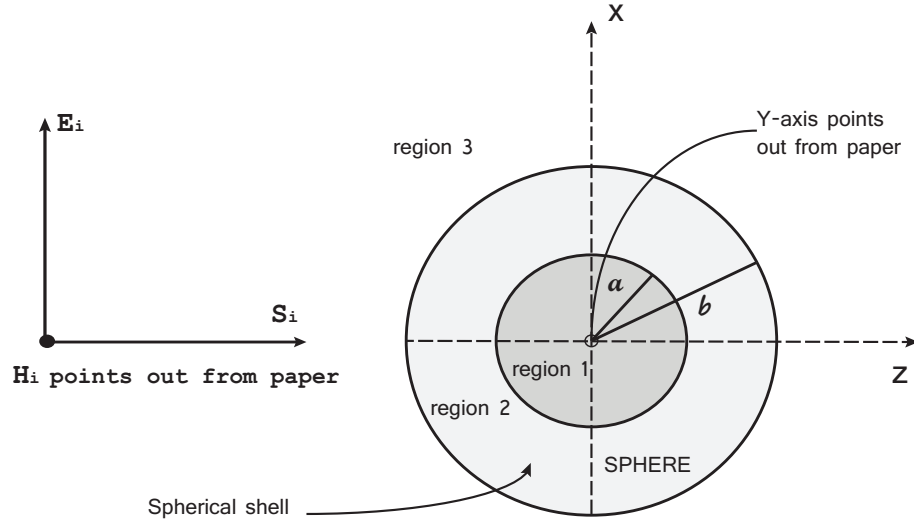


Figure 6: The geometry of a plane wave incident upon a sphere with a concentric spherical shell, as it was shown by Aden and Kerker [21].

[21] in the framework of the T-matrix approximation. The problem is described in fig. 6 with the incident Poynting vector  $\mathbf{S}_i$  represented as the vector perpendicular to the magnetic and electric field. This figure is a representation of a simplified geometry of the problem for spherical coated particle of inner radius  $a$ , outer radius  $b$  is illuminated by a monochromatic beam of radiation of vacuum wavelength  $\lambda_0$ , and  $n_0$ ,  $n_1$ ,  $n_2$  are the refractive indices of the suspending medium (air in this case), core, and shell respectively,  $k = 2\pi/\lambda = 2\pi n_1/\lambda_0$  and  $x = ka$ ,  $y = kb$  are the dimensionless sizes parameters and the dimensionless parameter  $q = x/y$  is used to reduce the number of parameters needed to describe the size distribution for the entire particle [22].

As it was seen in section 1.3, the T-matrix elements only depend on the particle's size, shape, composition and orientation and they can be calculated in the natural reference frame ( $z$  axis along the revolution axis) and then be averaged for all incident and scattering directions, which equals averaging on particle orientation [23]. In this case, the T-matrix can be written in compact

notation as

$$T = -B \cdot A^{-1} = - \begin{bmatrix} B_{11} & B_{12} \\ B_{21} & B_{22} \end{bmatrix} \cdot \begin{bmatrix} A_{11} & A_{12} \\ A_{21} & A_{22} \end{bmatrix}^{-1} = \begin{bmatrix} T_{11} & T_{12} \\ T_{21} & T_{22} \end{bmatrix} \quad (94)$$

as it is written and solved in [5], and [24]. In the case of homogeneous scatterer, the matrices depend on the inner and outer indices of refraction  $m_1$  (core) and  $m_2$  (shell), the T-matrix can be calculated as [25].

$$T = -B \cdot A^{-1} = - \left[ B_2 + BB_2 \cdot (-B_1 \cdot A_1^{-1}) \right] \cdot \left[ A_2 + AA_2 \cdot (-B_1 \cdot A_1^{-1}) \right] \quad (95)$$

with

- $-B_1 \cdot A^{-1} = T_1$  is the T-matrix for the core particle with refractive index as  $m_1/m_2$  for inner, as 1 for outer and incident radiation wave number as  $k_0 m_2$ .
- $A_2$  and  $B_2$  are calculated by setting refractive index as  $m_2$  for inner and as 1 for outer, and an incident wavelength as  $k_0$ . If calculated, the product  $-B_2 \cdot A_2^{-1}$  would be the T-matrix for a particle with no core.
- Matrices  $AA_2$  and  $BB_2$  are calculated in the same way as  $A_2$ ,  $B_2$  except that the Bessel functions of the first kind with argument  $kr$  are replaced by Hankel functions with the same argument [22].

## CHAPTER 2

### Methodology

#### 2.1 Instrumentation

In order to have an accurate description of the particles during the day, the Atmospheric Physics Laboratory acquired a laser particle counter model Climet CI150, which provides number distributions in four defined channels, and a Photoacoustic Extinctionmeter, which provides scattering values, absorption and extinction coefficients, and detects soot at 870 nm. These instruments along with a visible multifilter radiometer will be described in the next subsections as well as the mathematical model used to calculate the cross sections of the particles.

##### 2.1.1 Optical particle laser counter

An optical particle counter uses a high-intensity light source (a laser), a controlled air flow (viewing volume), and a highly sensitive light photodetector [26]. The instrument measures the scattering of the light produced by the interaction of the laser with the air sample. The light scattered is converted to electric signals or electric pulses which are proportional to the pulses of scattered light which at the same time is proportional to the size of the particle. The next step procedure is to analyze the height of the electric signals. It is achieved by a pulse height analyzer which examines the magnitude of the electrical pulses and places the values into an appropriate sizing channel. The channels contain information about each pulse that correlates to particle sizes.

The laser particle counter instrument used in this work is the Climet CI-150t (Climet instrument 150t) which is a laser diode based aerosol particle counter that monitors particles in four ranges or bins: 0.3-0.5, 0.5-1.0, 1.0-5.0, and  $\geq 5.0\mu\text{m}$ . It is fully self-contained, operating on battery power or AC power for sampling



Figure 7: Climet CI-150t - Laser Particle Counter.

convenience [27]. It works by taking samples at flow rates of air at one cubic foot per minute (1 CFM). The sample air is filtered before being exhausted through the rear panel. Counts of the types of particles are displayed and printed in a variety of formats. They can be stored on an 3.5" floppy disk or in the computer through a RS-232 serial port. Data are displayed as a comma delimited ASCII which contains the total count, differential count, concentration per cubic foot, and concentration per cubic meter. The instrument uses a highly efficient optical system and detection electronics based on a light scattering principle. The light from a 50 mW laser diode is scattered by the particles and then collected by an elliptical mirror and focused onto a solid state photo detector, which converts the light energy into electrical current. Figure 7 displays a picture of the instrument.

### 2.1.2 Photoacoustic Extinctionmeter (PAX)

The Photoacoustic Extinctionmeter (PAX) is a sensitive, high-resolution, fast-response instrument for measuring aerosol optical properties relevant for climate change and carbon particle sensing [28]. Its applications are to air quality and

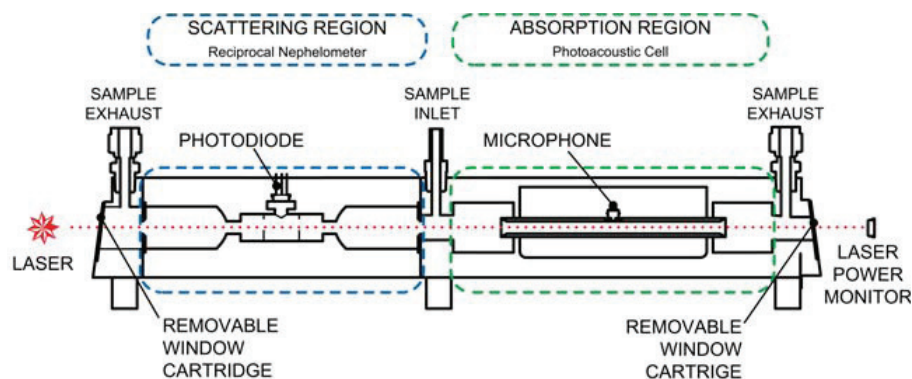


Figure 8: Photoacoustic extinctionimeter circuit diagram.



Figure 9: Photoacoustic extinctionimeter model PAX 870 nm.

visibility, atmosphere, health effects, combustion source emissions and biomass burning.

Figure 8 depicts the internal mechanism of the instrument. It uses a modulated diode laser to simultaneously measure light scattering and absorption. The Atmospheric Physics Laboratory at the University of Texas at El Paso acquired the standard 870 nm wavelength which is especially sensitive to black carbon particles, since there is relatively little absorption from gases and non-BC aerosol species at this wavelength. Figure 8 shows the mechanism of measurement through the circuit diagram and figure 9 shows a frontal view of the instrument in operational mode. The "modus operandi" is as follow: a 1 liter per minute aerosol sample flow

is drawn into the PAX using an internal vacuum pump controlled by two critical orifices, the inlet and exhaust orifices. The flow is split between the nephelometer and photoacoustic resonator for simultaneous measurement of light scattering and absorption. The absorption measurement uses in-situ photoacoustic technology. A laser beam directed through the aerosol stream is modulated at the resonant frequency of the acoustic chamber. Absorbing particles heat up and quickly transfer heat to the surrounding air. The periodic heating produces pressure waves that can be detected with a sensitive microphone and determine aerosol light absorption. Additionally, the PAX uses a wide-angle integrating reciprocal nephelometer to measure the light scattering coefficient. The scattering measurement responds to all particle types regardless of chemical makeup, mixing state, or morphology. The measurements are recorded every 15 seconds and stored internally. The data is then copied to an usb device as comma separated values format or CSV.

### **2.1.3 The Visible Multifilter Rotating Shadowband Radiometer**

The Visible Multifilter Rotating Shadowband Radiometer (Vis-MFRSR) instrument consist of a broadband channel together with a rotating shadowband which measures solar irradiance at six narrowband wavelengths (nominal 415, 500, 615, 673, 870, and 940 nm) and instantaneous optical depth. This measurements are made every 15 seconds and integrated into 3-minute averages and stored by an on-board computer.

The University of Texas at El Paso, Texas, was integrated as one of the monitoring sites once it installed the Vis-MFRSR on January 6, 2006 on the roof of the Undergraduate Learning Center (UGLC) of the University of Texas at El Paso (UTEP) and started to collect data since then (See figure 10).



Figure 10: Side (a) and close up view (b) of the Visible Multifilter Rotating Shadowband Radiometer installed at the roof of the Undergraduate Learning center (UGLC), at the University of Texas at El Paso.

## 2.2 Mathematical models

The T-matrix theory is applied for the nonspherical, polydispersal and randomly oriented aerosol particles for both core alone and core-shell geometry where mineral dust and black carbon were selected as the main constituents of the particles. In the El Paso del Norte Airshed most of the particles are scatterers as it is seen in the retrieval of single scattering albedo from radiative transfer models applied to the region. The truncation of the series expansion of the fields was taking according to eq. (86), and the models used here were running in a PC with AMD FX-8350 8-Core processor under LINUX environment and GNU compilers.

### 2.2.1 The Tropospheric Radiative Transfer Model (TUV)

The TUV model version 5.0 is a one-dimensional radiative transfer code that uses either or both of Eddington's approximations and the discrete ordinate method to describe the radiative transfer through the atmosphere. The code gives outputs of various spectral irradiances in the UV and visible spectra by using input data, such as geographic coordinates and atmospheric parameters in standard format. The Tropospheric Radiative Transfer Model, TUV, has been used to solve

the Radiative Transfer Equation and obtain single scattering values as it will be explained later.

### 2.2.2 The T-matrix model

As it was indicated in section 1.3, the T-matrix model is a mathematical model tool which was built following the T-matrix approximation given by Waterman [17], and that accurately computes light scattering by nonspherical particles. The description of the input values of the code is done by Mishchenko [29]. In this work, the T-matrix version for randomly oriented nonspherical particles in double precision was modified and applied using the variables from table 2. The code was modified in order to obtain  $C_{\text{ext}}$  and  $C_{\text{sca}}$  values at the effective radius for the four bins of the laser particle counter at different wavelengths and different refractive indexes from days selected at the El Paso del Norte Airshed. The required input to the code include the wavelength of the incident light. In this case, because of the capabilities of the acoustic extinctionmeter, the wavelength selected was  $0.87\mu\text{m}$ . The size distribution was input as lognormal distribution parameters based on fit data. Particle shape were input as oblate spheroids (ellipse of revolution about its minor axis) with sphericity parameter (EPS) equals to 1.5. This spheroidal approximation of particle shape applied for Mineral Dust and Black Carbon is based on early works (see for example Nousiainen and Vermeulen [30]). Although this is not true in reality (atmospheric particles are highly irregular in shape) this shape model showed good results and save us greatly time computations. The spheroids are formed by rotating an ellipse about its minor axis (oblate spheroid) or major axis (prolate spheroid). Their shape are described by the equation

$$r(\vartheta) = a \left( \sin^2 \vartheta + \frac{a^2}{b^2} \cos^2 \vartheta \right)^{-\frac{1}{2}} \quad (96)$$

where  $b$  is the rotational (vertical) semi-axis and  $a$  is the horizontal semi-axis, and the shape and size of the spheroid is specified by the axis ratio  $a/b$  and by either  $r_s$  which is the radius of a sphere having the same area or  $r_v$  which is the radius of a sphere having the same volume. The following definitions are summarized in the input table 2 and allowed us to understand the model in general (see Mishchenko [5]). The average area of the geometric projection per particle  $\langle G \rangle$

$$\langle G \rangle = \int_{r_{\min}}^{r_{\max}} dr n(r) \pi r^2 \quad (97)$$

where  $\langle G \rangle = \pi r^2$  if it is the area of circle.

The average volume per particle  $\langle V \rangle$

$$\langle V \rangle = \int_{r_{\min}}^{r_{\max}} dr n(r) \frac{4}{3} \pi r^3 \quad (98)$$

and the average radius  $\langle R \rangle$

$$\langle R \rangle = \int_{r_{\min}}^{r_{\max}} dr n(r) r \quad (99)$$

where  $n(r)$  is the number distribution of the particles (particles/cm<sup>3</sup>), and  $r$  is the radius of the particle.

As it was indicated before, all input parameters must be specified in the same units. If the units we are working on are based on lengths like micrometers ( $1\mu\text{m} = 10^{-6}\text{m}$ ), then all the derivatives of length like area and volume must be expressed in micrometers. Table 3 describes output values from the code.

The model was modified to output the scattering, extinction and absorption

Table 2: T-matrix input parameter values

Input	Value	Description
R1 and R2	$R_i$	Array of 4 radii bins
ICHOICE	2	Gauss Elimination for inverse matrices
NDISTR	2	Lognormal distribution
DDELT	0.001	Accuracy
GAM	0.05	Not taken into account
NDGS	2	Compact spheres
NPNA	19	Number of scattering angles
NKMAX	5	Number $N_r$ of Gaussian quadrature points
LAM	0.87	Wavelength, it varies from 0.3-0.94 $\mu\text{m}$
EPS	1.5	Oblate spheroidal particles
RAT	1.0	Volume equivalent sphere radius $r_s$
NP	-1	Spheroids

cross sections per bin of the particle laser counter for the generalized spherical functions which are related with the solution of the scattering problem for the wave equations (35a) and (35b), however only the values of scattering and extinction cross sections were calculated from the model and for the computation of the optical coefficients and Müeller coefficients. The values of  $B_{\text{abs}}$  are generated by subtracting  $B_{\text{ext}} - B_{\text{sca}}$ .

Table 3: T-matrix output information

Output	Description
R1 and R2	Minimum and maximal radii, respectively
REFF	Effective radius
VEFF	Effective variance
CEXT	Ensemble-averaged extinction cross section per particle
CSCA	Ensemble-averaged scattering cross section per particle
COS	Ensemble-averaged asymmetry parameter
ALBEDO	Ensemble-averaged single scattering albedo
$\langle G \rangle$	Averaged projected area
$\langle V \rangle$	Averaged volume per particle
$\langle R \rangle$	Averaged radius

### 2.2.3 The LISA model

The T-matrix code was adapted to calculate first the  $(A_1, B_1)$  matrices for the inner layer, and then the  $(A_2, B_2, AA_2, BB_2)$  matrices for the outer layer as it is described in section 1.3.1 and by Quirantes [22]. Once computed, the T-matrix elements can be used to calculate any light scattering of interest, either cross sections or scattering (Müeller) matrix elements. As it was described for the T-matrix, tables 4 and 5 show input and output descriptions respectively.

Table 4: LISA input parameter values

Input	Value	Description
$mr_1$ and $mr_2$	Vary	Absolute refractive index for core and shell
ntope	7	Total angles in the calculation of the Müeller matrix
ang(ntope)	0:30:180	Angles in the calculation of the scattering matrix elements
$a$	2	Starting value of $n_{\max}(x + 4x^{1/2} + 2 - a)$
G	5	Number of Gaussian quadrature points $N_g = G \cdot n_{\max}$
kr, deri	0.001	Functions describing the particle surface, $r(\theta)$ , $dr/dr(\theta)$
$\Delta$	0.001	Desired accuracy
$r_{\text{int}}/r_{\text{ext}}$	Vary	Outer size over inner size ratio
NDISTR	2	Lognormal distribution
LAM	0.87	LAM varies from 0.3-0.94 $\mu\text{m}$
EPS	1.5	For sphere particles $a/b=1.00$
RAT	1.0	Volume equivalent sphere radius $r_s$
NP	-1	For spheroids

Table 5: LISA output information

Output	Description
$Q_{\text{sca}}$	scattering efficiencies
$Q_{\text{abs}}$	absorption efficiencies
$Q_{\text{ext}}$	extinction efficiencies
$F_{11}(\theta)$ and $F_{22}(\theta)$	Müeller elements
$F_{33}(\theta)$ and $F_{44}(\theta)$	Müeller elements
$F_{12}(\theta)$ and $F_{34}(\theta)$	Müeller elements

### 2.3 The Scattering Matrix

The description of the scattering effect of a beam by a volume is done by the Müller matrix or scattering matrix. The incident and scattered radiation are related by equation (83). When the scattering system is composed of randomly oriented, axially symmetric particles in single scattering, the scattering matrix has the form [11].

$$F(\theta) = \begin{bmatrix} F_{11}(\theta) & F_{12}(\theta) & 0 & 0 \\ F_{12}(\theta) & F_{22}(\theta) & 0 & 0 \\ 0 & 0 & F_{33}(\theta) & F_{34}(\theta) \\ 0 & 0 & -F_{34}(\theta) & F_{44}(\theta) \end{bmatrix} \quad (100)$$

where the Müller matrix elements are calculated from the expansion of generalized spherical functions  $P_{mn}^s(\theta)$

$$\begin{aligned} F_{11}(\theta) &= \sum_{s=0}^{\infty} a_1^s P_{00}^s(\cos \theta), \\ F_{22}(\theta) + F_{33}(\theta) &= \sum_{s=2}^{\infty} (a_2^s + a_3^s) P_{22}^s(\cos \theta), \\ F_{22}(\theta) - F_{33}(\theta) &= \sum_{s=2}^{\infty} (a_2^s - a_3^s) P_{22}^s(\cos \theta), \\ F_{44}(\theta) &= \sum_{s=0}^{\infty} a_4^s P_{00}^s(\cos \theta), \\ F_{12}(\theta) &= \sum_{s=2}^{\infty} b_1^s P_{02}^s(\cos \theta), \\ F_{34}(\theta) &= \sum_{s=2}^{\infty} b_2^s P_{02}^s(\cos \theta) \end{aligned} \quad (101)$$

where the  $a_i^s$ ,  $b_i^s$  are related to the T-matrix elements (see [22] and [23]).

#### 2.3.1 The matrix element $F_{11}$

Nonspherical particles are not always best scatterers than the spherical ones in the backscattering direction, and for this element the angular scattering are

similar for both prolate and oblate particles with the same long-to-short axis [23]. Also, the tendency of  $F_{11}$  is to increase with  $q = r_{\text{int}}/r_{\text{ext}}$  and scattering angle  $\theta$  in smoother behavior for nonspherical than for spherical particles.

### 2.3.2 The matrix element $F_{22}/F_{11}$

This Müller matrix element indicates nonsphericity, since it equals to unity for spherical particles, although non spherical particles can exhibit values close to one [31], and allows to distinguish prolate particles from oblate particles of the same volume and axial ratio.

### 2.3.3 The matrix element $F_{33}/F_{11}$ and $F_{44}/F_{11}$

These elements show sphericity if  $F_{33} = F_{44}$ . One characteristic of the  $F_{33}$  element is the faster variation for spherical particles than for nonspherical particles when the angle or the core size is changed [23]. For spheroids the differences between  $F_{33}$  and  $F_{44}$  are smaller also but not equal like as spheres. Also, in the backscattering region,  $F_{33}/F_{11} = F_{44}/F_{11} = -1$  for spheres at  $180^\circ$ . This fact is of relevance for particle sizing because backscattering is more sensitive to particle shape.

### 2.3.4 The matrix element $F_{12}/F_{11}$

This element indicates linear polarization. Its formulation is with in some references with negative sign (see for example Bohren [11]) and shows faster variations with core and angle for spherical particles. For particles smaller than the incident wavelength, the beam is complete polarized at  $90^\circ$  indicating Rayleigh effect (see eq. 72). It is also known that for non spherical particles polarization does not reach extremes ( $\pm 1$ ) [23].

### 2.3.5 The matrix element $F_{34}/F_{11}$

This parameter is more strongly core and angle dependent for spheres than for spheroids. When particles are nonspherical, this ratio does not reach extreme values ( $\pm 1$ ). In the forward and backward scattering regions, this ratio is close to zero, being identically zero for  $\theta = 0^\circ, 180^\circ$ , as it is predicted by theory [23].

## 2.4 Experimental setup

The procedure for modeling the inputs for the two mathematical models is represented in figure 11. Climet particle counter data for April 13, 2013 and July 18, 2014 were assumed to follow the lognormal distribution and they represent low relative humidity and high relative humidity day cases respectively. Parameters like the  $\ln^2 \sigma_g$  was calculated as input for the models, according to eq. (13). This distribution data were selected along with PAX acoustic extinctions values of  $B_{\text{sca}}$ ,  $B_{\text{abs}}$ , and  $B_{\text{ext}}$ , and compared to the computed coefficient values from the models. The T-matrix represent the model for low relative humidity and the LISA model is applied to the cases when relative humidity is considered. Comparisons of the coefficients  $B_{\text{sca}}$ ,  $B_{\text{abs}}$ , and  $B_{\text{ext}}$  were made for the two scattering models in order to validate them with the extinctions in the El Paso del Norte Airshed. Also, the Müller parameters from the scattering matrix (see section 2.3) were analyzed for the coating particles.

### 2.4.1 Selection of days

Values of the mean relative humidities (RH) were selected during April and October of 2013, and July 2014 due to the availability of the data from both the extinctions and the particle counter instruments. Two days which represent the minimum and maximum relative humidities were chosen and they are shown in tables 6, 7, and 8. Values of particle concentrations for these days are shown in

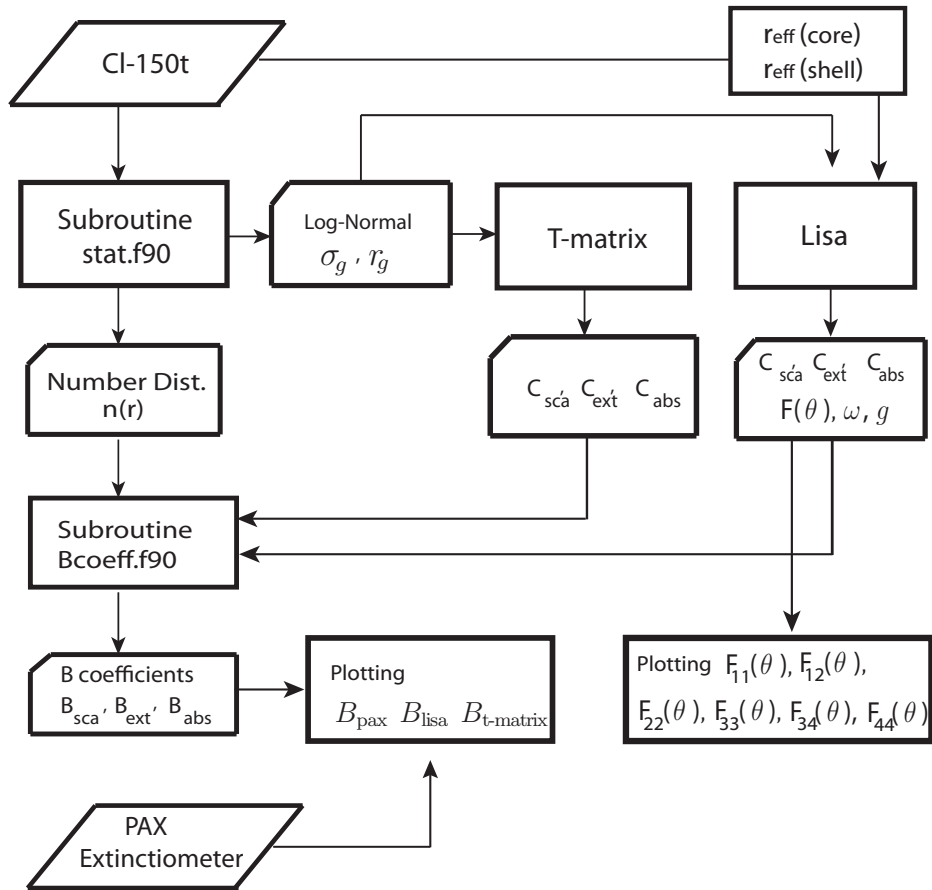


Figure 11: Flowchart of procedure for light scattering calculations.

figures 12 and 13 for the four bins  $0.3\text{-}0.5\ \mu\text{m}$ ,  $0.5\text{-}1.0\ \mu\text{m}$ ,  $1.0\text{-}5.0\ \mu\text{m}$ , and  $>5.0\ \mu\text{m}$  in diameter. The values from PM<sub>2.5</sub> and PM<sub>10</sub> were obtained from the Texas Commission on Environmental Quality (TCEQ) and gives us an idea about the mass concentration of particulate matter in the airshed, as can be seen in figures 14 and 15.

Once the days were selected, it was necessary to create input files for both models in the appropriate units required. Also, the refractive indices were calculated for the composite material which is mainly formed by mineral dust and soot. The volume-weighted averaged method was used to find the mass fraction of the species of the composite material and from there it was derived the refractive index of the composite medium in the air. By expanding the volume-weighted equation (17) and comparing their respective real and complex indices to the one calculated with the T-matrix and LISA codes, we were able to find the mass fractions and refractive indexes for both low-relative-humidity and high-relative-humidity days.

Table 6: Number concentration for April 13, 2013, in  $\text{cm}^{-3}$ , diameters for the four bins are in  $\mu\text{m}$  at the header

Time	0.3-0.5	0.5-1.0	1.0-5.0	>5.0
06:19	9.9600	1.7429	0.9794	0.0348
06:34	13.1535	2.3368	2.0626	0.1640
06:49	10.8528	1.9208	1.1806	0.0485
07:04	12.7955	2.0370	1.3215	0.0499
07:19	25.9999	3.5786	2.7547	0.1432
07:34	12.1289	2.5240	1.7888	0.0797
07:49	10.6261	1.6481	1.1271	0.0523
08:04	21.0171	15.4542	23.1116	1.8225
08:19	21.1408	14.0825	19.6178	1.5721
08:34	14.1236	2.8587	2.2292	0.1157
08:49	14.9980	3.4686	2.7531	0.1294
09:04	14.7230	3.3524	1.9758	0.0661
09:19	14.6298	2.6365	1.6233	0.0669
09:34	15.1510	2.7675	1.9617	0.1116
09:49	14.7666	2.5282	1.6758	0.0808
10:04	11.8997	2.1293	1.3801	0.0605
10:19	10.5391	1.9953	1.5563	0.0735
10:34	10.9753	1.8504	1.3306	0.0596
10:49	10.7518	1.9872	1.2841	0.0464
11:04	8.3661	1.3442	0.9078	0.0369
11:19	7.9078	1.1976	0.8429	0.0468
11:34	6.3282	1.0162	0.5573	0.0137
11:49	6.4654	1.1456	1.2269	0.0856
12:04	8.3632	1.2185	0.9092	0.0472
12:19	6.7148	1.0341	0.9951	0.0675
12:34	6.4278	0.9977	0.6779	0.0281
12:49	6.8004	1.1652	1.2468	0.0821
13:04	5.9705	0.8871	0.6543	0.0299
13:19	7.7794	1.0403	0.8873	0.0678
13:34	6.8964	0.9218	0.6661	0.0316
13:49	6.8087	0.9861	0.6332	0.0209
14:04	6.0354	0.8704	0.5795	0.0141
14:34	6.0360	0.9701	0.7508	0.0305
15:04	6.1802	0.8791	0.5894	0.0181
15:34	6.5435	0.9877	0.7218	0.0250
16:19	7.2968	1.4037	1.6172	0.1248
16:34	7.1318	1.1293	1.0535	0.0461
16:49	7.0426	1.1343	0.9478	0.0343
17:04	6.9063	1.1844	1.0392	0.0285

Table 7: Number concentration for July 18, 2014, in  $\text{cm}^{-3}$ , diameters for the four bins are in  $\mu\text{m}$  at the header.

Time	.3-0.5	0.5-1.0	1.0-5.0	>5.0
14:23	11.7896	0.9450	0.5641	0.0312
14:38	13.1629	1.3769	0.7257	0.0263
14:53	12.5170	1.0839	0.6453	0.0476
15:08	12.9462	0.9116	0.6354	0.0355
15:23	13.1291	1.0501	0.6584	0.0252
15:38	12.5332	0.9033	0.5998	0.0250
15:53	13.3357	0.9103	0.6015	0.0285
16:08	13.2753	0.8868	0.5405	0.0188
16:23	14.1010	1.0470	0.6124	0.0250
16:38	13.9976	0.9087	0.5704	0.0228
16:53	14.0923	0.9930	0.5879	0.0209
17:08	15.8491	1.2358	0.6392	0.0201
17:23	15.1262	0.9123	0.5542	0.0239
17:38	14.9795	0.9166	0.5408	0.0208
17:53	16.3175	1.2138	0.6337	0.0204
18:08	16.4879	1.3486	0.9042	0.1985
18:23	16.3520	1.0622	0.5709	0.0201
18:38	18.6764	1.5216	0.6742	0.0190
18:53	16.8534	1.0222	0.5398	0.0185
19:08	19.2067	1.3065	0.6371	0.0183
19:23	17.2035	1.2483	0.7332	0.0298
19:38	17.3083	1.1985	0.6467	0.0266
19:53	17.8135	1.3556	0.7683	0.0331
20:08	21.0226	2.0410	1.1902	0.0529
20:23	17.6707	1.4320	1.0270	0.0513
20:38	18.3794	1.7029	1.2989	0.0682
20:53	20.0397	1.6091	1.1603	0.0616
21:08	16.2276	1.0605	0.6463	0.0312
21:23	16.5419	1.2291	0.7764	0.0360
21:38	14.5538	0.9315	0.5521	0.0174
21:53	14.5322	0.9636	0.5751	0.0192
22:08	14.8350	0.9345	0.5609	0.0181
22:23	15.2147	0.9612	0.5869	0.0215
22:38	15.5077	1.0979	0.7197	0.0231
22:53	14.8325	0.9386	0.5899	0.0183
23:08	16.1260	1.2330	0.6960	0.0190
23:23	15.3612	1.1773	0.6766	0.0186
23:38	15.1179	1.0528	0.5974	0.0195
23:53	14.4713	0.9488	0.5490	0.0163

Table 8: Days selected and values of relative humidity and particle concentration for April 13 and July 18, 2014, in the PdN Airshed.

Day/Variable(mean)	04/13/13	07/18/14
RH	0.156	0.351
0.3-0.5, $\text{cm}^{-3}$	10.468	15.580
0.5-1.0, $\text{cm}^{-3}$	2.369	1.145
1.0-5.0, $\text{cm}^{-3}$	2.287	0.687
>5.0, $\text{cm}^{-3}$	0.145	0.032
pm2.5, $\mu\text{g}/\text{m}^3$	7.092	5.621
pm10, $\mu\text{g}/\text{m}^3$	27.458	19.504

### 2.4.2 Input Process

Due to the irregularity of the particles suspended in the air, it is difficult to obtain single measurement parameters to describe them like for example the diameter of the particles. It is in such cases that an equivalent diameter of a sphere of equivalent volume with the same physical properties is used to classify them. Such classifications are grouped in bins of diameters or radii by particle counter instruments.

The particle laser counter measures the particle number concentration  $N$  in four bins of diameters of  $0.3\text{-}0.5\mu\text{m}$ ,  $0.5\text{-}1.0\mu\text{m}$ ,  $1.0\text{-}5.0\mu\text{m}$ , and  $>5.0\mu\text{m}$ . These measurements in units of particles per  $\text{ft}^3$  are converted in standard units of particles per  $\text{cm}^3$ . These measurements are done every 15 minutes and operates simultaneously with the acoustic extinctions. Data from the particle counter is extracted through the serial port and downloaded to storage device (see section 2.1.1). This data are stored in format time HH:MM:SS per day which it is reformed to HH:MM for better comparison with the acoustic extinctions. The conversion and the selection of the distribution is done in the flowchart of fig. 11 in the subroutine stat.f90, where the parameters for the log-normal distribution with the input parameters like the one in eq. (13) is given.

For all the cases where values of relative humidity are present, the hygroscopic

growth of the particle was considered and calculated from Hänel [32].

$$r \approx r_0(1 - RH)^\varepsilon \quad (102)$$

where RH is the relative humidity ( $\leq 1$ ),  $r_0$  is the initial particle radius,  $r$  is the new radius, and  $\varepsilon$  was assumed as 0.23 which is the mean value of 0.25, 0.25, 0.255, 0.18, and 0.20 for five different aerosol types studied before [33].

The composite index of refraction was calculated by using the volume-weighted method which is explained in section 1.1.4. The two species considered in the study were mineral dust ( $n = 1.53 + i0.0080$ ,  $\rho_{\text{md}} = 2.39$ ) and soot ( $n = 1.872 + i0.6887$ ,  $\rho_{\text{soot}} = 2.00$ ) which are the two main components of the air for El Paso del Norte region, and interpolated to the wavelength  $0.87\mu\text{m}$  under a single rule of three [3]. This consideration is based in old aerosol studies in the region due to the complex topography and location of the mountains and river valley in the El Paso del Norte region which results in a constrained air basin where, on calm days, especially in the winter, anthropogenic air pollution is trapped over the metropolitan area [34]. On windy days, especially during the winter and early spring, mineral dust and sand blowing out of the surrounding desert causes high particulate matter concentrations [35]. The main component of soot is elemental carbon with density of  $\rho = 2.0 \text{ g cm}^{-3}$ , and on the other side, mineral dust has many components and for this region the density and refraction index was assumed as a simplified composition of 90%  $\text{SiO}_2$  9%  $\text{CaCO}_3$ , and 1%  $\text{Fe}_2\text{O}_3$  as it is shown in table 9.

As it was mentioned, the T-matrix and the LISA codes were used to determine the cross sections for both low and high relative humidity cases respectively for non-spherical and randomly oriented particles. The cross section values calculated

were multiplied by the number density obtained from the particle laser counter and described in the equations (26), (27), and (28), and therefore the values of extinction, scattering, and absorption coefficients were obtained. These computed coefficient values were compared against the acoustic extinciometer for each measured time of day. Also, values the Müller matrices  $F_{11}$ ,  $F_{12}$ ,  $F_{22}$ ,  $F_{33}$ ,  $F_{34}$ , and  $F_{44}$ , were calculated and plotted for better analysis at selected hours.

Finally, the values of single scattering albedo (SSA) were retrieved for the wavelengths of  $0.87 \mu\text{m}$  by using the direct-to-diffuse (DDR) method. This method consists of changing the values of SSA in the TUV code to obtain outputs of direct-to-diffuse irradiance ratios and comparing them against values obtained from the Visible-MFRSR instrument using error percent relative error  $\delta_{\text{SSA}}$ , as is shown in the following equation:

$$\delta_{\text{SSA}} = \frac{|DDR_{\text{MFRSR}} - DDR_{\text{TUV}}|}{DDR_{\text{MFRSR}}} \quad (103)$$

Table 9: Physical constant of species used in refractive index and density calculations (courtesy, Hand, J. L., et al. [36])

Species	Density (g cm <sup>-3</sup> )	Refractive index
H <sub>2</sub> SO <sub>4</sub>	1.8	1.408
NH <sub>4</sub> HSO <sub>4</sub>	1.78	1.479
(NH <sub>4</sub> ) <sub>3</sub> H(SO <sub>4</sub> ) <sub>2</sub>	1.83	1.527
(NH <sub>4</sub> ) <sub>2</sub> SO <sub>4</sub>	1.76	1.531
Organic Carbon	1.4	1.55
Elemental Carbon	2.0	1.96-0.66i
NaNO <sub>3</sub>	2.261	1.587
SiO <sub>2</sub>	2.32	1.486
Al <sub>2</sub> O <sub>3</sub>	3.97	1.765
Fe <sub>2</sub> O <sub>3</sub>	5.24	3.011
CaO	3.3	1.833
MgO	2.58	1.735
TiO <sub>2</sub>	4.23	2.58

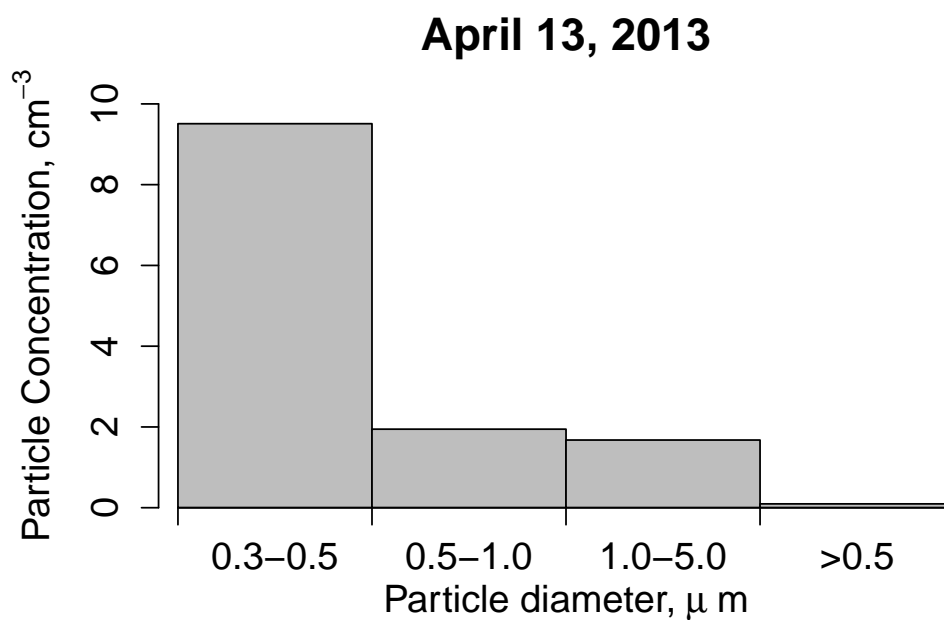


Figure 12: Averaged particle concentration, cm<sup>-3</sup> on April 13, 2013.

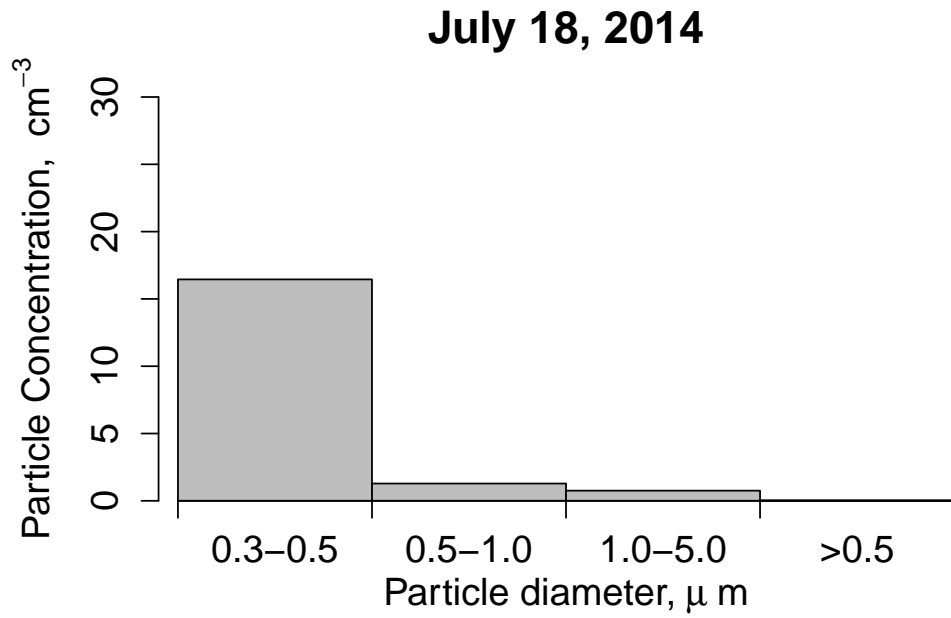


Figure 13: Averaged particle concentration,  $\text{cm}^{-3}$  on July 18, 2014.

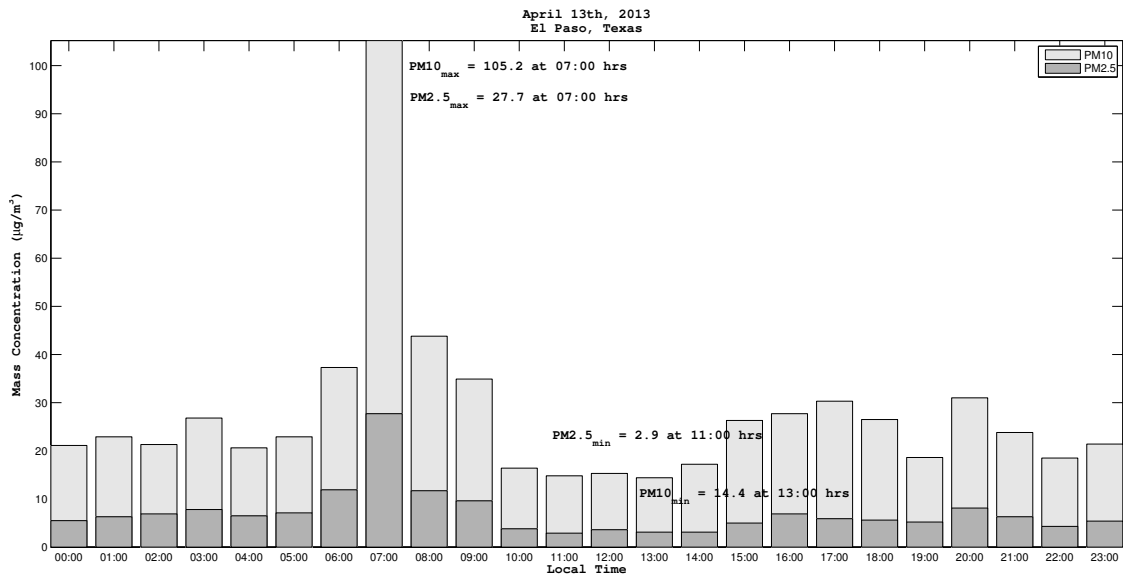


Figure 14: Mass concentration ( $\mu\text{g}/\text{m}^3$ ) on April 13, 2013.

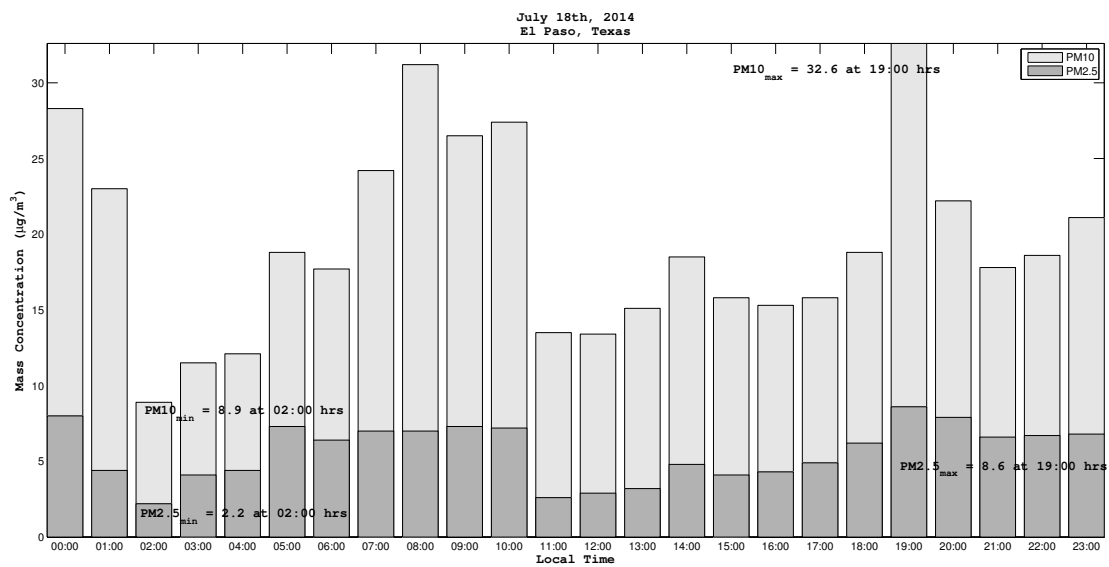


Figure 15: Mass concentration ( $\mu\text{g}/\text{m}^3$ ) on July 18, 2014.

## CHAPTER 3

### Results and Discussion

Values of the scattering and extinction cross sections were calculated with both models, non relative humidity model (T-matrix), which does not consider hygroscopic growth, and the one which consider relative humidity (LISA), which consider hygroscopic growth and consequently core-shell geometry. Number concentration of the particles in  $\text{ft}^{-3}$  were obtained from the laser particle counter at their four channels and then converted to units of  $\text{particles}/\mu\text{m}^3$ . The scattering and extinction coefficients were obtained by using the formula

$$B_{\text{sca}} = \sum_{i=0}^{N_B} n \cdot C_{\text{sca}} \quad (104a)$$

$$B_{\text{ext}} = \sum_{i=0}^{N_B} n \cdot C_{\text{ext}} \quad (104b)$$

where  $N_B$  is the number of bins of the particle counter,  $C$  are the cross sections, and the values for  $B_{\text{abs}}$  was obtained directly from the equation

$$B_{\text{abs}} = B_{\text{ext}} - B_{\text{sca}} \quad (105)$$

Equations (104a), (104b), and (105) are valid for scattering by individual or ensemble of particles and the single-scattering theory can be used even in the more concentrated atmospheric conditions if the average distance between particles is large compared to the particle size [2].

Each coefficient value was calculated with the model and then compared with the

ones from the acoustic extinciometer per hour. Figures 16 and 30 show the comparison between  $B_{\text{sca}}$  coefficients calculated from dry simulation model, simulation with humidity and values from the acoustic extinciometer along with values of humidity for the days selected.

The elements of the T-matrix for a randomly oriented, axially symetric particles are plotted for the radius  $q = r_{\text{int}}/r_{\text{ext}}$  of the day cases selected. This plots are per angular distribution and the Müller matrix form is given by equation (100). Values of  $q$  are very close to one for all the cases where relative humidity is less than 40% which is true for an arid region as El Paso, where the hygroscopic growth from equation (102) does not present changes around the core. The low relative humidity values does not allow us to make a complete visualization of the properties of the hygroscopic growth of the particles and the two models apparently show the same results. However, we have selected some hours where the scattering coefficients, the angular scattering patterns, and the polarization gives us important information about the shape and orientation of the particles.

### 3.1 April 13, 2013

The first case run was the one with low relative humidity. Values of scattering coefficients, composite index of refraction and mass concentration during the day are shown in table 10. Due to the low relative humidity, this day did not show major changes in the particle and not hygroscopic growth was detected. Also, as it is seen the values of composite index of refraction are more close to mineral dust and only at certain hours this index changes to more presence of soot or black carbon. The scattering coefficient results also are plotted in figure 16. The two models describe correctly the behavior of the instrument. At 7:49 AM however, there is an increasing in scattering that the model with humidity follows correctly. This peak correspond to a change in the number concentration which is doubled at that time as it can be seen in table 6 and therefore increasing tremendously the scattering to ten times. This change can be easily seen from the TCEQ in fig. 14 where particles matter of  $2.5 \mu\text{m}$  and  $10.0 \mu\text{m}$  in diameter is greater at around 7:00 AM and before 8:00 AM in this day.

For the first nonzero Müller matrix element,  $F_{11}$  from figures 17 and 18 we can see the angular scattering patterns for April 13, 2013 at 7:49 AM and 8:04 AM respectively. This selection was based on the increase of the scattering coefficient at that time interval. We can see in these plots that the particle scattering follows Rayleigh scattering as it shows symmetrical and isotropic scattering for bins 1-3 (small size parameters) and forward-backward assymetry for bin 4 [11]. Rayleigh scattering also describe complete polarization or not scattering at 90 degrees as it is proved in eq. (72). Unfortunately, due to the low values of relative humidity, it is not possible to see the changes of  $F_{11}$  for changes of  $q$  at any angle.

Table 10: Time (hh:mm),  $B_{\text{sca}}$  ( $\mu\text{m}^{-3}$ ) of instrument, LISA model, T-matrix model, Relative Humidity (%), and Index of Refraction for composite material for April 13, 2013

Time	Instrument	LISA	T-matrix	RH	n = m + i k
06:19	10.430	8.147	11.879	16.653	1.530 + i 0.008
06:34	21.316	35.835	25.772	17.106	1.872 + i 0.688
06:49	12.032	11.253	14.172	17.085	1.530 + i 0.008
07:04	20.922	11.219	16.827	16.755	1.530 + i 0.008
07:19	30.382	30.301	33.882	16.253	1.682 + i 0.310
07:34	14.684	17.227	20.643	16.616	1.872 + i 0.688
07:49	24.729	12.270	14.538	16.592	1.530 + i 0.008
08:04	399.869	397.499	277.860	16.497	1.530 + i 0.008
08:19	369.796	343.745	238.139	16.795	1.530 + i 0.008
08:34	19.191	24.510	25.903	16.806	1.872 + i 0.688
08:49	37.720	29.332	33.222	16.672	1.530 + i 0.008
09:04	16.504	14.720	22.995	16.656	1.530 + i 0.008
09:19	16.393	14.861	19.640	16.533	1.530 + i 0.008
09:34	20.288	23.174	23.984	16.586	1.872 + i 0.688
09:49	22.363	17.973	21.827	16.691	1.530 + i 0.008
10:04	16.394	13.886	16.510	16.602	1.530 + i 0.008
10:19	16.937	16.977	17.847	16.599	1.813 + i 0.570
10:34	12.578	13.054	15.607	16.569	1.872 + i 0.688
10:49	14.368	10.881	14.899	16.564	1.530 + i 0.008
11:04	10.690	9.436	10.712	16.521	1.530 + i 0.008
11:19	7.073	11.699	10.423	16.359	1.872 + i 0.688
11:34	5.649	3.919	6.624	16.277	1.530 + i 0.008
11:49	12.302	31.797	14.880	15.875	1.872 + i 0.688
12:04	10.861	11.427	11.022	15.497	1.872 + i 0.688
12:19	6.725	21.993	12.200	15.506	1.872 + i 0.688
12:34	7.828	8.000	8.102	15.232	1.872 + i 0.688
12:49	21.884	28.278	15.929	15.023	1.872 + i 0.688
13:04	8.462	9.366	8.4080	14.954	1.872 + i 0.688
13:19	3.280	18.106	11.466	14.713	1.872 + i 0.688
13:34	7.425	8.430	8.138	14.534	1.872 + i 0.688
13:49	5.769	5.755	7.521	14.673	1.646 + i 0.238
14:04	2.986	4.111	6.634	14.390	1.872 + i 0.688
14:34	5.470	9.844	8.713	14.464	1.872 + i 0.688
15:04	6.574	5.560	6.900	14.109	1.530 + i 0.008
15:34	6.106	7.129	8.330	13.737	1.872 + i 0.688
16:19	15.422	42.356	19.859	12.652	1.872 + i 0.688
16:34	11.468	13.678	11.892	12.737	1.872 + i 0.688
16:49	6.473	9.830	10.611	12.764	1.872 + i 0.688
17:04	12.608	9.199	11.851	12.705	1.530 + i 0.008

Figures 19 and 20 show the  $F_{22}$  element with values near to unity for bins 1-3 indicating sphericity in these radii ranges. For bin 4, the particles are bigger than the wavelength and this matrix element goes from close to unity to 0.8. This indicates that for bigger particles this element can detect particles shapes at  $0.87 \mu\text{m}$  at the backscattering angle.

The matrix elements  $F_{33}/F_{11}$  and  $F_{44}/F_{11}$  in figures 21 and 22, show similarity in values ( $F_{33} = F_{44}$ ), also the fast variation of these parameters with the change of the angle indicates that the particles are more likely spheres.

The matrix element  $F_{12}/F_{11}$  indicates linear polarization. Its formulation is expressed with negative sign in some texts and we followed the convention of Bohren and Hauffman [11], however the negative sign can be removing and we will arrive to the same conclusions. From figures 25 and 26, we can observe that the light is complete polarized at  $90^\circ$  indicating Rayleigh effect as it is described by eq. (72). Figures also show that for spherical particles, polarization reaches extremes indicating again the spherical shape of particles.

For bins 1 and 2, the matrix element  $F_{34}/F_{11}$  does not show polarization at all. This can occur due to the size of the particle with respect to the wavelength. However for bins 3 and 4, this element shows strong dependence of core and angle which is true for spheres than for spheroids. Also, this ratio does not reach extreme values ( $\pm 1$ ) leading to the conclusion of nonspheres particles according to section 2.3.5.

The retrieval of single scattering albedo in fig. 29, shows that scattering occurs most frequently. The values of SSA are greater than 0.6 for all time of the day with some dips for certain hours and with maximum at 13:00 - 14:00 hrs.

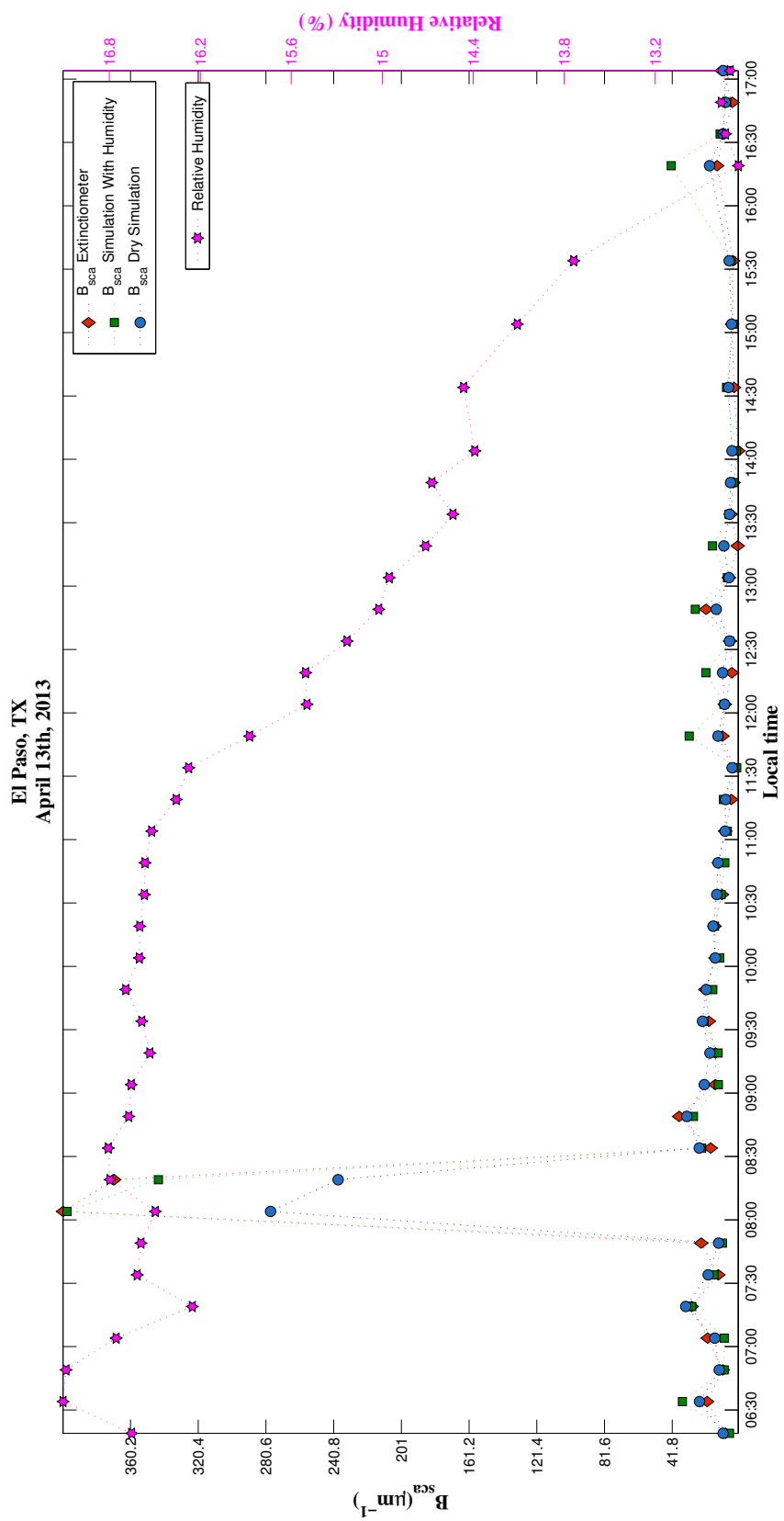


Figure 16:  $B_{sca}$  Coefficients for April 13th, 2013. Look at the high peak at 7:49AM.

April 13, 2013, at 07:49 AM

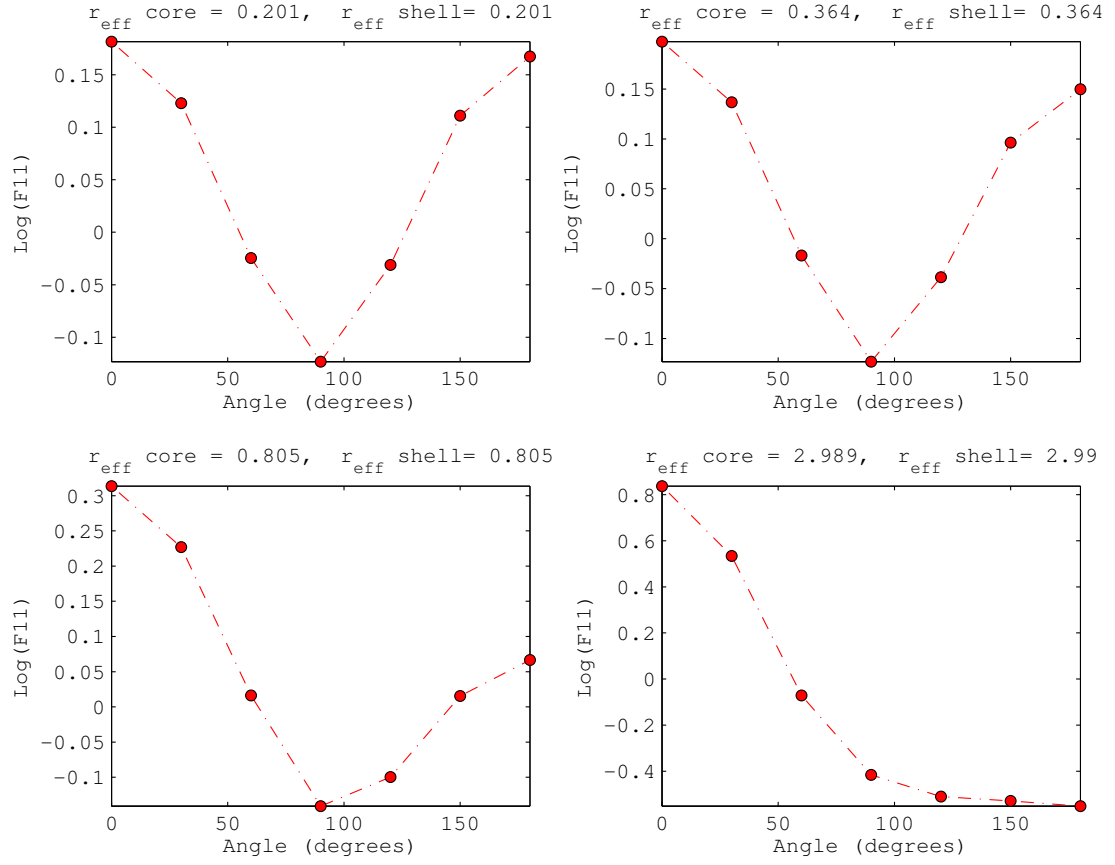


Figure 17:  $\text{Log}(F_{11})$  Müller matrix element for an ensemble of oblate spheroids as a function of scattering angle  $\theta$  and relative core size  $q$  for April 13, 2013 at 7:49 AM.

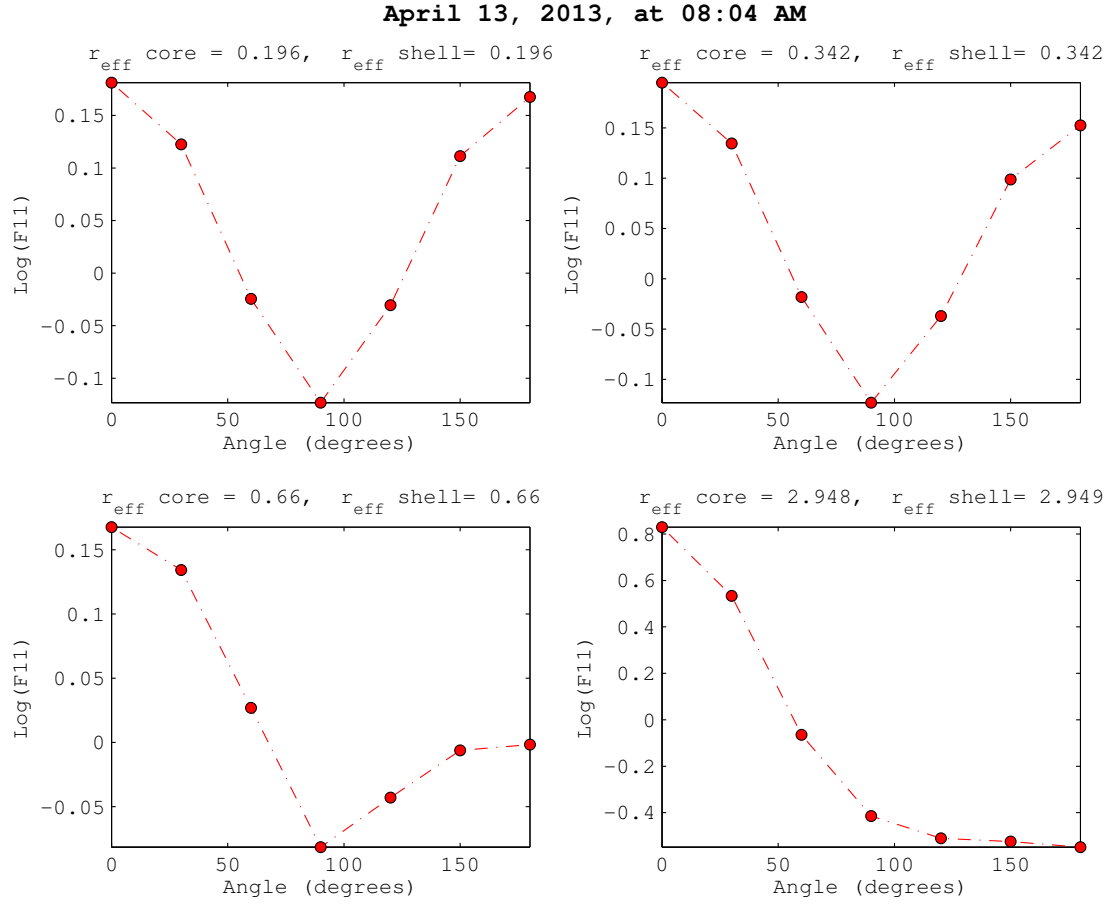


Figure 18:  $\text{Log}(F_{11})$  Müller matrix element for an ensemble of oblate spheroids as a function of scattering angle  $\theta$  and relative core size  $q$  for April 13, 2013 at 8:04 AM.

April 13, 2013, at 07:49 AM

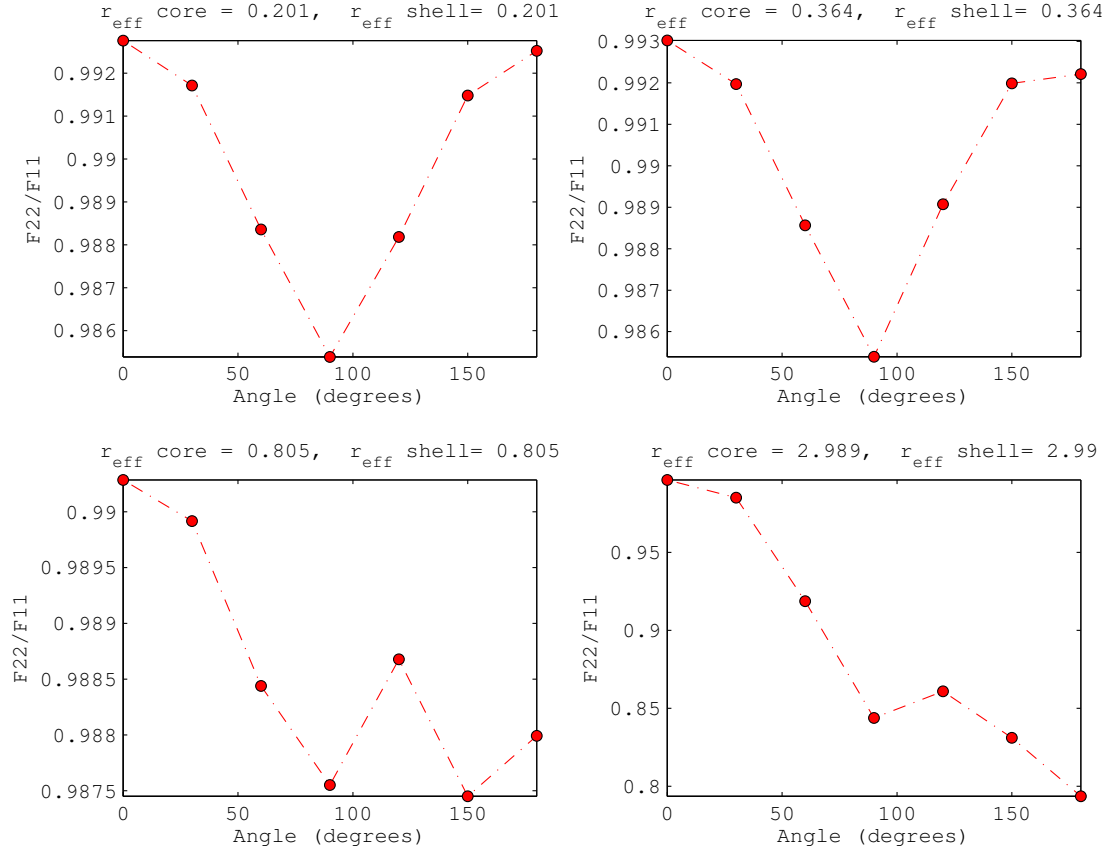


Figure 19:  $F_{22}/F_{11}$  Müller matrix element for an ensemble of oblate spheroids as a function of scattering angle  $\theta$  and relative core size  $q$  for April 13, 2013 at 7:49AM.

April 13, 2013, at 08:04 AM

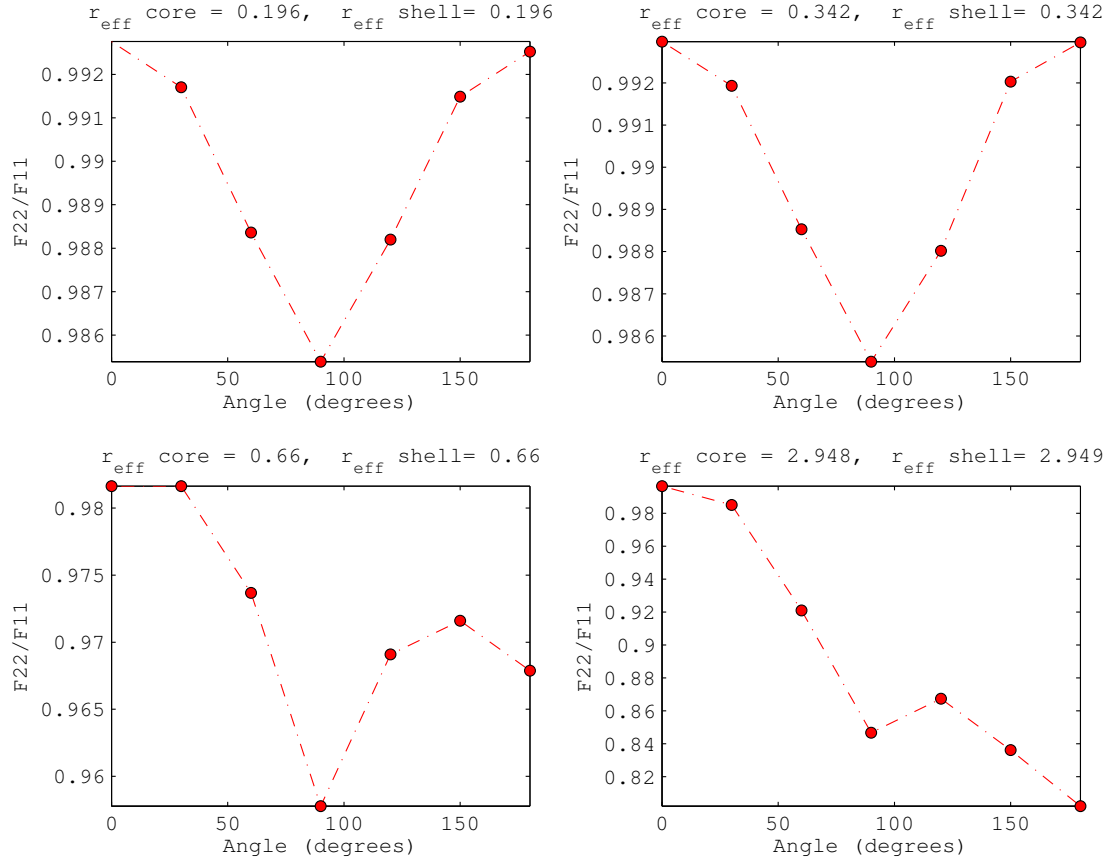


Figure 20:  $F_{22}/F_{11}$  Müller matrix element for an ensemble of oblate spheroids as a function of scattering angle  $\theta$  and relative core size  $q$  for April 13, 2013 at 8:04AM.

April 13, 2013, at 07:49 AM

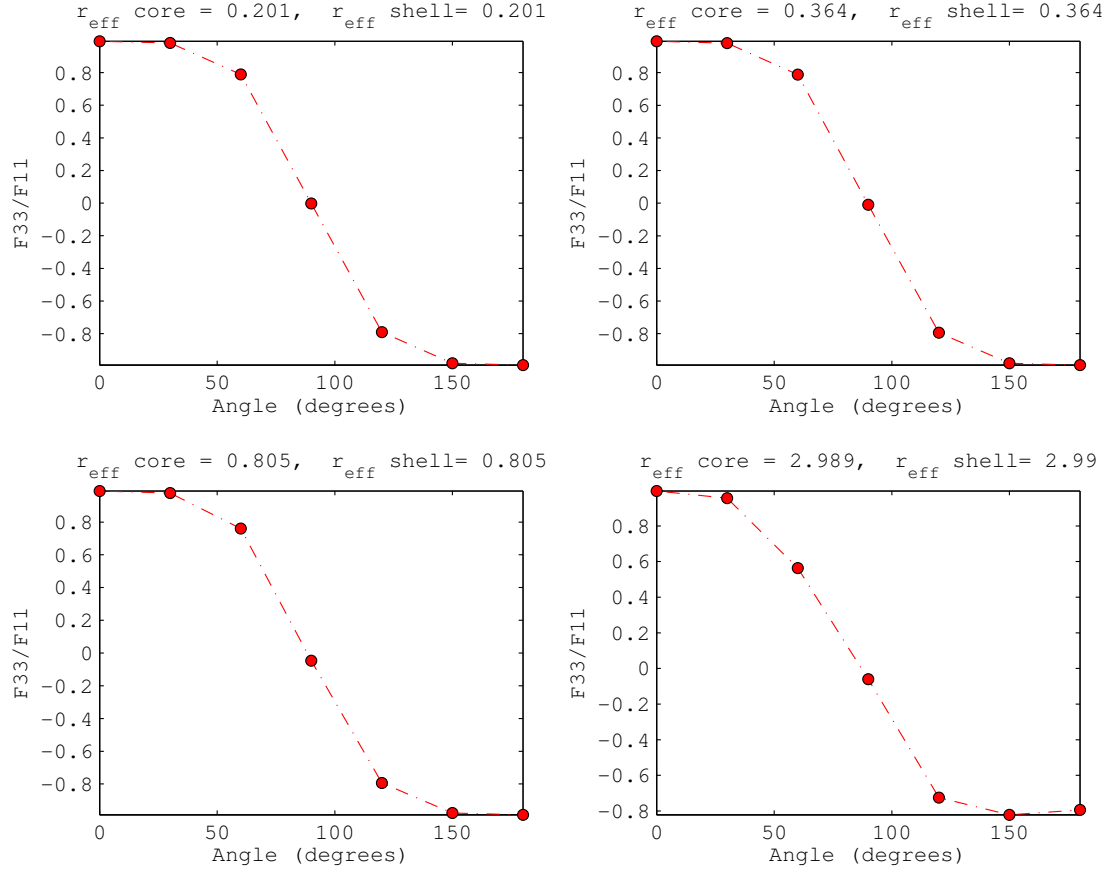


Figure 21:  $F_{33}/F_{11}$  Müller matrix element for an ensemble of oblate spheroids as a function of scattering angle  $\theta$  and relative core size  $q$  for April 13, 2013 at 7:49AM.

April 13, 2013, at 08:04 AM

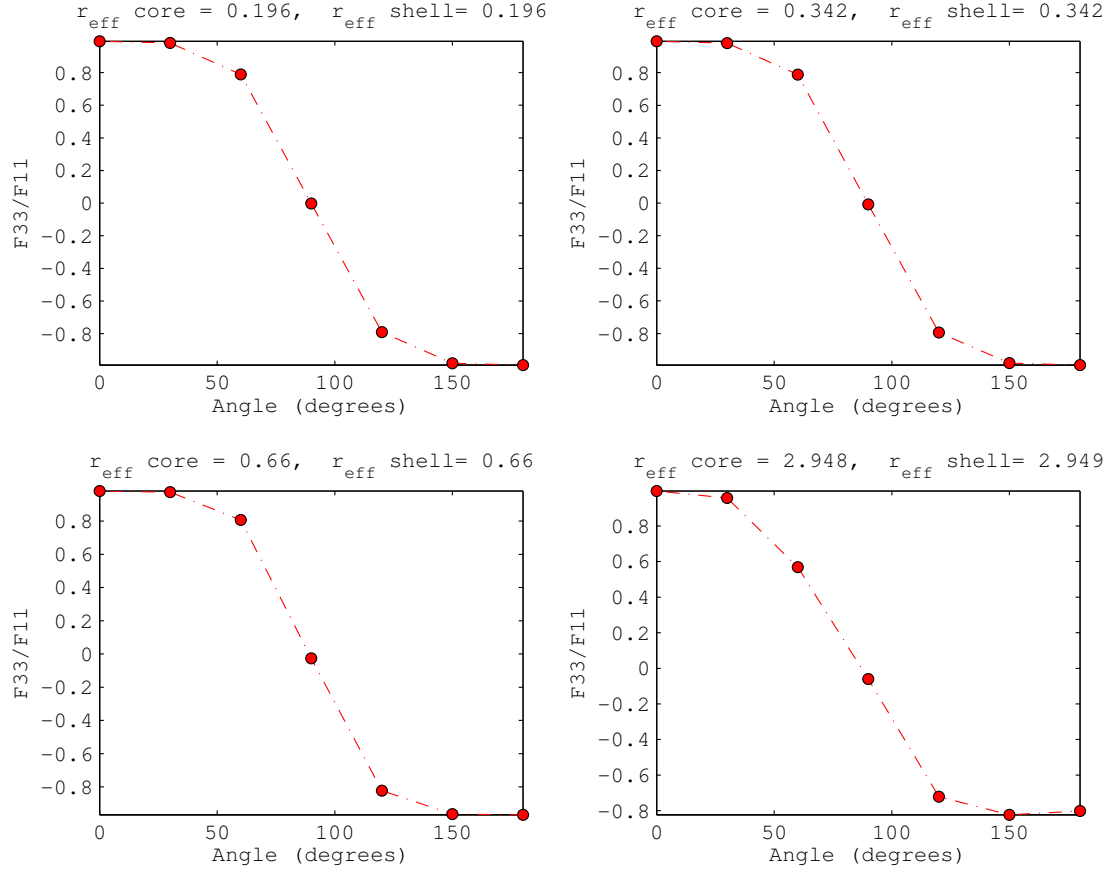


Figure 22:  $F_{33}/F_{11}$  Müller matrix element for an ensemble of oblate spheroids as a function of scattering angle  $\theta$  and relative core size  $q$  for April 13, 2013 at 8:04AM.

April 13, 2013, at 07:49 AM

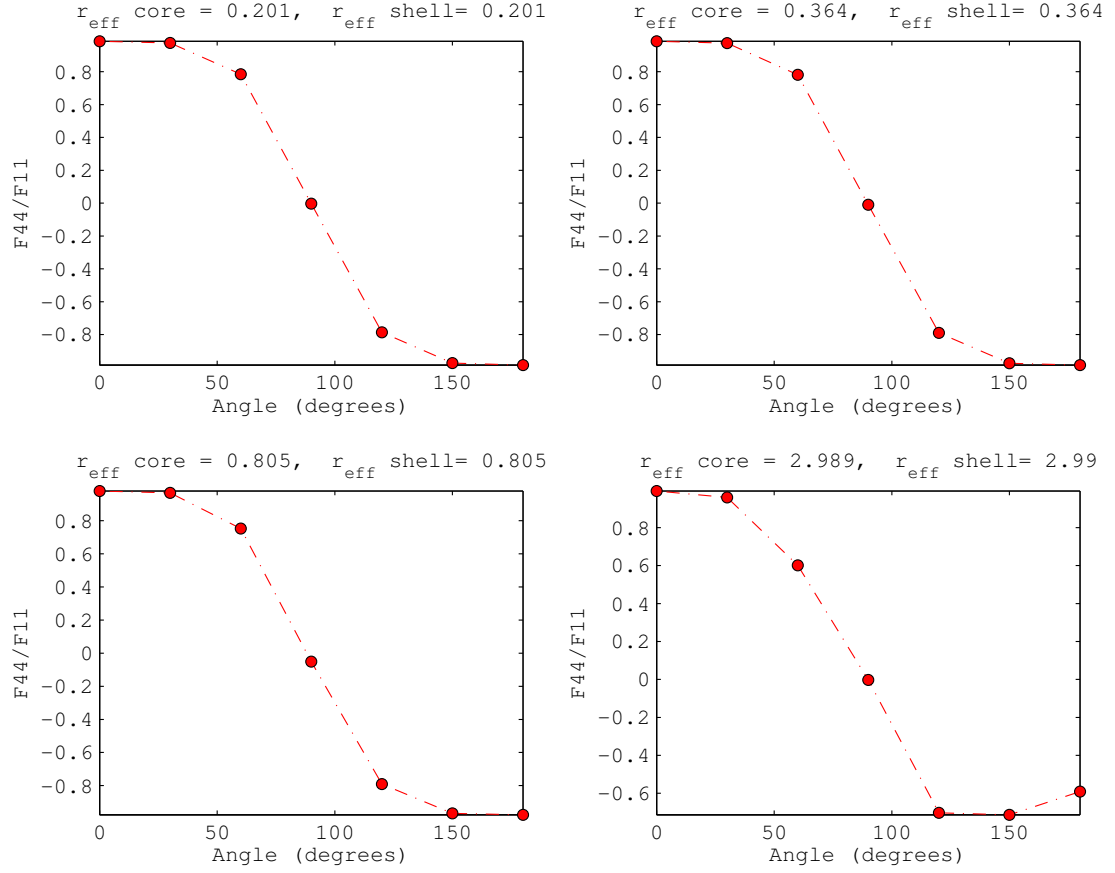


Figure 23:  $F_{44}/F_{11}$  Müller matrix element for an ensemble of oblate spheroids as a function of scattering angle  $\theta$  and relative core size  $q$  for April 13, 2013 at 7:49AM.

April 13, 2013, at 08:04 AM

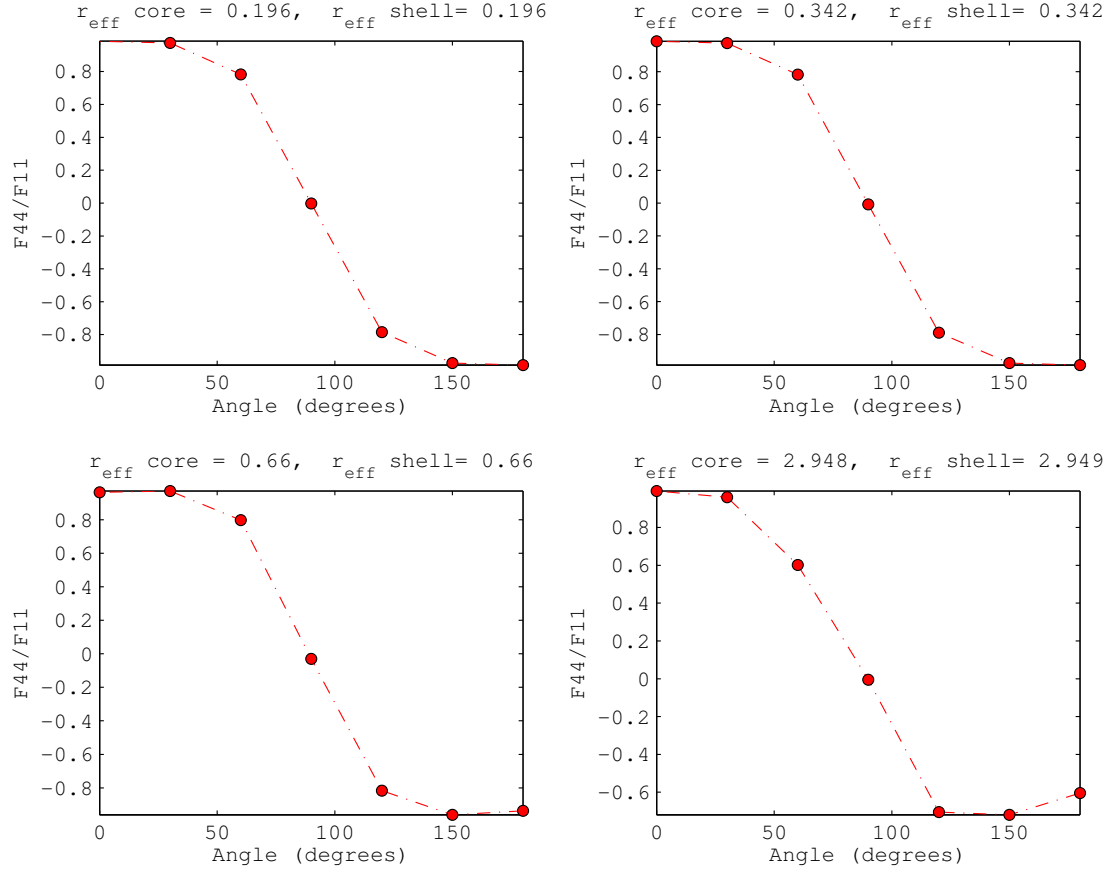


Figure 24:  $F_{44}/F_{11}$  Müller matrix element for an ensemble of oblate spheroids as a function of scattering angle  $\theta$  and relative core size  $q$  for April 13, 2013 at 8:04AM.

April 13, 2013, at 07:49 AM

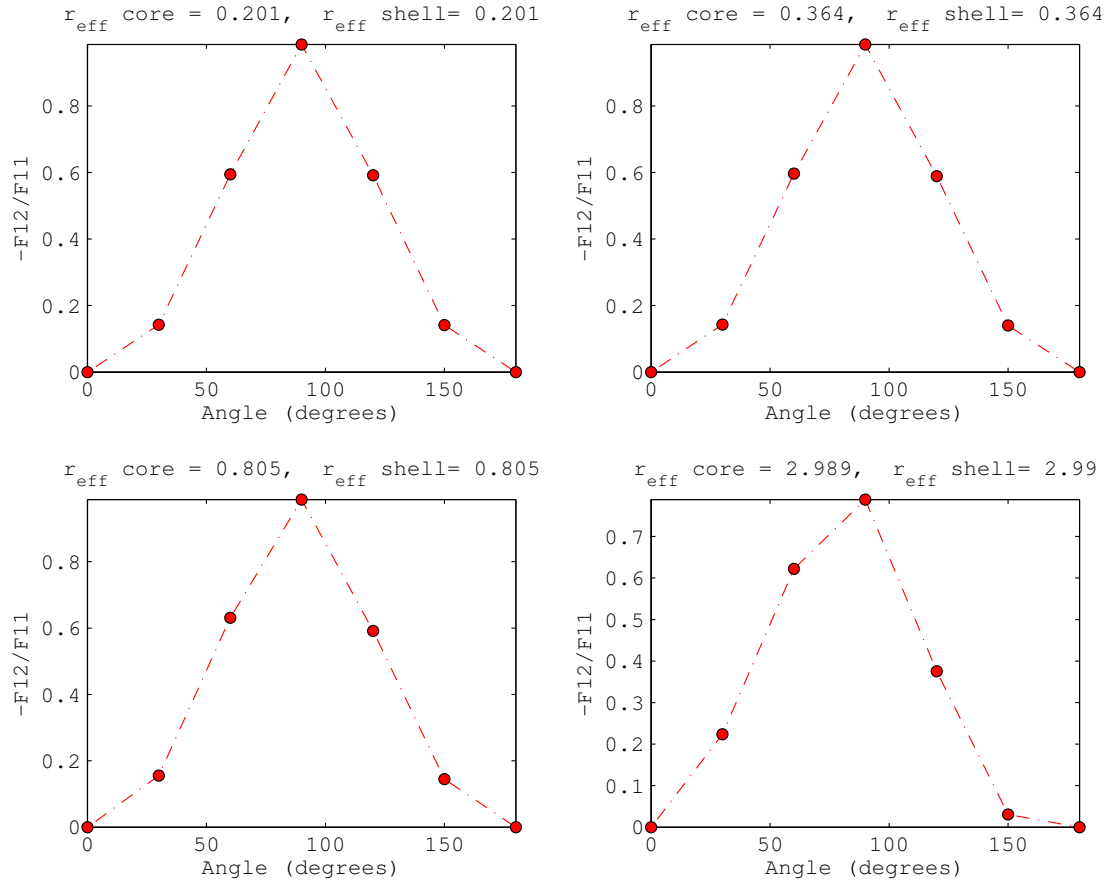


Figure 25:  $F_{12}/F_{11}$  Müller matrix element for an ensemble of oblate spheroids as a function of scattering angle  $\theta$  and relative core size  $q$  for April 13, 2013 at 7:49AM.

April 13, 2013, at 08:04 AM

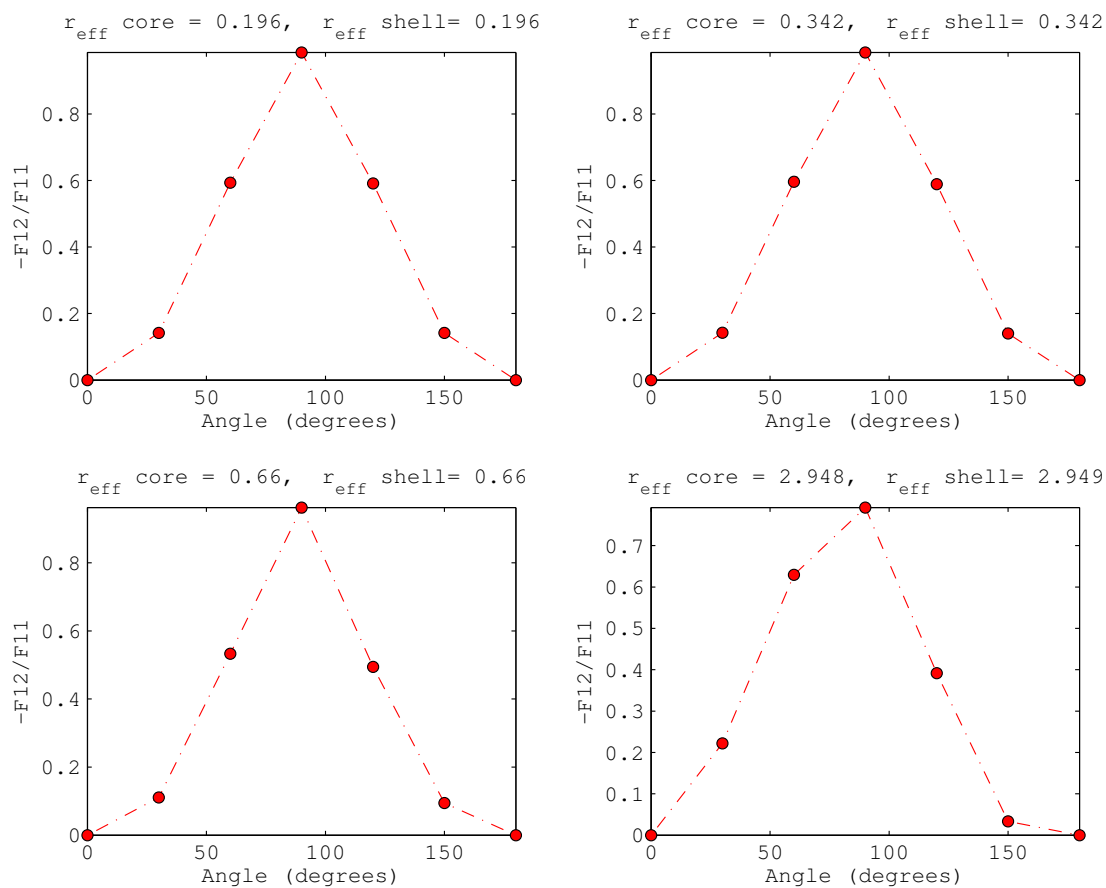


Figure 26:  $F_{12}/F_{11}$  Müller matrix element for an ensemble of oblate spheroids as a function of scattering angle  $\theta$  and relative core size  $q$  for April 13, 2013 at 8:04AM.

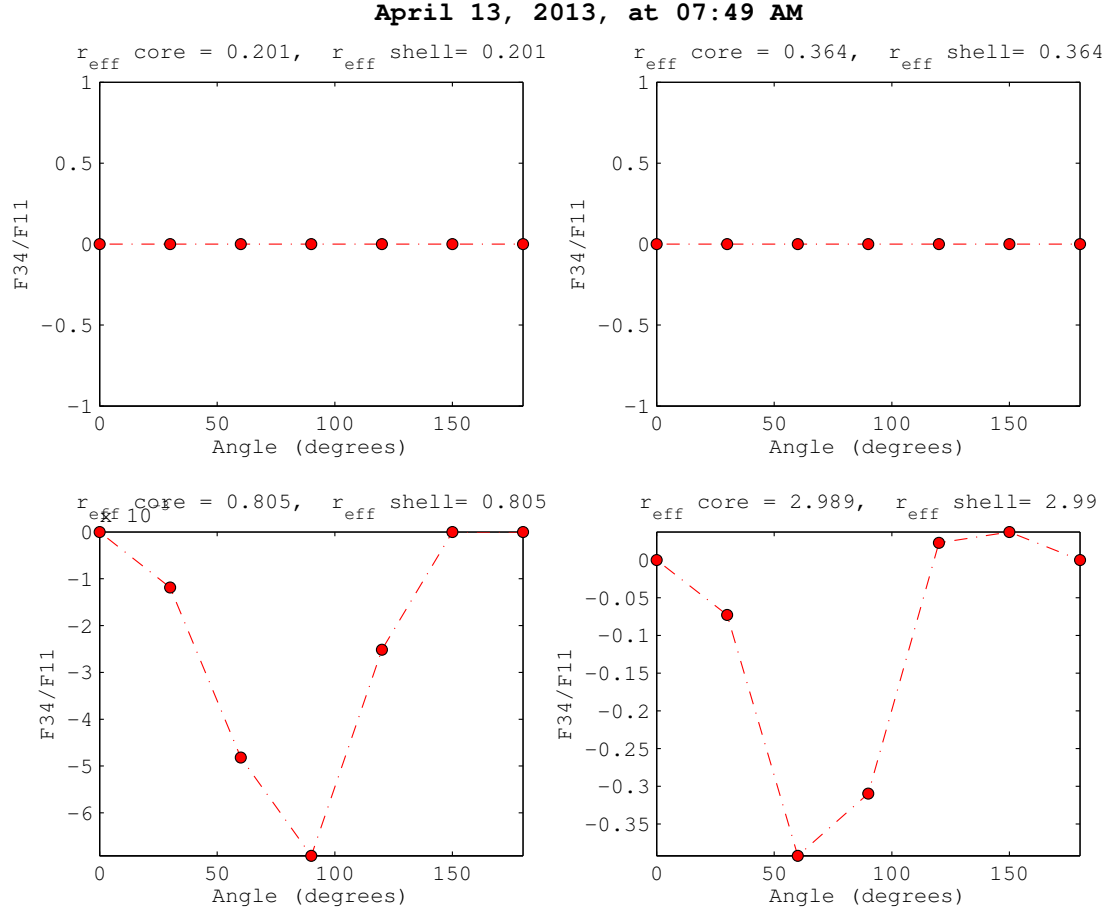


Figure 27:  $F_{34}/F_{11}$  Müller matrix element for an ensemble of oblate spheroids as a function of scattering angle  $\theta$  and relative core size  $q$  for April 13, 2013 at 7:49AM.

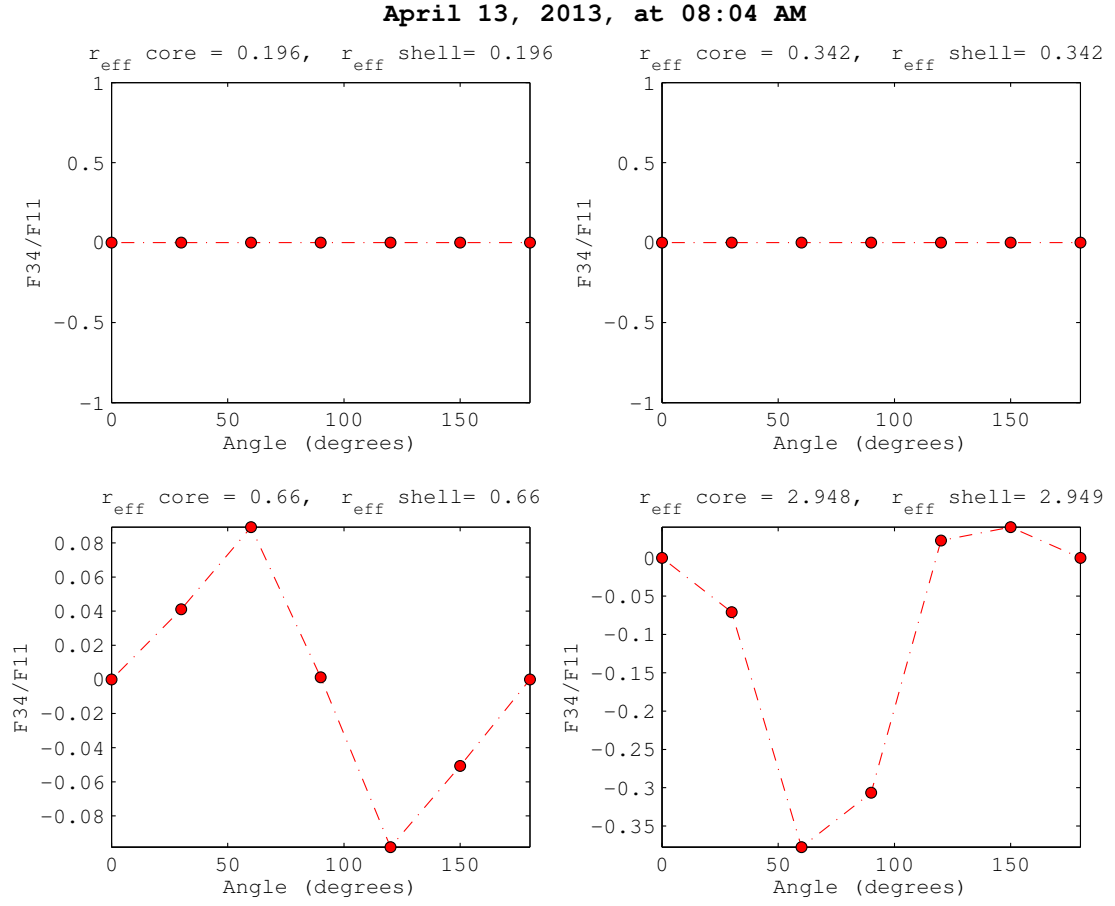


Figure 28:  $F_{34}/F_{11}$  Müller matrix element for an ensemble of oblate spheroids as a function of scattering angle  $\theta$  and relative core size  $q$  for April 13, 2013 at 8:04AM.

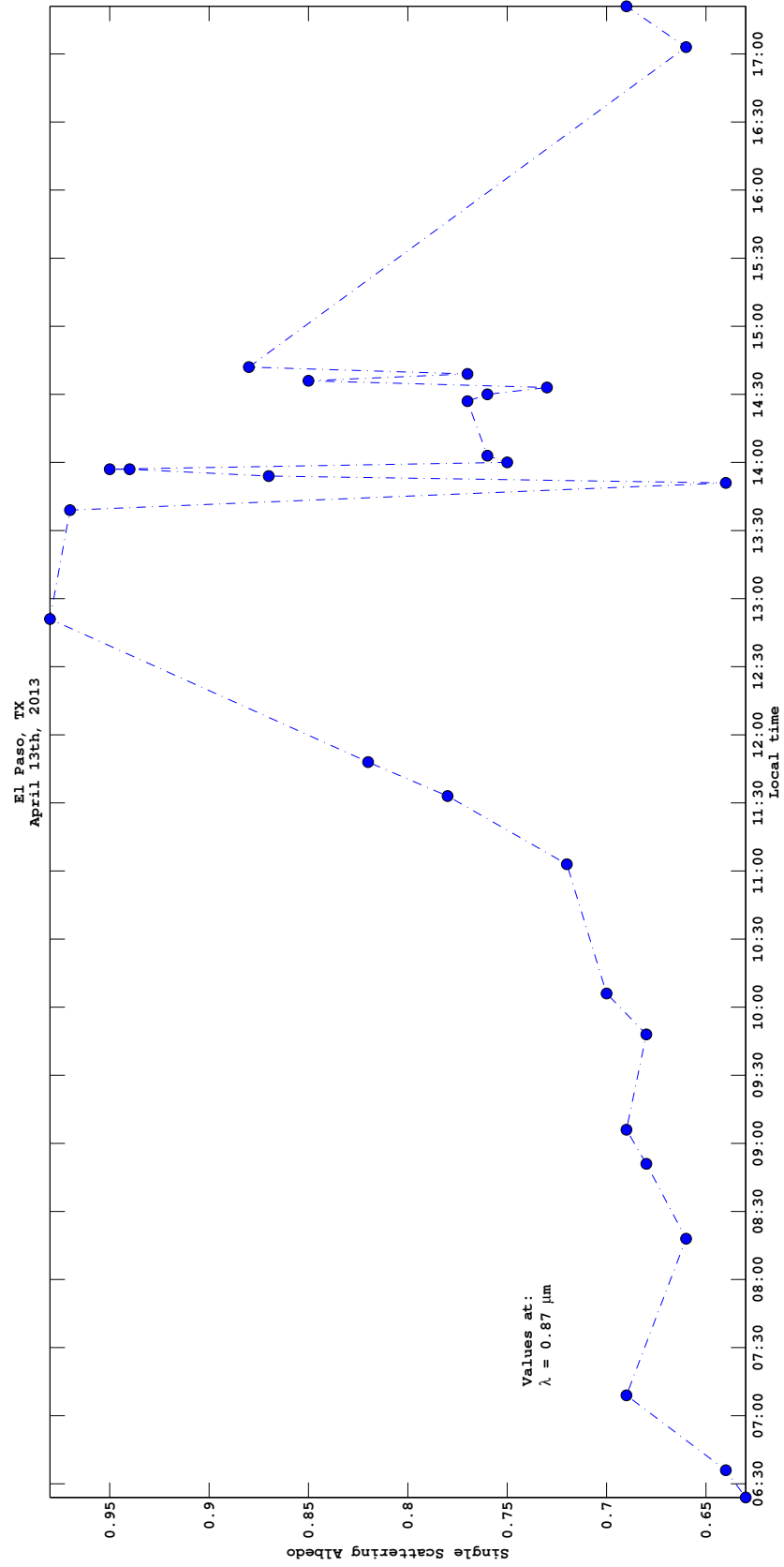


Figure 29: Single scattering albedo retrievals for April 13th, 2013.

### 3.2 July 18, 2014

The day with higher average relative humidity for the area was July 18, 2014. It can be seen from table 11 that the values of scattering coefficients are close in some times of day, however in general it is not so. The first analysis on this results is that the model with humidity underpredict values from the instrument, and the dry model shows a better behavior instead. This is understandable if we consider that the values of humidity does not allow a noticeable hygroscopic growth and therefore the shell is almost neglectable according to eq. (102). However, at relative humidity values higher than 40%, the model with humidity show a better approximation, like before 15:30 hrs (see fig. 16).

In the analysis of the Müller matrix elements  $F_{11}$ , from figures 31 and 32 we observe the same behavior as in the dry case, where the particles follow Rayleigh scattering as it shows symmetrical and isotropic scattering for bins 1-3 (small size parameters) and forward-backward assymetry for bin 4 as well. Also, the sphericity shape from particles in bins 1-3 is proved from figures 33 and 34 which shows again the  $F_{22}$  element with values near to unity. For bin 4, it is expected a better resolution when the size parameter  $x_{\text{eff}}$  is greater than the incident wavelength and therefore this element at this interval size deviates from unity, indicating nonsphericity.

As it happened in section 3.1, the matrix elements  $F_{33}/F_{11}$  and  $F_{44}/F_{11}$  in figures 33 and 34, show similarity in values ( $F_{33} = F_{44}$ ), and changing fast with angles indicating sphericity again, but not conclusions can be made before analyzing figures 39 and 39. For linear polarization, the matrix element  $F_{12}/F_{11}$ , it is observed from figures 37 and 38, we observe the same Rayleigh behavior, the unpolarized beam is complete polarized at  $90^\circ$  and also reaches extremes indicating again the spherical shape of particles.

From figures 39 and 40, the matrix element  $F_{34}/F_{11}$  does not show any change for the first bin, but it is interesting the behavior for bin 2, which show extreme values at  $60^\circ$  and  $120^\circ$  indicating nonsphericity and for bins 3 and 4, this element shows strong dependence of core and angle which is true for spheres.

Finally, the retrieval of single scattering albedo in fig. 41, also shows that scattering occurs most frequently with values above 0.6 for all time of day and also whows dips for certain hours and with maximum values of 0.96 at sometimes showing that the iar masses are mostly composed of scattering particles.

Table 11: Time (hh:mm),  $B_{\text{sca}}$  ( $\mu\text{m}^{-3}$ ) of instrument, LISA model, T-matrix model, Relative Humidity (%), and Index of Refraction for composite material for July 18, 2014

Time	Instrument	LISA	T-matrix	RH	$n = m + i k$
14:23	6.94	6.83	6.95	47.27	$1.53 + i 0.01$
14:38	10.91	5.74	8.50	46.11	$1.53 + i 0.01$
14:53	10.02	10.0	8.48	44.58	$1.75 + i 0.44$
15:08	6.84	7.18	7.38	42.83	$1.87 + i 0.69$
15:23	6.05	5.49	7.43	41.21	$1.53 + i 0.01$
15:38	7.51	5.46	7.29	41.86	$1.53 + i 0.01$
15:53	7.18	6.20	7.18	39.92	$1.53 + i 0.01$
16:08	6.96	4.07	6.85	39.23	$1.53 + i 0.01$
16:23	8.48	5.43	7.94	37.79	$1.53 + i 0.01$
16:38	6.21	4.96	6.89	38.03	$1.53 + i 0.01$
16:53	7.19	4.54	7.18	36.65	$1.53 + i 0.01$
17:08	8.12	4.35	8.10	36.09	$1.53 + i 0.01$
17:23	9.35	5.19	7.64	35.28	$1.53 + i 0.01$
17:38	7.55	4.51	7.39	35.55	$1.53 + i 0.01$
17:53	10.2	4.41	8.61	34.52	$1.53 + i 0.01$
18:08	7.87	40.41	16.25	35.39	$1.80 + i 0.69$
18:23	8.29	4.34	7.97	34.80	$1.53 + i 0.01$
18:38	8.25	4.11	8.95	33.62	$1.53 + i 0.01$
18:53	8.05	4.00	7.77	33.83	$1.53 + i 0.01$
19:08	7.78	3.95	8.52	33.24	$1.53 + i 0.01$
19:23	9.66	6.46	9.67	32.35	$1.53 + i 0.01$
19:38	9.56	5.75	9.22	32.37	$1.53 + i 0.01$
19:53	9.92	7.17	9.95	34.02	$1.53 + i 0.01$
20:08	11.16	11.16	14.27	34.05	$1.68 + i 0.31$
20:23	15.11	11.14	13.05	33.25	$1.53 + i 0.01$
20:38	12.99	13.78	15.17	31.43	$1.87 + i 0.69$
20:53	14.60	13.34	14.61	32.34	$1.53 + i 0.01$
21:08	13.86	6.76	9.18	31.21	$1.53 + i 0.01$
21:23	11.67	7.81	10.57	30.75	$1.53 + i 0.01$
21:38	9.78	3.78	7.63	30.91	$1.53 + i 0.01$
21:53	7.76	4.17	7.77	30.57	$1.53 + i 0.01$
22:08	10.15	3.92	7.76	30.87	$1.53 + i 0.01$
22:23	6.51	4.66	7.63	30.70	$1.53 + i 0.01$
22:38	7.36	5.01	8.73	30.85	$1.53 + i 0.01$
22:53	9.43	3.97	7.94	31.36	$1.53 + i 0.01$
23:08	8.41	4.12	8.65	31.04	$1.53 + i 0.01$
23:23	9.07	4.05	8.89	1.73	$1.53 + i 0.01$
23:38	9.13	4.23	8.19	31.75	$1.53 + i 0.01$
23:53	8.12	3.54	7.52	31.58	$1.53 + i 0.01$

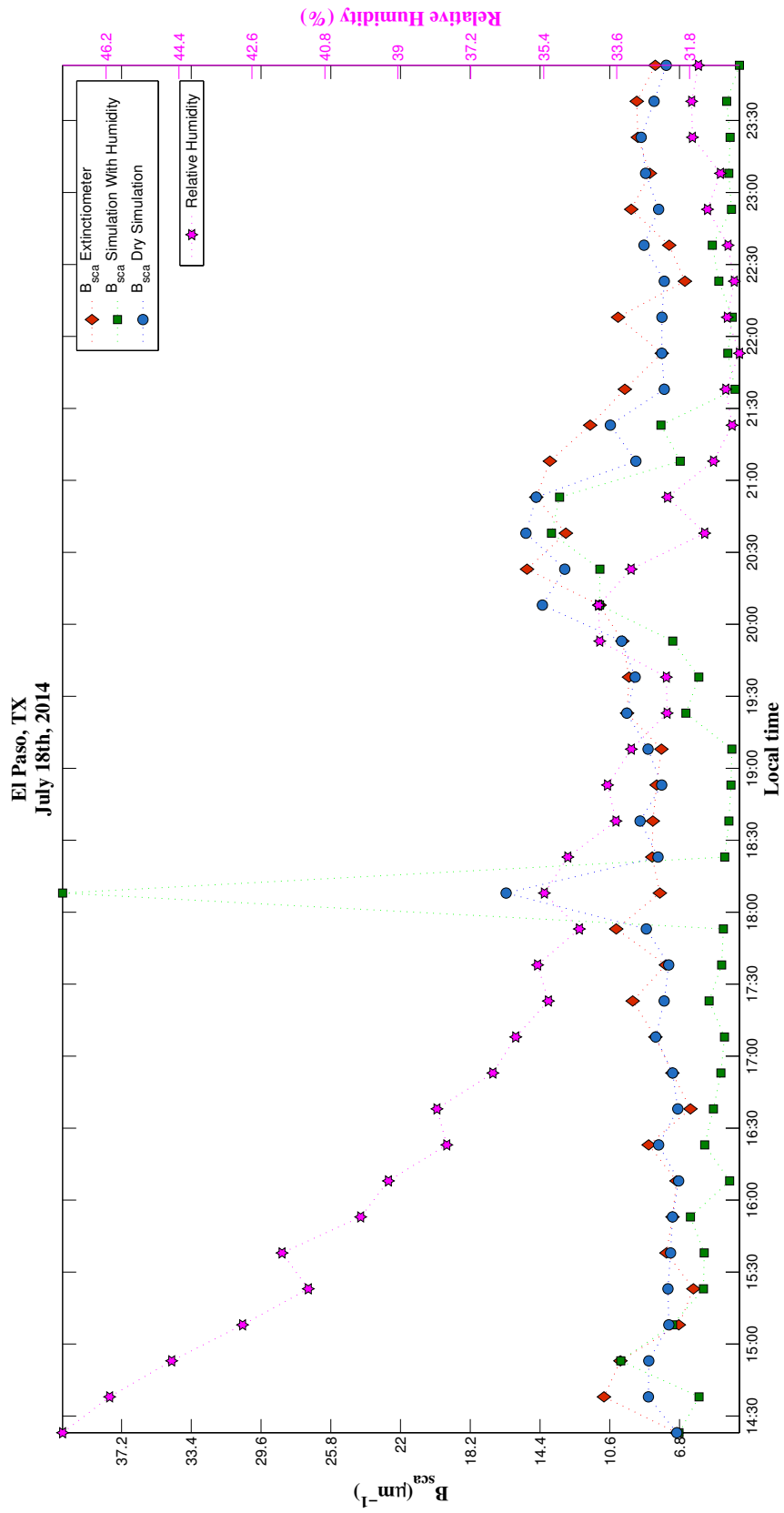


Figure 30:  $B_{sca}$  Coefficients for July 18th, 2014.

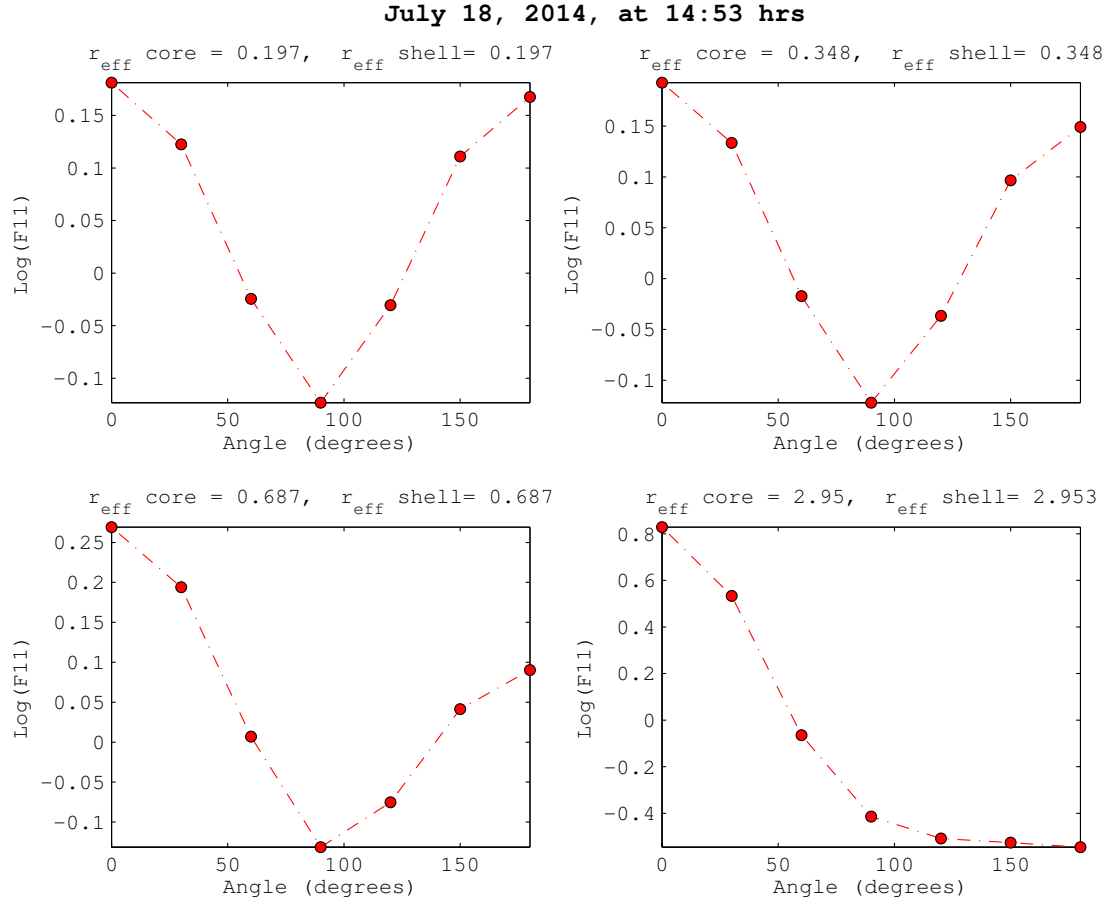


Figure 31:  $\text{Log}(F_{11})$  Müller matrix element for an ensemble of oblate spheroids as a function of scattering angle  $\theta$  and relative core size  $q$  for July 18, 2014 at 14:53 hrs.

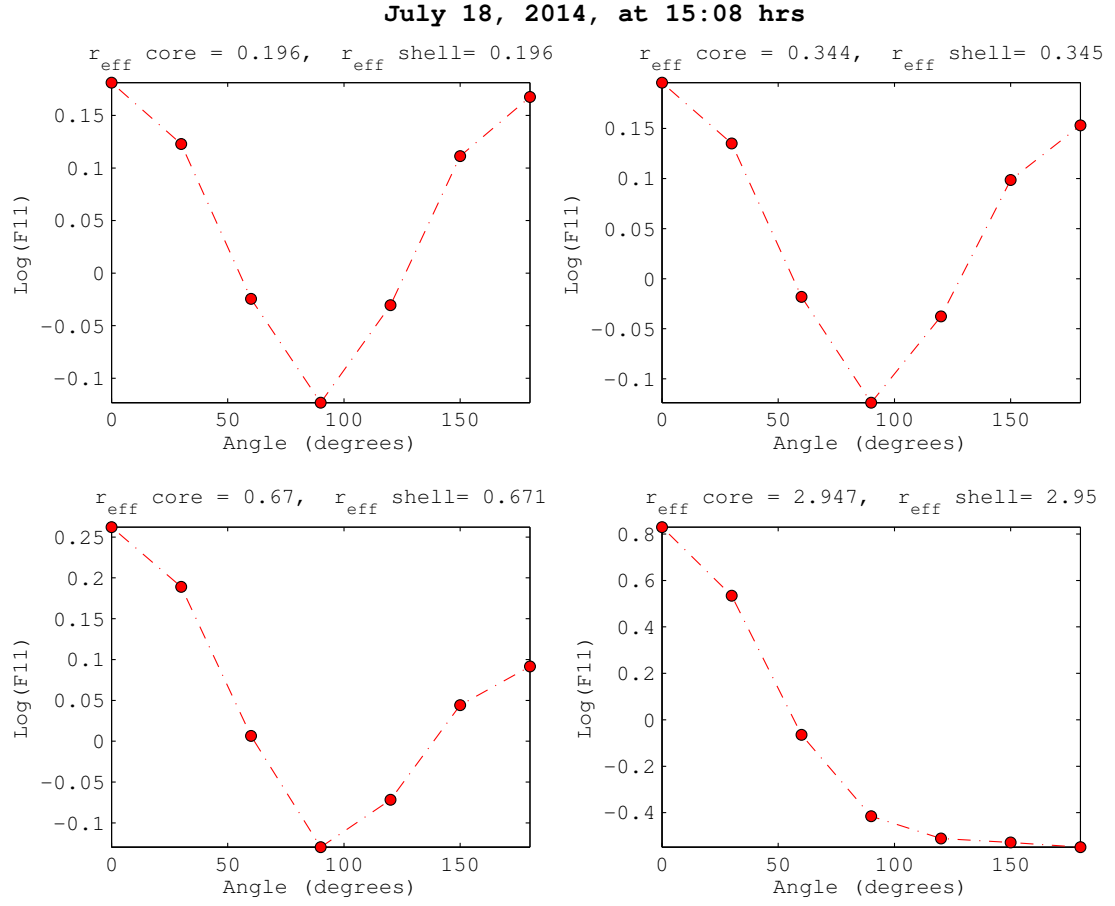


Figure 32:  $\text{Log}(F_{11})$  Müller matrix element for an ensemble of oblate spheroids as a function of scattering angle  $\theta$  and relative core size  $q$  for July 18, 2014 at 15:08 hrs.

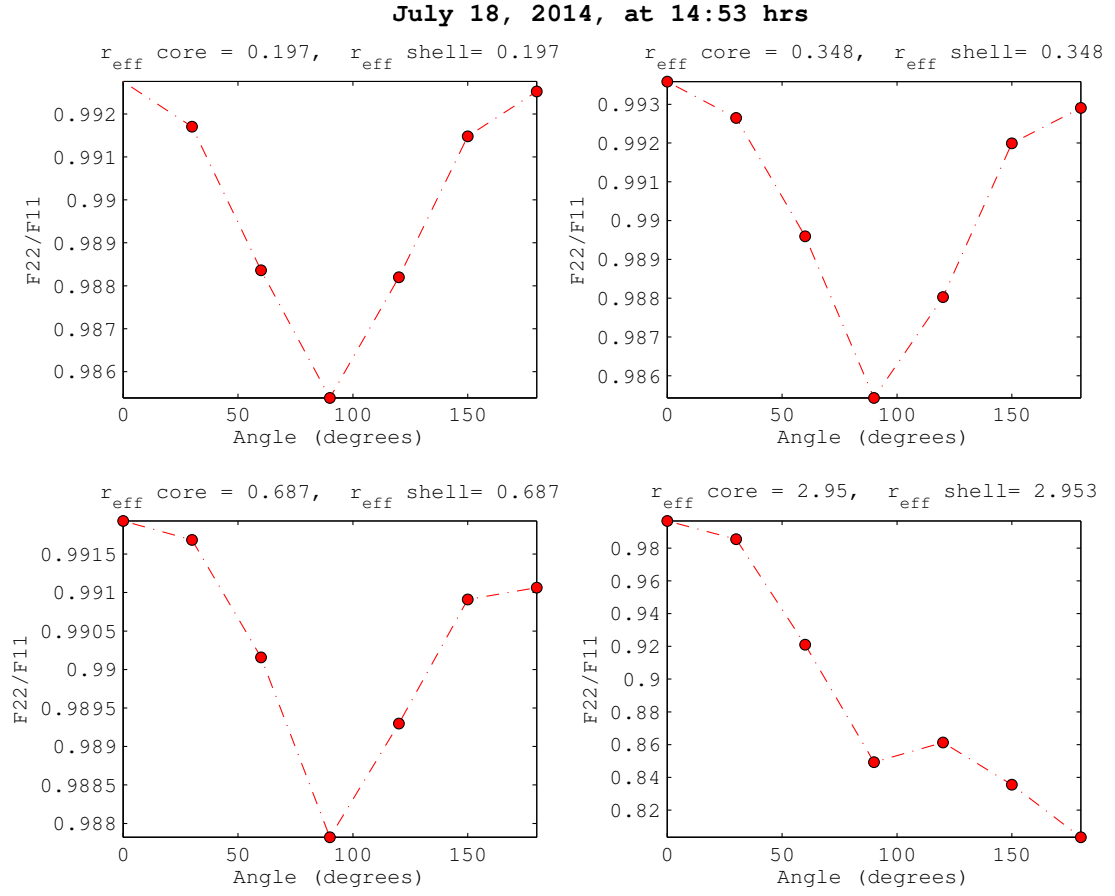


Figure 33:  $F_{22}/F_{11}$  Müller matrix element for an ensemble of oblate spheroids as a function of scattering angle  $\theta$  and relative core size  $q$  for July 18, 2014 at 14:53 hrs.

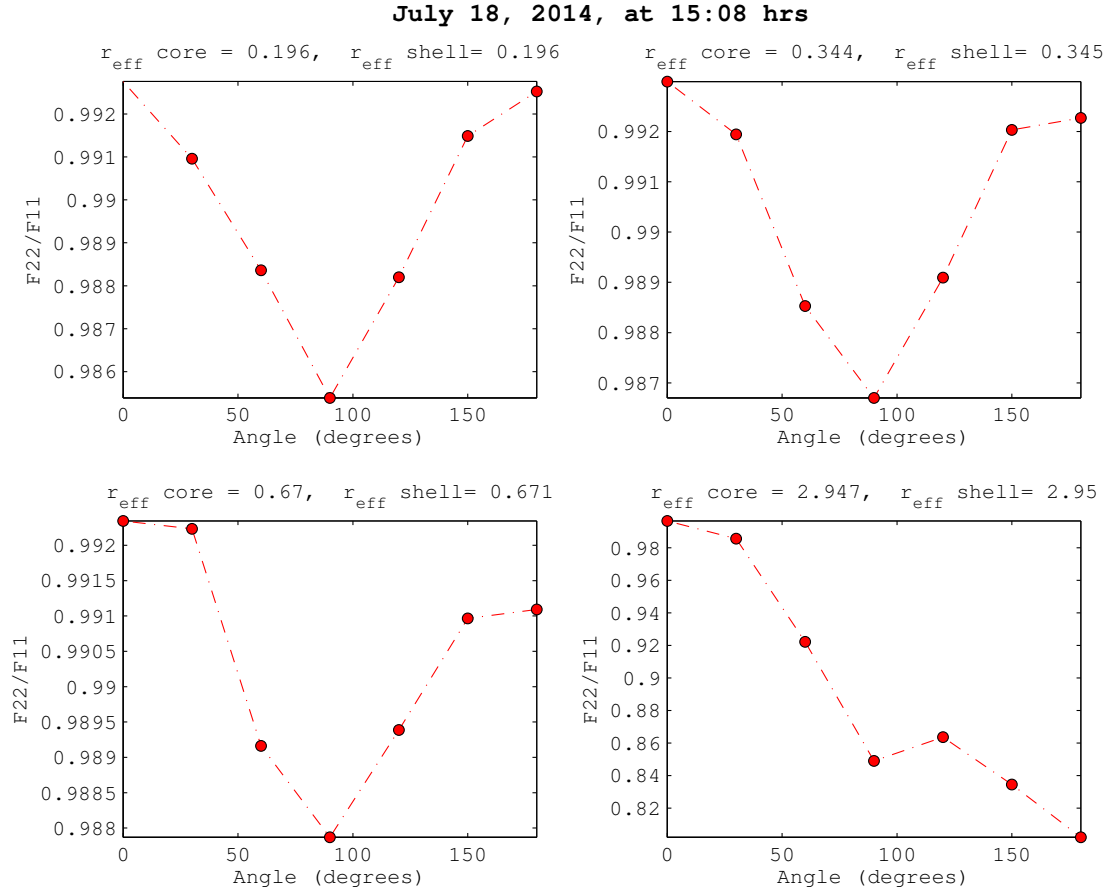


Figure 34:  $F_{22}/F_{11}$  Müller matrix element for an ensemble of oblate spheroids as a function of scattering angle  $\theta$  and relative core size  $q$  for July 18, 2014 at 15:08 hrs.

July 18, 2014, at 14:53 hrs

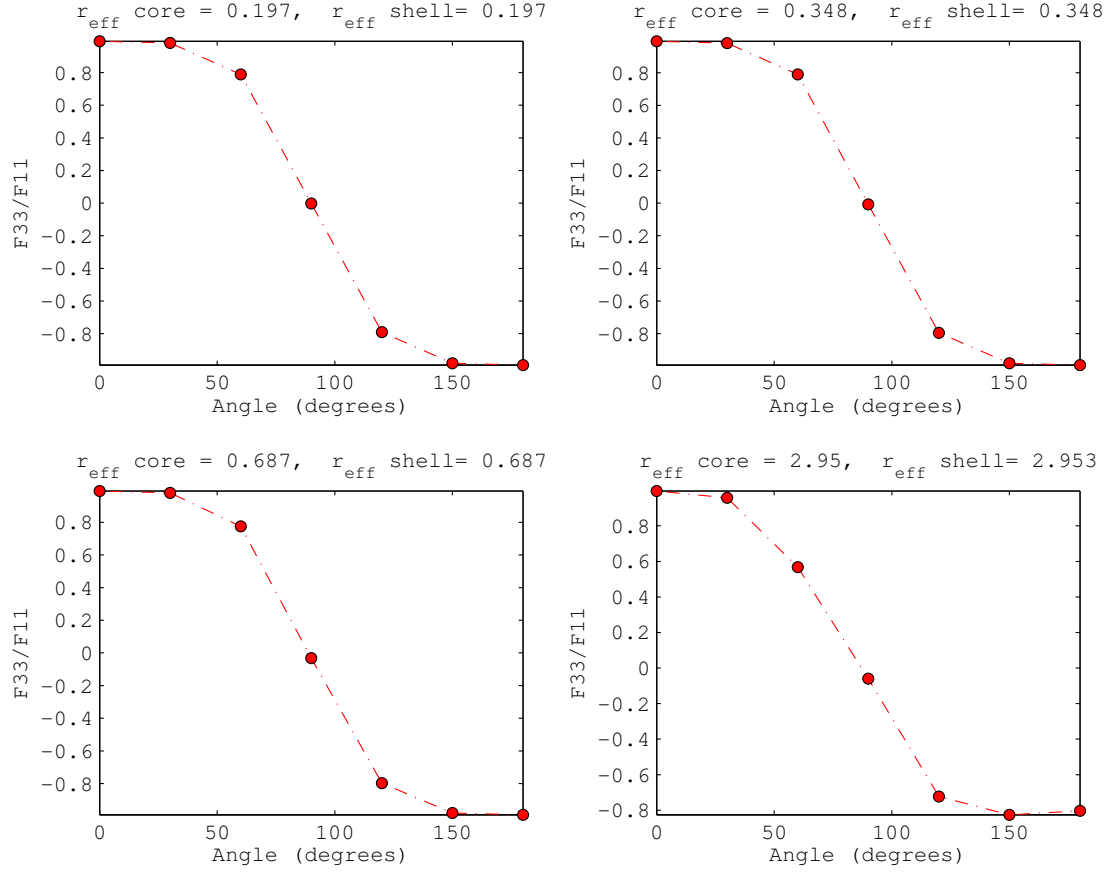


Figure 35:  $F_{33}/F_{11}$  Müller matrix element for an ensemble of oblate spheroids as a function of scattering angle  $\theta$  and relative core size  $q$  for July 18, 2014 at 14:53 hrs.

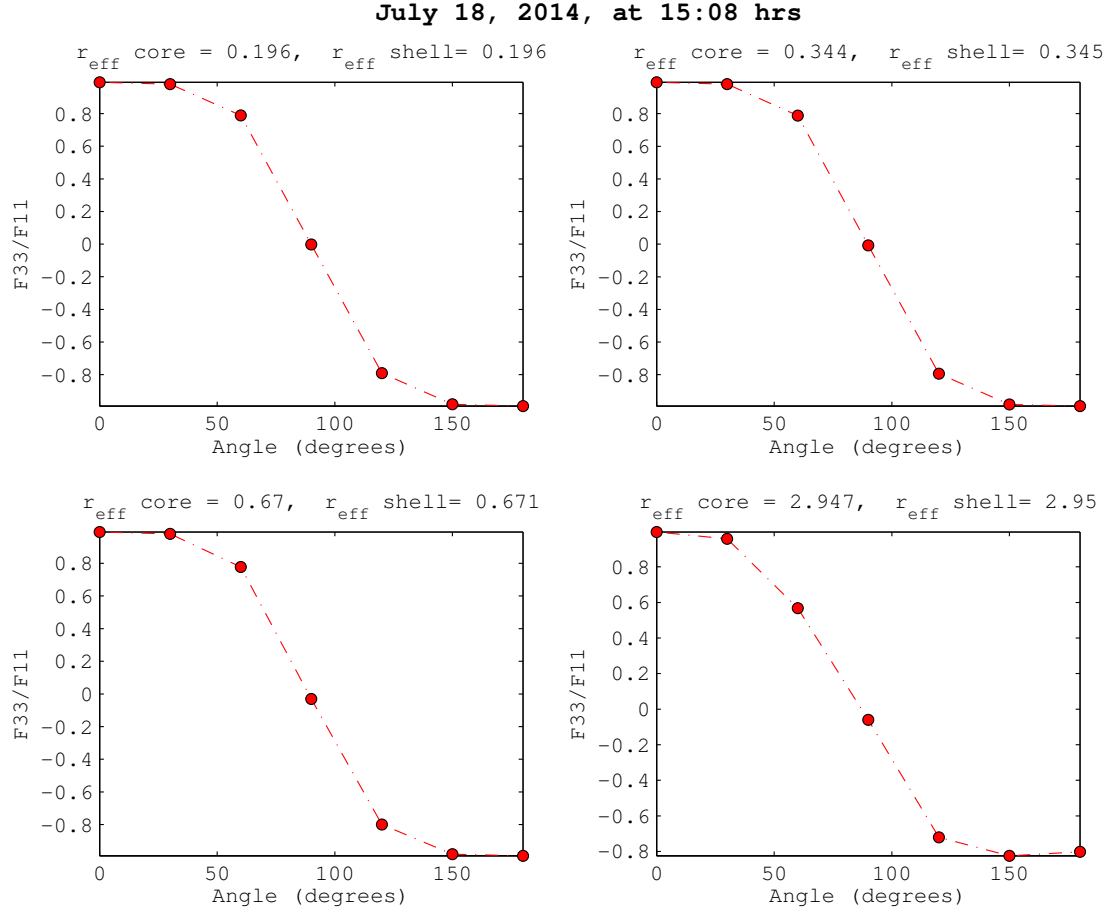


Figure 36:  $F_{33}/F_{11}$  Müller matrix element for an ensemble of oblate spheroids as a function of scattering angle  $\theta$  and relative core size  $q$  for July 18, 2014 at 15:08 hrs.

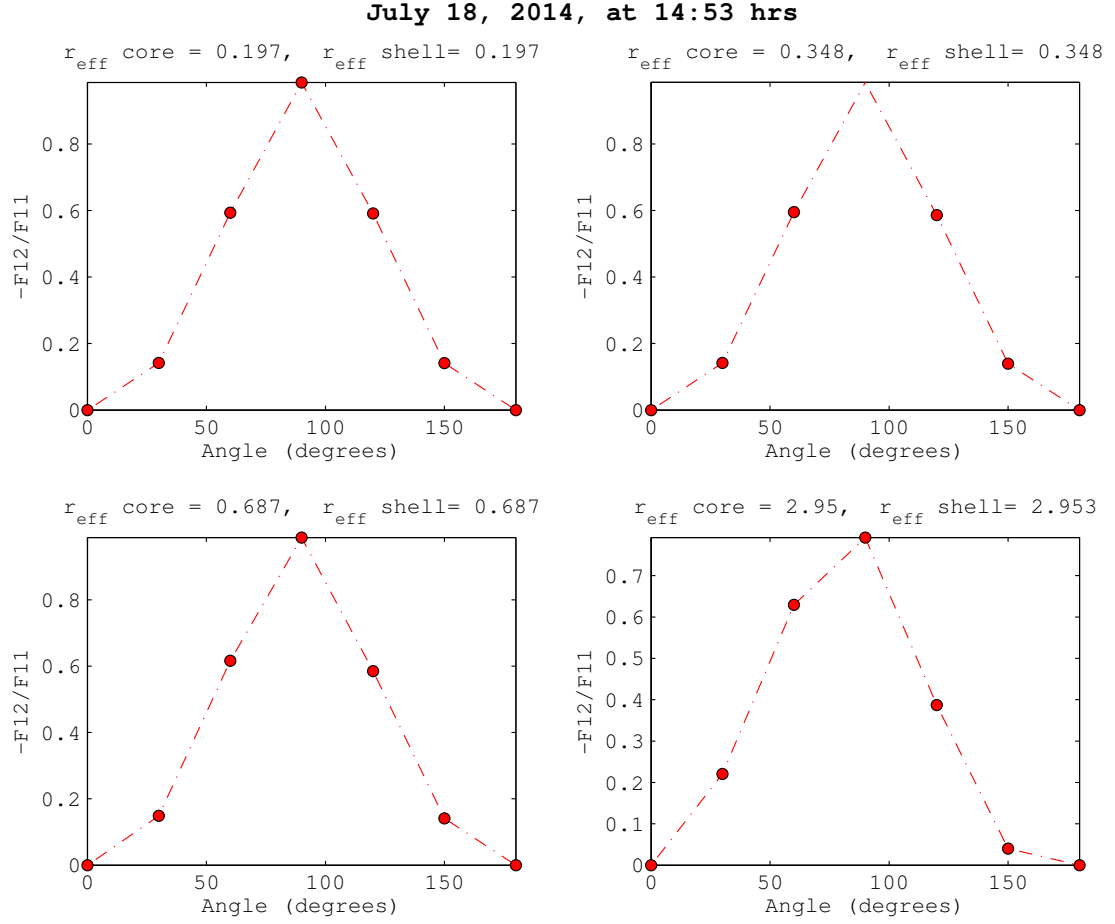


Figure 37:  $F_{12}/F_{11}$  Müller matrix element for an ensemble of oblate spheroids as a function of scattering angle  $\theta$  and relative core size  $q$  for July 18, 2014 at 14:53 hrs.

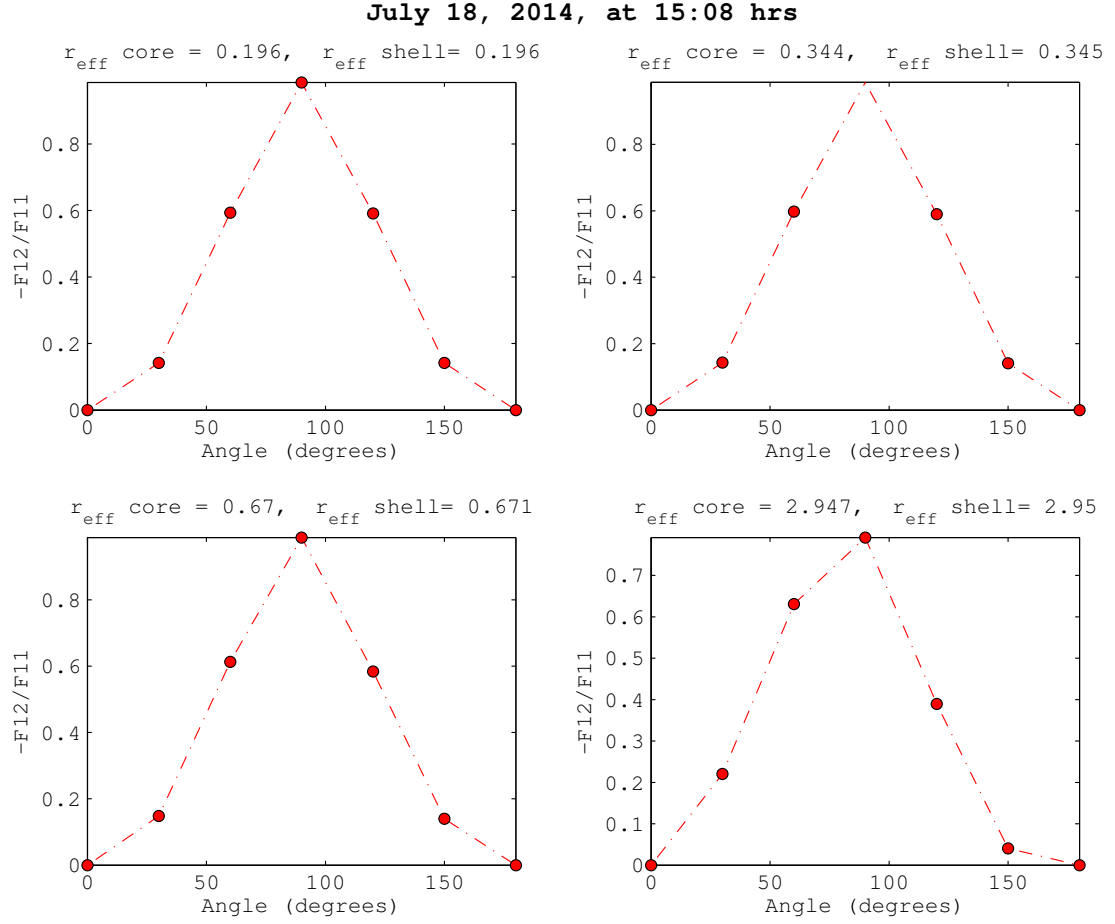


Figure 38:  $F_{12}/F_{11}$  Müller matrix element for an ensemble of oblate spheroids as a function of scattering angle  $\theta$  and relative core size  $q$  for July 18, 2014 at 15:08 hrs.

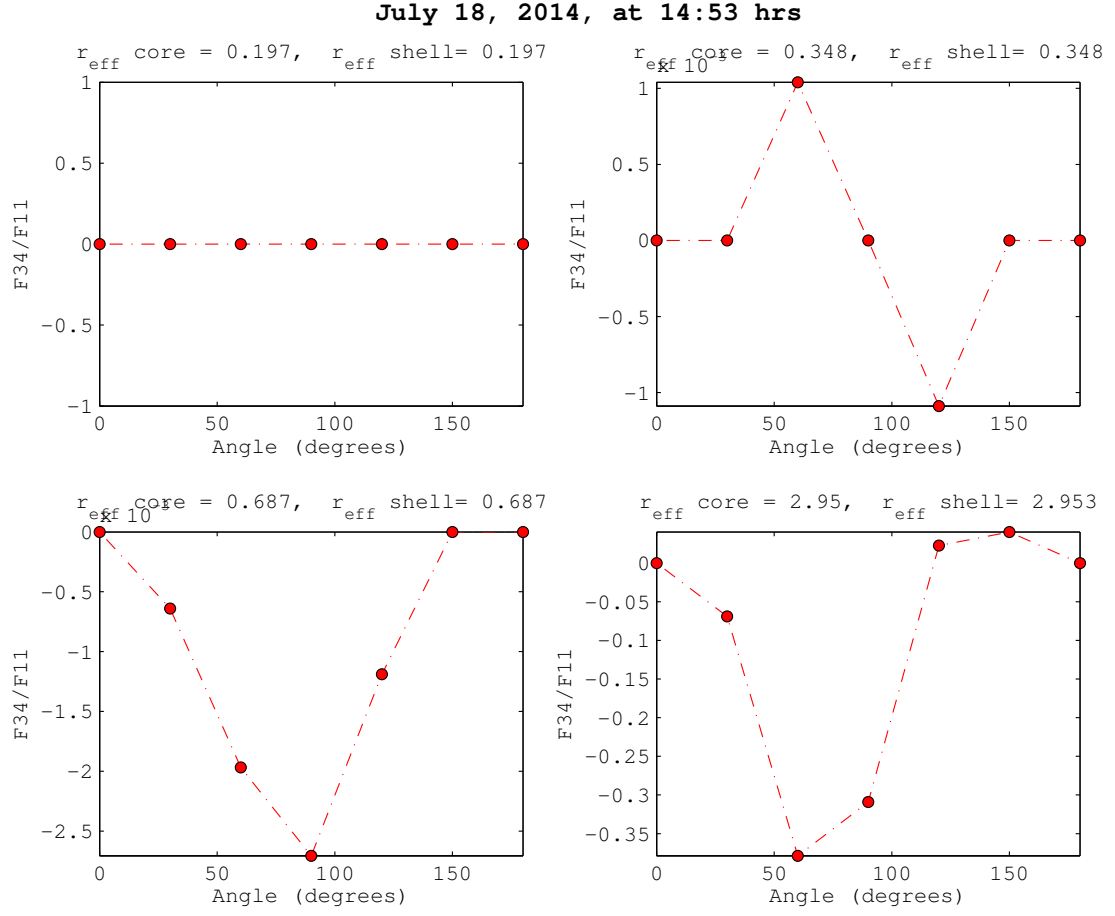


Figure 39:  $F_{34}/F_{11}$  Müller matrix element for an ensemble of oblate spheroids as a function of scattering angle  $\theta$  and relative core size  $q$  for July 18, 2014 at 14:53 hrs.

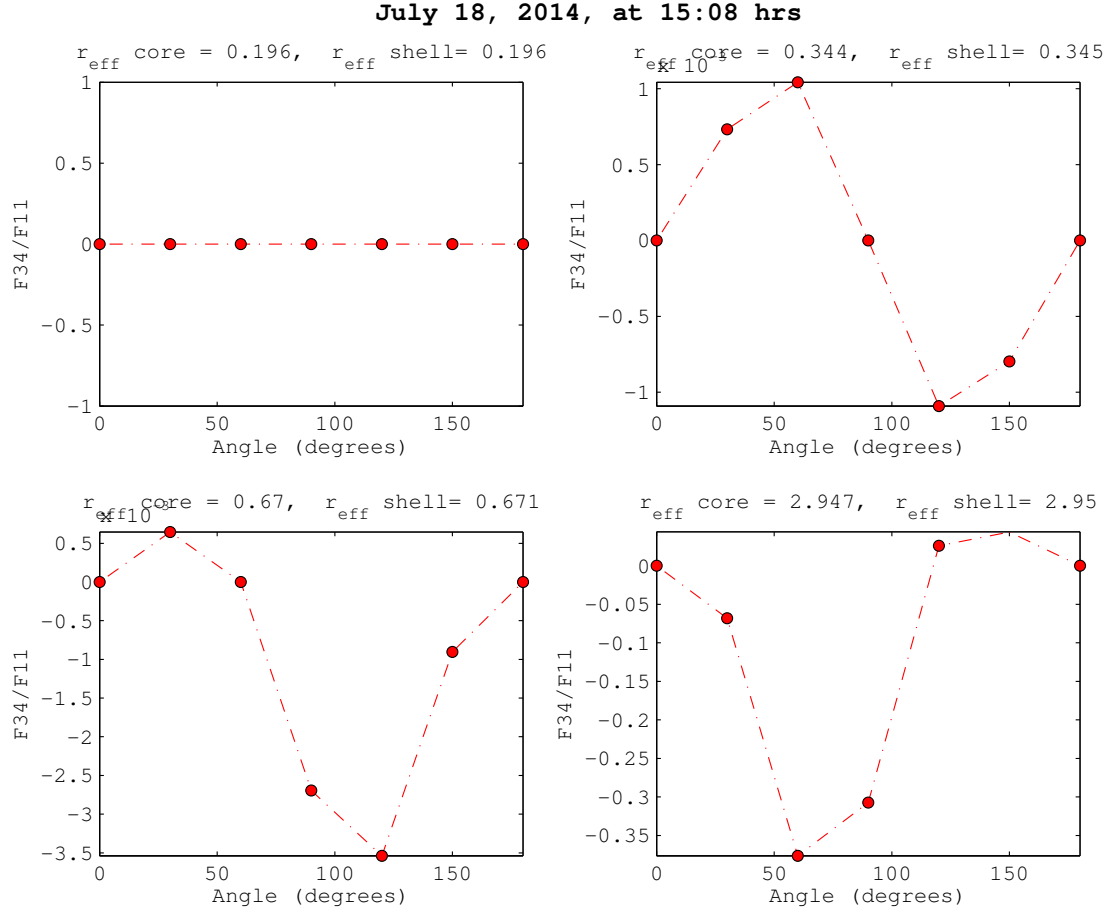


Figure 40:  $F_{34}/F_{11}$  Müller matrix element for an ensemble of oblate spheroids as a function of scattering angle  $\theta$  and relative core size  $q$  for July 18, 2014 at 15:08 hrs.

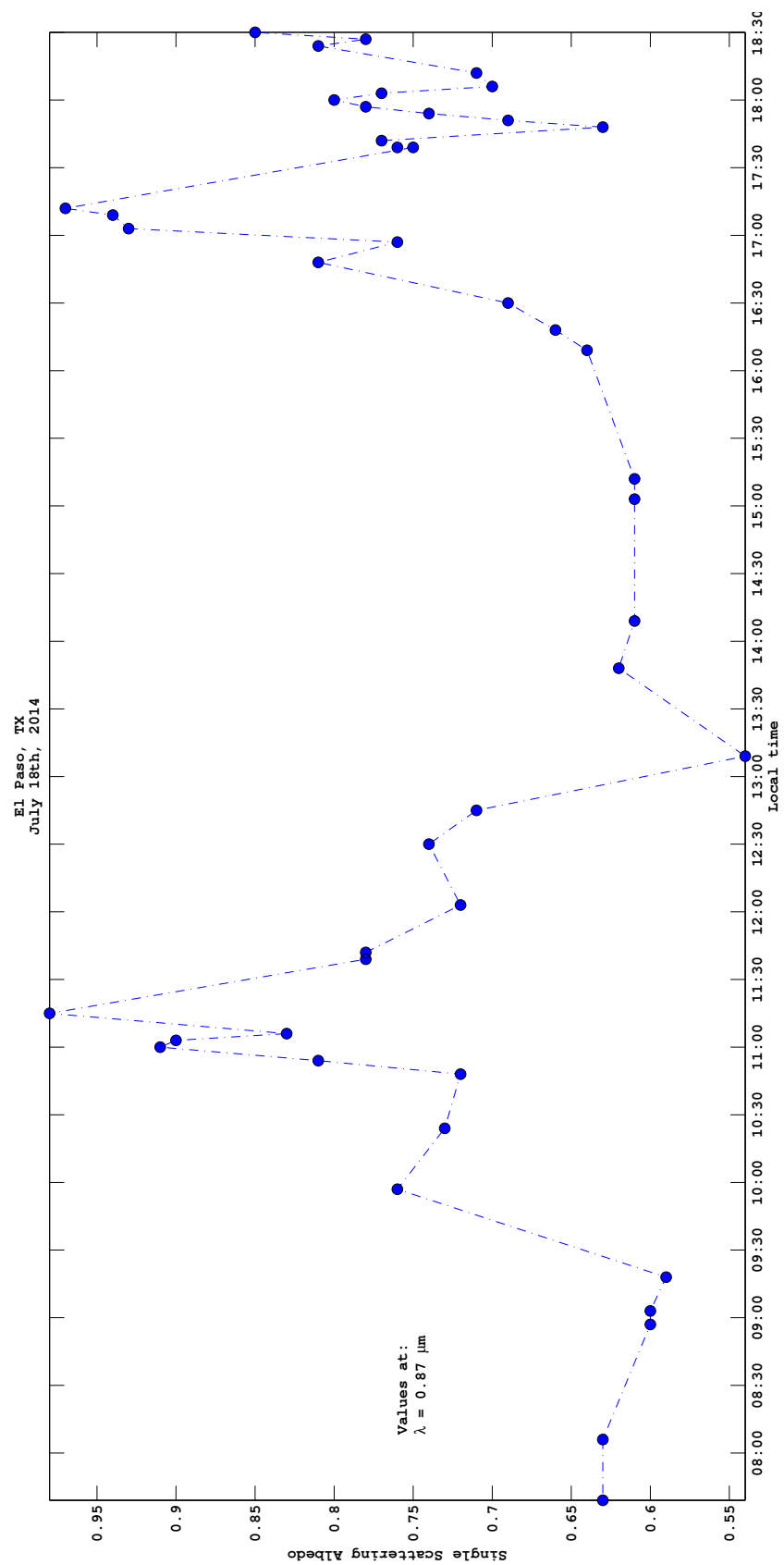


Figure 41: Single scattering albedo retrievals for July 18th, 2014.

## CHAPTER 4

### Conclusions and future work

#### 4.1 Conclusions

Scattering of solar radiation of  $0.87\ \mu\text{m}$  by atmospheric aerosols under the effects of humidity was calculated by using two models based in the T-matrix approximation showing reasonable agreement with the experimental data.

Although the scattering properties of core-shell models was not affected by the shell thickness because of its minimal hygroscopic growth, due to general low humidity; it shows better agreement during high humidity hours. Predictions by Bauer et al., [37] who stated that the shell thickness should be 20% of the core radius in order to be significant in light scattering.

The selected low relative humidity day show good agreement for both models which were built under the t-matrix approximation. The model for high humidity has a good response when the number distribution increases, as it has been seen on day april 13, 2013. However, humidity greater than 40% were not present in the region and the LISA model could not be proved in all the hourly events. In summary we can say that both models worked very well but it is necessary simulate more cases under extreme higher relative conditions and also changing the shape of the particles for better analysis. Despite of all, the scattering coefficients  $B_{\text{sca}}$  shown good agreement in most of the cases for both low and high relative humidities.

Only two species have been used in the simulations and they corresponded closely to the real composition of aerosols in the region. Mineral dust is the one that contributes more to the air masses and also to scattering. The measurements of number distribution by the particle laser counter and the mass concentration by the Texas Commission on Environmental Quality (TCEQ) allow to measure

the size distribution which is a good indicator of the air masses, however it will be useful to make measurements in finer meshes in diameters as well in short interval of times.

Particle shape was possible to observe under the Müller matrix elements. Although the wavelength was large to detect particles under  $1.0\mu\text{m}$  on effective radius, it was clear to observe polarization changes, sphericity and scattering properties per angle when it was necessary. Both selected days were similar in size and geometry, having similar matrices elements and similar values as well. This is another consequence of the absence of significant shell thickness on the particle.

The values of SSA showed that most of the particles in the airshed correspond to scattering particles, and the selection of the refractive indices for them at the wavelength chosen was correct. This also was confirmed by electron scanning spectroscopy (SEM) as it is seen in figures 42 and 43. There were few cases where the concentration of soot was relevant but it occurred in few cases, like at 6:34 AM and 8:34 AM for april 13th, 2013, and for 14:53 hrs and 15:08 hrs for July 18th, 2014. This few episodes of soot could correspond to high peak hours where emissions from motorized vehicles occurs at these time of the day. It is necessary to run emissions models to make a final conclusion about this.

In conclusion, this developed methodology was successfully used to find the composite refractive index for both day scenarios and estimate the percentages of the aerosol components, and it can be extended to other air masses where the composition is more complex.

## 4.2 Future Work

For the data processing of the particle counter, the size distribution function was assumed to be the log-normal distribution. The limitation on the number of channels or diameter bins of the particle counter, made it not possible to fit the

data, however this distribution is considered standard in aerosol counting techniques [10]. In future work, particle counters with better resolution in diameter channels and short collection time intervals is suggested.

Some computation improvements will demand some cost of memory, processing, and time. The T-matrix model has also a parallel version, which was developed to make bigger calculations. It is advisable to review the routines created and explore the capabilities of the model for larger data.

In the calculation, it was assumed that most of the particles were oblates and rounded in shape. In reality the shape of the particles can vary from spherical to non-spherical (also, chevyshev particles with more complicated shape). Figures 42 and 43 show the real shape of aerosols corresponding to El Paso airshed, simulation of this particle is difficult to create, however there exist some programs that can simulate them and are of free use (see for example Wriedt [38]).

The single scattering albedo allowed to observe the composition of the particles in the air masses. This methodology can be combined with some other instruments in order to detect other parameters involved in the study of atmospheric aerosols. For example, it would be interesting to retrieve values of the phase factor described in eq. 8. This parameter in combination with the Müller matrices will help us to create a complete description of the size and shape of the particles and their effects on scattering.

Finally, we are trying to complement this work with some image processing of the pictures taken by ordinary digital cameras. In the future we expect to have this information as a data source for brightness and contrast information of the meteorological range or visibility in visible wavelength range during the day and also for night using infrared cameras to match with the wavelength used in this work.

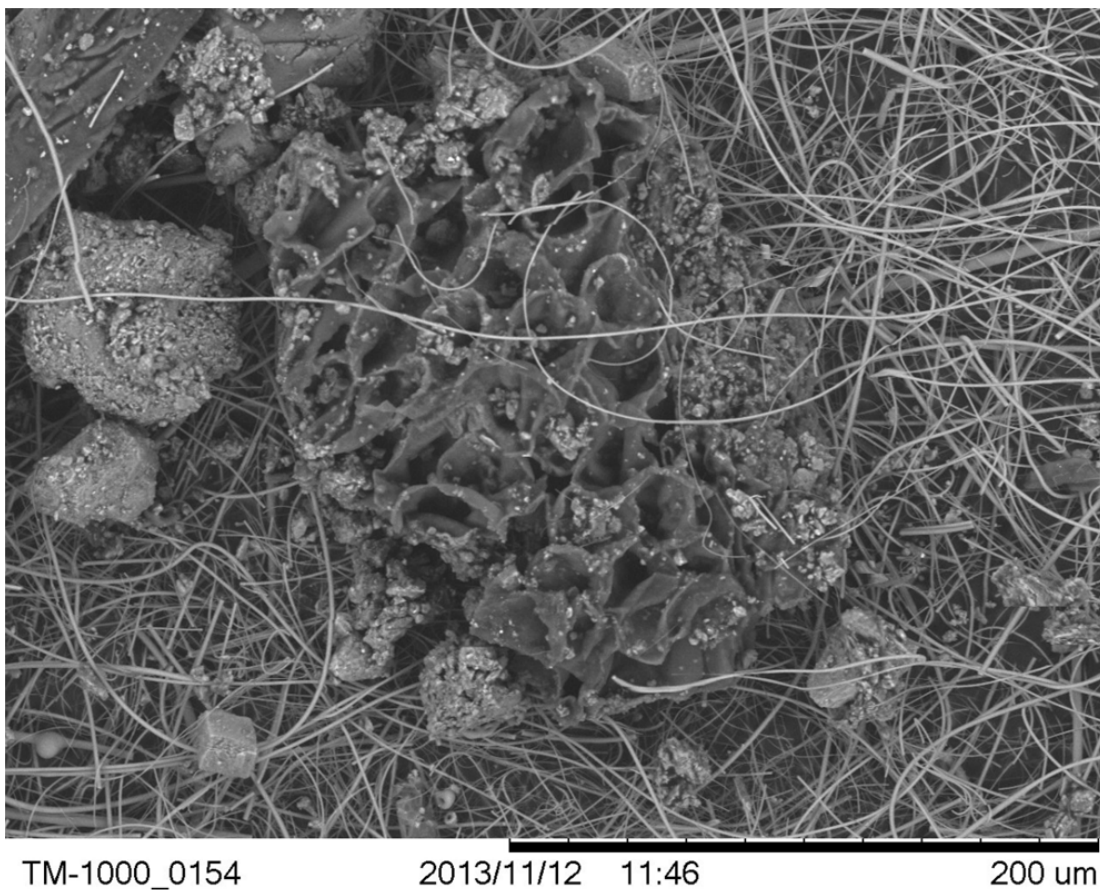


Figure 42: Aerosol particle at 200 $\mu$ m scale resolution. The threads in the figure are the composition of special filters used in the filtering process.

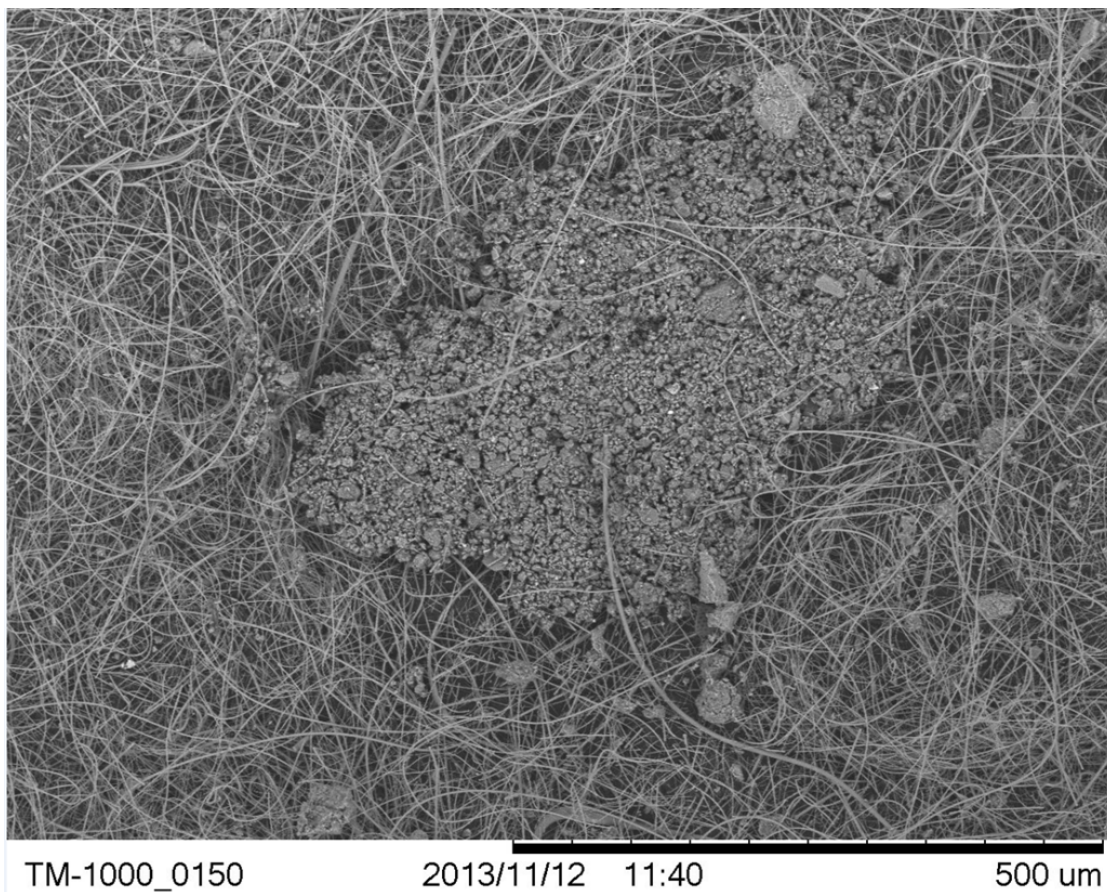


Figure 43: Aerosol particle at 500 $\mu$ m scale resolution. The threads in the figure are the composition of special filters used in the filtering process.

## List of References

- [1] A. Winkel and G. Jander, *Schwebstoffe in Gasen (Aerosole)*. Ferdinand Enke, 1939.
- [2] H. J. Seinfeld and N. P. Spyros, *Atmospheric Chemistry and Physics, from Air Pollution to Climate Change*. John Wiley & Sons Inc., 2006.
- [3] R. Medina, R. Fitzgerald, and Q. Min, “Retrieval of the single scattering albedo in the el paso-juarez airshed using the tuv model and a uv-mfrsr radiometer,” *Atm. Env.*, vol. 46, pp. 430–440, 2012.
- [4] A. P. Waggoner, R. E. Weiss, N. C. Ahlquist, D. S. Covert, S. Will, and R. J. Charlson, “Optical characteristics of atmospheric aerosols,” *Atm. Env.*, vol. 15, pp. 1891–1909, 1981.
- [5] I. M. Mishchenko, *Scattering, Absorption, and Emission of Light by Small Particles*. Cambridge University Press, 2002.
- [6] A. Kokhanovsky, *Light Absorption and Scattering by Particles in the Atmosphere*. Springer, 2008.
- [7] L. Elterman, “Uv, visible, and ir attenuation for altitudes to 50 km,” *Air Force Cambridge Res. Lab.*, vol. 68, 1968.
- [8] M. Z. Jacobson, *Fundamentals of Atmospheric Modeling*. Cambridge University Press, 2005.
- [9] W. C. Hinds, *Aerosol Technology: Properties, Behavior; and Measurement of Airborne Particles*. John Wiley & Sons, 1998.
- [10] J. L. Hand, S. M. Kreidenweis, J. Slusser, and G. Scott, “Comparisons of aerosol optical properties derived from sun photometry to estimates inferred from surface measurements in big bend national park, texas,” *Atm. Env.*, vol. 38, pp. 6813–6821, 2004.
- [11] C. F. Bohren and D. R. Huffman, *Absorption and Scattering of Light by Small Particles*. Wiley-VCH, 1998.
- [12] J. D. Jackson, *Classical Electrodynamics*. Wiley, 1975.
- [13] H. C. van de Hulst, *Light scattering by small particles*. Wiley, 1957.
- [14] G. N. Watson, *A treatise on the Theory of Bessel functions*. Cambridge University Press, 1958.
- [15] E. Collett, *Polarized Light: Fundamentals and Applications*. CRC Press, 1992.

- [16] S. Chandrasekhar, *Radiative Transfer*. Dover Publications, 1960.
- [17] P. C. Waterman, "Matrix formulation of electromagnetic scattering," *Proc. IEEE*, vol. 41, pp. 1633–1639, 1965.
- [18] P. C. Waterman, "Symmetry, unitarity, and geometry in electromagnetic scattering," *Phys. Rev.*, vol. D3, pp. 825–839, 1971.
- [19] P. C. Waterman, *Numerical solution of electromagnetic scattering problems. In Computer Techniques for Electromagnetics*. R. Mitra, 1973.
- [20] P. C. Waterman, "Matrix methods in potential theory and electromagnetic scattering," *J. Appl. Phys.*, vol. 50, pp. 4550–4566, 1979.
- [21] A. Aden and K. M., "Scattering of electromagnetic waves from two concentric spheres," *J. Appl. Phys.*, vol. 22, pp. 1242–1246, 1951.
- [22] A. Quirantes, "A t-matrix method and computer code for randomly oriented, axially symmetric coated scatterers," *J. Quant. Spectrosc. Radiat. Transfer*, vol. 92, pp. 373–381, 2005.
- [23] A. Quirantes, "Light scattering properties of spheroidal coated particles in random orientation," *J. Quant. Spectrosc. Radiat. Transfer*, vol. 63, pp. 263–275, 1999.
- [24] B. P. W., *Light scattering by particles: computational methods*. World Scientific, 1990.
- [25] B. Peterson and S. S., "T-matrix formulation of electromagnetic scattering from multilayered scatterers," *Phys. Rev. D*, vol. 10, p. 2670, 1974.
- [26] P. M. Systems, 2011, basic Guide to Particle Counters and Particle Counting.
- [27] D. Aldaco and J. C. Roque, *CI-550, laser particle counter, operator's manual*. CLIMET INSTRUMENTS, 2002.
- [28] D. M. Technologies, 2013, pAX, Photoacoustic Extinctionmeter.
- [29] M. I. Mishchenko and L. D. Travis, "Capabilities and limitations of a current fortran implementation of the tmatrix method for randomly oriented, rotationally symmetric scatterers," *J. Quant. Spectrosc. Radiat. Transfer*, vol. 60, pp. 309–324, 1998.
- [30] T. Nousiainen and K. Vermeulen, "Comparison of measured single-scattering matrix of feldspar particles with t-matrix simulations using spheroids," *J. Quant. Spectrosc. Radiat. Transfer*, vol. 79-80, pp. 1031–1042, 2003.

- [31] T. L. D. Mishchenko, M. I. and A. Macke, “Scattering of light by polydisperse, randomly oriented, finite circular cylinders,” *Appl. Opt.*, vol. 35, pp. 4927–4940, 1996.
- [32] G. Hänel, “The properties of atmospheric aerosol particles as functions of the relative humidity at thermodynamic equilibrium with the surrounding moist air,” *Advances in Geophysics*, vol. 19, pp. 73–188, 1976.
- [33] G. Hänel, “Computation of the extinction of visible radiation by atmospheric aerosol particles as a function of the relative humidity, based upon measured properties,” *Aerosol Sci.*, vol. 3, pp. 377–386, 1972.
- [34] R. Pearson and R. Fitzgerald, “Application of a wind model for the el paso-juarez airshed,” *J. of the Air and Wasted Management Association*, vol. 51, pp. 669–680, 2001.
- [35] N. Rivera Rivera, T. Gill, K. Gebhart, J. Hand, M. Bleiweiss, and R. M. Fitzgerald, “Application of a wind model for the el paso-juarez airshed,” *Atm. Env.*, vol. 43, pp. 347–354, 2009.
- [36] J. L. Hand and S. M. Kreidenweis, “A new method for retrieving particle refractive index and effective density from aerosol size distributions data,” *Aerosol Science and Technology*, vol. 10, pp. 1012–1026, 2002.
- [37] S. E. Bauer, M. I. Mishchenko, A. A. Lacis, S. Zhang, P. J., and S. M. Metzger, “Do sulfate and nitrate coatings on mineral dust have important effects on radiative properties and climate modeling?” *J. Geophys. Research*, vol. 112, 2007.
- [38] T. Wriedt, “Using the t-matrix for light scattering computations by non-axisymmetric particles: Superellipsoids and realistically shaped particles,” *Part. Syst. Charact.*, vol. 4, pp. 256–268, 2002.

## Vita

Richard Medina Calderon earned the bachelor degree in Physics from The Universidad Nacional Mayor de San Marcos in Lima, Peru, in 2000. He worked at the Nuclear Reactor Laboratory in Huarangal, Lima for two years. During that time he developed a graphic interface for the Peruvian Nuclear Reactor RP10 as part of his thesis work to obtain the Licence to teach Physics in 2002.

He worked as Physics lecturer at the Universidad Tecnologica del Peru in Lima during the years of 2003 to 2006. After that, he joined the Master of Physics Program at the University of Texas at El Paso in the spring of 2007 where he obtained his Masters in Physics during the Summer of 2009 with his thesis entitled "Characterization of Aerosols in the El Paso-Juarez Airshed". After finished his Master, he was admitted to the Doctoral Program of Computational Sciences in the Fall of 2009 and here obtained his second Master degree in 2013. While pursuing the PhD degree, Dr. Medina worked as research assistant and assistant instructor for the department of Physics. As a researcher he has participated in many events related to Atmospheric Sciences and Light scattering. It is important to mention that Dr Medina has performed innovative research in the field of light scattering by atmospheric aerosols in the area, making important contributions to the scientific community and he has presented his research at international conference meetings and workshops including his publication about Retrieval of scattering albedo in El Paso del Norte Airshed, in Atmospheric Environment journal in 2012, which was supervised by Dr. Rosa Fitzgerald.

Permanent Address: 3512 Hixson St  
El Paso, TX 79902

This dissertation was typed by Richard Medina Calderon.